BATCH FABRICATION OF CANTILEVERED MAGNETIC NANORODS ON ATTONEWTON-SENSITIVITY SILICON OSCILLATORS FOR MAGNETIC RESONANCE FORCE MICROSCOPY

A Dissertation

Presented to the Faculty of the Graduate School

of Cornell University

in Partial Fulfillment of the Requirements for the Degree of

Doctor of Philosophy

by

Steven Alexander-Boyd Hickman

February 2010

© 2010 Steven Alexander-Boyd Hickman

ALL RIGHTS RESERVED

BATCH FABRICATION OF CANTILEVERED MAGNETIC NANORODS ON ATTONEWTON-SENSITIVITY SILICON OSCILLATORS FOR MAGNETIC RESONANCE FORCE MICROSCOPY

Steven Alexander-Boyd Hickman, Ph.D.
Cornell University 2010

Magnetic resonance spectroscopy and imaging are powerful tools for characterizing soft materials at length scales down to a few microns. While mechanical detection has enabled observation of magnetic resonance from single electron spins and nanoscale volumes of nuclear spins, all such experiments to date have required manually affixing a magnetic particle or a sample to the leading edge of a fragile microcantilever. In this dissertation, work to batch-fabricate attonewton sensitivity cantilevers with integrated, overhanging nickel magnets is described. That the magnet overhangs the leading edge of the cantilever is necessary to mitigate surface-induced force noise, the dominant source of noise in all high-sensitivity magnetic resonance force microscopy measurements to date. The smallest magnets produced had diameters of 70 nm.

Three methods were developed to produce such overhanging magnets on single-crystal silicon cantilevers. Proof-of-concept work was demonstrated on methods involving under-etching the magnetic nanorods using potassium hydroxide, and fabricating the nanorods over co-planar silicon oxide pillars. Complete devices were produced via a method in which the magnetic nanorods were under-etched by an isotropic sulfur hexafluoride reactive ion plasma etch.

In addition to developing processes to produce overhanging nanorods, significant challenges in lithographic alignment and silicide formation were over-

come. Cantilever magnetometry demonstrated a net tip magnetization between 57 and 77 % of that expected for bulk nickel. Good leading-edge magnetization of the nanorods was confirmed by using the cantilevers to detect, via force-gradients, electron spin resonance from nitroxide spin labels in a thin film. This is the first time that magnetic resonance force microscopy has been implemented with magnet-tipped cantilevers produced by batch fabrication. Over the same thin film used for the electron spin resonance experiment, the cantilevers were shown to have extremely low surface-induced force noise. The work covered in this dissertation significantly advances the feasibility of scanned-probe nanoscale magnetic resonance imaging of as-fabricated thin-film samples and devices.

BIOGRAPHICAL SKETCH

Steven Alexander-Boyd Hickman was born in Iowa City, Iowa on October 11, 1981 to Mary and J.C. Hickman. At age five, the family (with older sister Sarah) moved to Bellingham, WA. Steven quickly took to the sports of the area, becoming an active skier in the winter, and competitive sailor in the summer. In the eighth grade he first took an interest in chemistry, as preparation for a planned career in pyrotechnics. While at Sehome High School, he continued this interest, starting what would become a long and fruitful research partnership with Dr. David Patrick of Western Washington University. It was this research that earned him selection as a finalist in the Intel Science Talent Search, and was likely a major contribution to his selection as a 2000 United States Presidential Scholar.

Leaving often drizzly Bellingham for the warm coastal scrub of Claremont, CA, Steven matriculated at Harvey Mudd College. In addition to being an average chemistry student, he was president of Case Dormitory for two years and spent a very beneficial semester abroad at the University of Queensland in Australia. After graduation with a B.S. in chemistry in May of 2004, he headed to Cornell University for graduate study, lured by the strong reputation of Cornell's nanofabrication facility. Despite the demands of graduate work in the group of Professor John Marohn, Hickman found time to earn a pilots license, become well versed in winemaking practices and technology, and meet his future wife Anya. He also managed to attend more than 15 conferences, winning awards at three.

With his dissertation completed, Steven is heading to Cornell's bitter hockey rival Harvard University, to take a position at the Center for Nanoscale Systems.

The real trouble with this world of ours is not that it is an
unreasonable world, or even that it is a reasonable one.
The commonest kind of trouble is that it is nearly reasonable,
but not quite ... It looks just a little more mathematical
and regular than it is: its exactitude is obvious, but its
inexactness is hidden; its wildness lies in wait.

-G. K. Chesterton

ACKNOWLEDGEMENTS

Thanks to my advisor, John Marohn. You have constantly been pushing my knowledge forwards during my time at Cornell, and have been an excellent scientific mentor. As well, your seemingly endless trove of facts on an incredible breadth of subjects continues to amaze. Acknowledgement and gratitude must as well go to my extremely understanding committee, Harold Craighead and Poul Petersen, and, for the A-exam, Jack Freed.

The initial work on this project was done by Sean Garner, Neil Jenkins, and Seppe Kuehn. They developed an excellent foundation, and were very welcoming to a fresh young first-year. Thank you for taking me on-board. Much of the work in the measurements section of the document was done by other members of the Marohn group, for which I am extremely grateful. Eric Moore and Sanggap Lee took the ESR-MRFM, magnetometry, and other measurements of cantilever properties, and also provided valuable discussion about MRFM principles. John Marohn, Lee Harrell, and Jay Van Delden, as well as cornell undergrads Jeremy Ong and Eric VanWerven all contributed to the fabrication work. Lee, along with Sarah Wright, developed the ESR simulations. And Jonilyn Longenecker has taken up the torch behind me. On a personal level, thank you to all members of the Marohn group, past and present, for all your help and support. A special thanks must go to Showey Yazdanian, for being there for the long haul, and support in conquering an Expedition sundae.

My parents have been a constant support throughout, with love, advice, well-timed shipments of cookies, and driving my stuff and car out across the country twice. I could have never made it this far without your help. Thank you. Thanks to my sister Sarah for showing me how to do college right, trying to make me less of a nerd,and being a great road trip partner.

Anya, you are without a doubt the best part of the last 5+ years. If meeting you was the only thing I gained from Cornell, it would have been well worth it. I love you. And thanks to Tulip for bringing us together.

To the friday night dinner group, thanks for all the great times and good meals. And to Quenten and Marlene, always up for a beer or a BBQ. Thanks as well to the rest of the CNF core users, Steve, Shahyaan, Dana, Gregory, and others I am likely forgetting at the moment. Your help, insight, and well-timed humor has immeasurably helped my work. As well, without the help of the CNF staff, especially Rob Ilic, I would not have been able to accomplish this project.

Outside of Cornell, the staff and members of the East Hill Flying Club provided great times and excellent instruction my first few years at CU. And Peter Bell, Tricia and the rest of the staff at Fox Run Vineyards have provided a great escape for my last years at school.

TABLE OF CONTENTS

Biographical Sketch . . . iii
Dedication . . . iv
Acknowledgements . . . v
Table of Contents . . . vii
List of Tables . . . x
List of Figures . . . xi

1 Introduction 1
1.1 Signal Calculation . . . 4
1.2 Spin Manipulation . . . 6
1.3 Thermally-limited Detection Limit . . . 9
1.4 Pendulum Geometry . . . 10
1.5 Sample Versus Magnet on Cantilever . . . 12
1.6 Signal Detection in Pendulum Geometry . . . 12
1.7 Surface Noise . . . 14
1.8 Other Cantilever Applications . . . 16

2 Background 19
2.1 Cantilever Dynamics . . . 19
2.2 Prior Cantilever Fabrication Work . . . 22
2.3 Other Methods for Producing Overhanging Magnets . . . 22
2.4 Intrinsic Dissipation and Quality Factor . . . 24
2.5 Magnetic Materials . . . 27

3 Fabrication 30
3.1 Process Outline . . . 30
3.2 Methods to Produce Overhanging Magnets . . . 36
3.2.1 Magnet Undercut Via Anisotropic Silicon Etching . . . 37
3.2.2 Magnet Undercut Via Isotropic Plasma Etching . . . 39
3.2.3 Silicon Oxide Pillars . . . 42
3.3 Alignment Challenges . . . 46
3.3.1 Marks for the Silicon Oxide Pillar Process . . . 49
3.4 Backside Silicon Oxide . . . 51
3.5 Release Process Issues . . . 52
3.5.1 Silicon Oxide Membrane Cracking . . . 52
3.5.2 Through-wafer Etch Non-uniformity and Resulting Silicon Overetch . . . 54
3.5.3 Magnet Damage From Hydrofluoric Acid Etch . . . 56
3.5.4 Precipitation of HF etch products . . . 57

4 Silicides **59**
4.1 Evidence for Silicides 61
4.2 Barrier Layer for Silicide Prevention 65
4.3 Alternative to the Bosch Etch 70
4.4 Heat Management in the Bosch Etch 71
4.4.1 Heat Sink Wafer 71
4.4.2 Aperture Plates 72
4.4.3 Slow Etching 72
4.4.4 Cryogenic Etch 73

5 Cantilever and Magnet Analysis **75**
5.1 Probe 75
5.2 Frequency, Spring Constant and Quality Factor Measurement . . 75
5.3 Cantilever Magnetometry 76
5.4 Force Gradient Detection of Electron Spin Resonance 78
5.5 Surface-induced Dissipation and Frequency Noise 80
5.6 Results of Cantilever Analysis 81
5.7 Other Applicable Analysis Techniques 90

6 Conclusion and Future Directions **94**
6.1 Better Cantilever Force Sensitivity 94
6.2 Smaller Magnets 95
6.3 Other Magnetic Materials 98
6.4 Magnet Capping Layers 100

A Fabrication Process for Overhanging Magnet-tipped Cantilevers Using SF_6 Etching **104**
A.1 Alignment Mark Preparation 104
A.2 Magnet Preparation 106
A.3 Etch Pit Preparation 108
A.4 Etch Pit Etching 108
A.5 Cantilever Body Preparation 109
A.6 Cantilever Body Etching 110
A.7 Protective Top Silicon Oxide Deposition 111
A.8 Backside Silicon Oxide Deposition 111
A.9 Backside Resist Preparation 111
A.10 Backside Silicon Oxide Etch 112
A.11 Through-wafer Silicon Etch 113
A.12 Release 114
A.13 Critical point drying 114

B Process Modification to Eliminate Protective Front Silicon Oxide **116**
B.1 Backside Silicon Oxide Deposition 116
B.2 Protective PMMA Front Coating 116

B.3 Through-wafer Silicon Etch with SEM Monitoring 117
B.4 Release 117

C Fabrication Process for Overhanging Magnet-tipped Cantilevers Using Silicon Oxide Pillars 118
C.1 Alignment Mark Preparation 118
C.2 Alignment Mark Etching - Aluminum 118
C.3 Alignment Mark Etching - Silicon and Silicon Oxide 119
C.4 Silicon Nitride Layer Deposition 120
C.5 Silicon Nitride Mask Preparation 120
C.6 Silicon Oxide Pillar Growth 121
C.7 Silicon Oxide Pillar Chemical Mechanical Polishing 122
C.8 Silicon Nitride Layer Removal 122
C.9 Magnet Preparation 122
C.10 Cantilever Body Etch 122

D Fabrication Process for Overhanging Magnet-tipped Cantilevers Using Potassium Hydroxide Underetching 124
D.1 Thin Silicon Oxide Layer Deposition 124
D.2 Etch Pit Preparation 124
D.3 Etch Pit Silicon Oxide Etching 125
D.4 Etch Pit Silicon Etching 126
D.5 Potassium Hydroxide Silicon Underetch 126

E CAD and Mask Sets 128

Bibliography 131

LIST OF TABLES

2.1 Values of $\beta_n l$ 21
2.2 Magnetic properties of the elemental magnets and select alloys. . 29

5.1 Measured cantilever and tip magnet properties. 85

LIST OF FIGURES

1.1 Illustration of the prototypical MRFM experiment. 4
1.2 Definition of dimensions in an MRFM experiment. 5
1.3 The static, oscillating, and effective magnetic fields seen in the rotating reference frame. 7
1.4 Cantilevered beam with dimensions labeled. 10
1.5 Schematic of an ultra-sensitive magnet-tipped cantilever operating in the "pendulum" geometry. 11
1.6 Effects of tip cross-section area and surface material on surface-induced dissipation. 16

2.1 Shapes of first three transverse bending modes of a singly clamped cantilever of rectangular cross-section. 21

3.1 Side-view illustration of the key steps of the fabrication process. 31
3.2 Photo of a completed wafer. 32
3.3 Illustration of the KOH etching process 38
3.4 Magnet on test structure after KOH etch 39
3.5 Illustration of the SF_6 silicon underetch process 41
3.6 Series of SEM images showing increase in magnet underetch with increasing etch time 42
3.7 Result of too-narrow silicon cantilever tip 43
3.8 Illustration of the silicon oxide pillars method for overhanging magnet fabrication. 44
3.9 Overhanging gold nanorod on a polysilicon cantilever, produced using the silicon oxide pillar fabrication method. 46
3.10 E-beam alignment mark 49
3.11 Optical stepper alignment mark 50
3.12 SEM of photoresist contamination after critical point drying. . . . 51
3.13 Silicon oxide membrane distortion and cracking after the through-wafer etch. 52
3.14 Illustration of handler wafer attached to SOI wafer. 54
3.15 Examples of handle silicon under- and over-etching 56
3.16 Damage to cobalt magnets from buffered hydrofluoric acid etch. 57
3.17 Cantilever contamination from precipitated products of the silicon oxide hydrofluoric acid etch. 58

4.1 SEM images of wafer with incomplete through-wafer silicon etch. 62
4.2 SEM images of wafer with no front protective silicon oxide, after 360 μm of silicon has been removed in the through-wafer etch. . 64
4.3 SEM images of wafer with no front protective silicon oxide, after completion of through-wafer etch. 64
4.4 SEM images of wafer with silicide coming from metal/silicon interface. 65

4.5 Ta barrier layer test structure, annealed with no protective silicon oxide. . . . 67
4.6 Ti barrier layer test structure, annealed with no protective silicon oxide. . . . 67
4.7 Cr barrier layer test structure, annealed with no protective silicon oxide. . . . 68
4.8 SEM image from tantalum barrier layer test after annealing . . . 69
4.9 SEM image from tantalum barrier layer test without annealing . 69

5.1 Illustration of geometry for cantilever magnetometry measurements. . . . 77
5.2 Data from cantilever magnetometry analysis of an overhanging nickel nanomagnet. . . . 79
5.3 Cantilever with nickel magnet tip with a ~ 50 nm overhang. . . . 81
5.4 Cantilever with non-overhanging nickel tip magnet 82
5.5 SEM analysis showing partially or completely absent tip magnets after cantilever fabrication. . . . 82
5.6 SEM imaging challenges with ultra-sensitive cantilever 84
5.7 ESR-MRFM data collected with cantilever B, and associated modeling to estimate the size of the magnetically dead layer. . . 88
5.8 Dissipation versus tip-sample separation data collected with cantilever B over a gold coated polymer sample, at 4.2K. 89
5.9 Dissipation versus tip-sample separation data collected with a bare silicon cantilever, over a gold surface at 4.2K. . . . 89
5.10 Power spectrum of frequency noise measured for cantilever B at various heights over a gold coated polymer surface. . . . 91
5.11 Frequency noise power at the optimum frequency versus height measured for cantilever B. . . . 92

6.1 SEM image of a 1 millimeter long cantilever. . . . 95
6.2 Sub 50 nm wide cobalt magnet test structure fabricated on a silicon wafer. . . . 97
6.3 Cobalt blob formation. . . . 99
6.4 Spatial map of EDS analysis of cobalt blob 99
6.5 SEM of protective silicon oxide layer deposited by ALD 101
6.6 Chlorine contamination under ALD deposited protective silicon oxide layer. . . . 101

CHAPTER 1

INTRODUCTION

Scanning tunneling microscopy, developed in 1982, is generally considered the first scanned probe microscopy technique [1]. Since that time, a plethora of related scanned probe techniques have been developed, spawning numerous articles, books, conferences, and a Nobel Prize. In all these techniques the probe itself is key. Nowhere is that more true than in the technique known as Magnetic Resonance Force Microscopy (MRFM). The thrust of this work was to develop a new protocol for fabricating ultra-sensitive, magnet-tipped silicon oscillators for MRFM.

The MRFM technique was first proposed by John Sidles in 1991 [2]. Although current implementations of MRFM are quite different than the method proposed in that article, the fundamentals of the experiment have little changed. The core of the experiment is the detection of electron or nuclear spins in a sample through an interaction between the spin and a nearby magnetic particle. This interaction is mechanically detected by using the interaction energy to drive a sensitive oscillator, in the form of a cantilevered beam. Using the magnetic field gradient produced by the magnetic particle, and the techniques of magnetic resonance, the orientation of the spins can be manipulated, allowing spins to be addressed based on differences in spatial location and isotopic characteristic. This allows for three-dimensional, isotopically specific imaging.

The most exciting promise of MRFM, and also the most cited, is the isotopically specific, atomic-resolution structural determination of a single biomolecule. Biomolecule structure determination is currently done by X-ray crystallography, conventional NMR, and cryo-electron microscopy. However,

all of these techniques have limitations that prevent their use on a large range of biomolecules. X-ray crystallography requires that the sample form an ordered solid, which has been difficult to achieve for many molecules. Conventional NMR is limited to structural determination of proteins of less than ~ 150 kilodaltons, because of the increasing difficulty in interpreting the chemical coupling data with increasing molecule size. And cryo-electron microscopy requires that there be some degree of symmetry to the molecule structure, as the three-dimensional image is reconstructed from many two-dimensional projections. All three are bulk techniques, which can present the problem of acquiring the isolated target compound in sufficient volume for analysis. Cryo-electron tomography can give structure determination of a single molecule, but since many two-dimensional images of the same molecule must be taken to generate the full three-dimensional structure, resolution is limited by radiation damage [3].

MRFM can be done on a single molecule (and thus does not require a crystalline form), and is only limited in molecule size and complexity by the rate of image acquisition. The interaction of the magnetic particle with the molecule causes no damage to the molecule. To date, the highest resolution MRFM image was produced by Degen and coworkers [4], of a tobacco mosaic virus with 4 nm resolution. Although not high enough to determine structural information, this is nonetheless equivalent to the best resolution available in the only comparable single biomolecule imaging technique, cryo-electron tomography [5,6].

Another often cited application for MRFM is as the read/write device in a solid state quantum computer [7]. A final use is ferromagnetic resonance force microscopy for structure determination of magnetic thin films, of extreme interest to the magnetic media storage industry [8].

This work seeks to address two limitations in prior MRFM work. First, all prior MRFM experiments have either attached the magnetic particle to the force detection cantilever manually, or placed the sample on the cantilever and located the magnetic particle nearby. Affixing the sample to the cantilever severely restricts the types of samples that can be imaged. For example, it would be nearly impossible to integrate a working transistor onto the end of the extremely pliant cantilevers needed for highest force sensitivity, or a single protein in a cryo-protectant that must remain at cyrogenic temperatures during loading. Hand-gluing of the magnetic particle limits the minimum particle size that can be attached due to the difficulty in manipulating small particles. While the magnet size can be reduced somewhat further by focused ion beam milling, this too is limited to a minimum size of $\sim$ 100 nm from ion beam damage [9].

In this work, a batch fabrication method for producing nanoscale magnets on attonewton sensitivity cantilevers is presented and validated by cantilever magnetometry and force-detection of electron spin resonance. This represents a significant improvement over past cantilevers used in MRFM experiments, both in the magnet size and the method of production. Further, careful design of the cantilever tip geometry has resulted in a surface-induced force noise much lower than the cantilever used in the highest sensitivity MRFM experiment to date [4].

As a final note on the potential importance of MRFM, biomolecule structure determination by x-ray crystallography and conventional NMR are both subjects of Nobel Prizes, to Roderick Mackinnon in 2003, Max Perutz and Sir John Cowdery Kendrew in 1962, Dorothy Crowfoot Hodgkin in 1964, and Kurt Wüthrich in 2002.

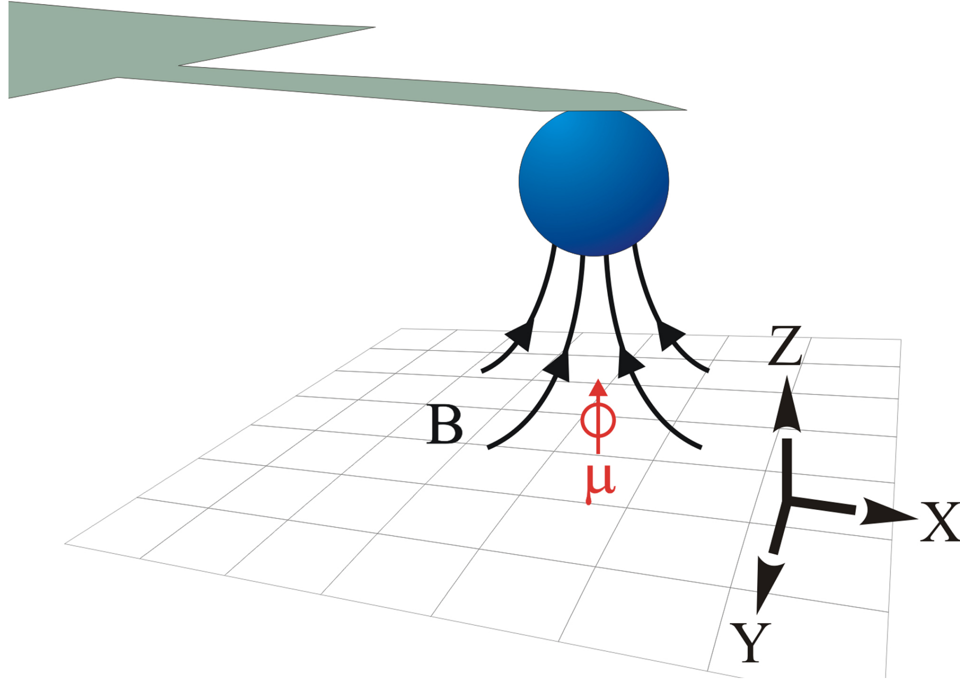

Figure 1.1: Illustration of the prototypical MRFM experiment.

1.1 Signal Calculation

In a prototypical MRFM experiment, a magnetic particle on the end of a cantilever is brought close to a spin (Figure 1.1). The force between the spin and the particle is a function of the spin's magnetic dipole moment $\boldsymbol{\mu}$ and the gradient of the particle's magnetic field $\mathbf{B}$ (the following equations are in SI units):

$$\mathbf{F} = (\boldsymbol{\mu} \cdot \nabla)\mathbf{B} \tag{1.1}$$

A large, homogeneous external magnetic field $\mathbf{B}_z$ is applied parallel to the z-axis. This causes the magnetic moment of both the spin and the magnetic particle to lie along the z-axis. For a spherical magnetic particle the magnetic field at a point directly below the particle is

$$\mathbf{B}_{\text{Static}} = \frac{2\mu_0 M a^3}{3(a+d)^3} \tag{1.2}$$

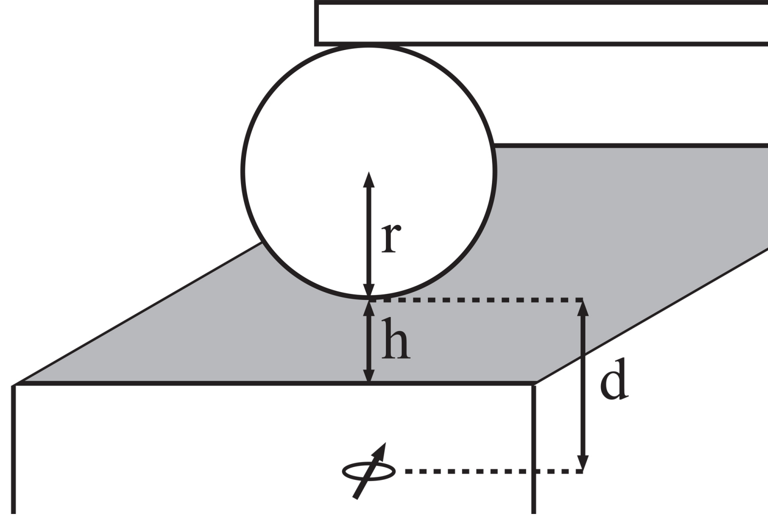

Figure 1.2: Definition of dimensions in an MRFM experiment. A magnet of radius **a** attached to a cantilever is directly above a spin in a sample. The closest edge of the magnet is a distance **d** from the spin, and a distance **h** above the sample surface.

Thus equation 1.1 becomes

$$\mathbf{F} = \mu \cdot \frac{\partial \mathbf{B}_z}{\partial z} = -2\mu\mu_0 M \frac{a^3}{(a+d)^4} \tag{1.3}$$

where μ is the magnitude of the spin magnetic moment $\boldsymbol{\mu}$ along the z axis, μ_0 is the permeability of free space, M is the magnetization of the magnetic particle, here lying along the z axis, a is the magnet diameter, and d is the distance between the spin and the closest edge of the magnet (Figure 1.2). For a 30 nm diameter iron sphere a mere 5 nm away from a single proton spin with a saturation magnetization $\mu_0 M_{\text{sat}} = 2.2$ T, the interaction force is 1.3 attonewtons. For comparison, this is approximately 200 times smaller than the force between two electrons one μm apart. From this rough calculation, it can be seen that the magnetic particle will need to be very small and brought extremely close to the spin, and the cantilever used for detection of resonance to be extremely sensitive. Equation 1.3 also shows that for a given spin-sample distance, there is an

optimal magnet diameter, comparable to this separation distance [10, 11].

The above example treats a spin in isolation, but in a real sample there will be many spins interacting with the magnetic particle. Equation 1.1 still holds true for each spin, but the total force is the sum of interactions of the j individual spins in the sample

$$\mathbf{F}_{tot} = \sum_{j} (\boldsymbol{\mu}_j \cdot \nabla)\mathbf{B}_j \tag{1.4}$$

1.2 Spin Manipulation

In order to isolate the force contribution of spins in a given region of the sample, spin manipulation techniques must be employed. The following is a brief summary of spin manipulation. The goal of this section is to explain the technique for spatial resolution of spins in MRFM experiments, and thus further the design criteria for MRFM mechanical oscillators. For a much more complete description the reader is referred to reference [12].

As noted above, a spin placed in a static magnetic field $\mathbf{B_{static}}$, with magnitude B_{static}, will tend to align with that field and precess around the field direction with frequency $\omega_0 = \gamma \mathbf{B}_{\text{static}}$, called the spin's resonance frequency. γ is the gyromagnetic ratio of the spin. As in Figure 1.1 $\mathbf{B_{static}}$ lies along the z-axis. A second magnetic field is applied to the system, along the x axis, and which is linearly polarized and oscillates in magnitude according to $\mathbf{B}_x(t) = 2B_1 \cos(\omega_{\text{rf}} t)$, where ω_{rf} is the frequency of oscillation.

The field $\mathbf{B}_x$ can be decomposed into two circularly polarized fields, each of magnitude B_1, rotating in opposite directions around the z axis. For simplicity

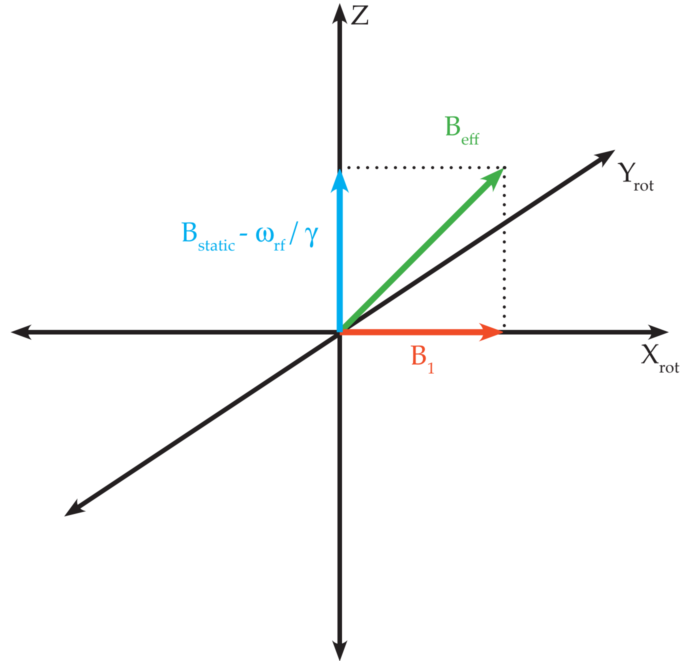

Figure 1.3: The static, oscillating, and effective magnetic fields seen in the rotating reference frame.

the spin system is often considered in a reference frame that rotates around the z axis at frequency ω_{rf}. In the rotating frame, one component of $\mathbf{B}_x$ is static, while the second is seen rotating at 2 ω_{rf} and can be disregarded. Hereafter the kept component of $\mathbf{B}_x$ will be called $\mathbf{B}_1$.

As stated above, in the rotating frame both $\mathbf{B}_{\mathbf{static}}$ and $\mathbf{B}_1$ are static, and the magnitude of $\mathbf{B}_{\mathbf{static}}$ has been decreased by the amount $\omega_{\mathrm{rf}}/\gamma$. The two fields produce an effective field $\mathbf{B}_{\mathbf{eff}}$ which is their vector sum (Figure 1.3).

If $\mathbf{B}_1$ is turned on with $\omega_{\mathrm{rf}} \gg \omega_0$, and then the frequency slowly lowered, the spins will follow $\mathbf{B}_{\mathbf{eff}}$. If ω_{rf} is swept to the condition that $\omega_{rf} \ll \omega_0$, then the spins will have been inverted from their initial direction. This technique is called

"adiabatic fast (or rapid) passage"(ARP). In an MRFM experiment, such a spin inversion or "flip" will result in a change in the direction of the force between the spins and the tip magnet, thus changing the deflection of the cantilever. If the magnetic field $\mathbf{B}_{\mathbf{static}}$ is homogeneous across a sample, then an ARP inversion or "sweep" will flip all of the spins. However, if $\mathbf{B}_{\mathbf{static}}$ is inhomogeneous, only the spins in regions where the resonance condition $\gamma B_{static} = \omega_{rf}$ is met will be flipped by an ARP inversion.

In MRFM, the magnetic particle at the end of the cantilever is the source of this field inhomogeneity. The region in the sample in which the resonance condition is met is called the sensitive slice. The size of the slice, and distance from the tip magnet, depends on the magnitude of the gradient of the tip magnet, and the frequency of ω_{rf}. In an MRFM experiment in which ARP is used to invert the spins, the thickness of the slice depends on the width $\Delta\omega$ of the frequency sweep, as well as the field gradient. It is this slice that allows spins in a specific region of a sample to be manipulated independently from the rest of the spins in the sample. Applying an ARP with this inhomogeneous $\mathbf{B}_{static}$ will invert only the spins within the sensitive slice, which will modulate the total force between the spins in the sample and the tip magnet.

In an MRFM experiment, there are two general methods by which an ARP sweep can be enacted [13]. In the "stationary cantilever, swept field" method the ARP is enacted as described previously, with the cantilever held stationary while the frequency of $\mathbf{B}_1$ is swept through resonance. In the "moving cantilever, steady field" method the oscillating field $\mathbf{B}_1$ is applied at a single frequency while the cantilever (and thus the tip magnet) is moved. The ARP sweep is created by changing the magnetic field experienced by the spin. Thus,

not only is a large tip magnet field gradient necessary to generate a sufficient interaction force, but it is also required for sharp spatial resolution.

1.3 Thermally-limited Detection Limit

For a simple harmonic oscillator, motion induced by thermal energy sets the lower bound on force detection. This relationship will be considered in more detail in chapter 2. Here it shall be simply stated that the noise-limited minimum detectable force, is given by:

$$F_{\min} = \sqrt{\frac{4kk_B T B}{\omega_0 Q}} \tag{1.5}$$

k, ω_0, and T are the spring constant, resonance frequency and temperature of the cantilever, k_B is Boltzmann's constant, and B is the measurement bandwidth. Q is the "quality factor" of the oscillator, a unitless value that represents the ratio of the energy lost in each cycle of oscillation to the total energy of oscillation. From this equation, it can be seen that an ideal oscillator would have a very small spring constant and a high frequency and quality factor. $F_{\min}$ can also be written as

$$F_{\min} = \sqrt{4k_B T B\,\Gamma} \tag{1.6}$$

where

$$\Gamma = \frac{k}{\omega_0 Q} \tag{1.7}$$

is the friction coefficient. The friction coefficient is related to the frictional force by $F_{\text{frict}} = \Gamma\dot{x}$ where $\dot{x}$ is the cantilever velocity.

For the first mode of a cantilevered beam, the spring constant and frequency can be written in terms of the beam's dimensions, and the density ρ and Young's

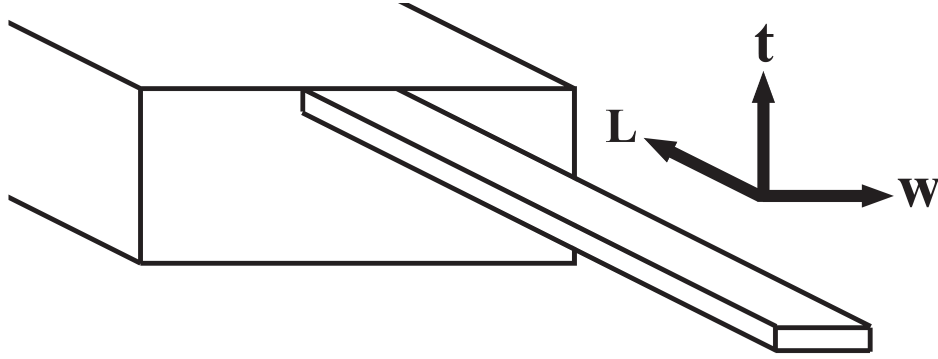

Figure 1.4: Cantilevered beam with dimensions labeled.

modulus E of the beam's material (See section 2.1). F_{min} then becomes:

$$F_{\text{min}} = 1.007 \sqrt{\left(\frac{wt^2}{l}\right)(E\rho)^{\frac{1}{2}} \left(\frac{k_B T B}{Q}\right)} \tag{1.8}$$

where width w, thickness t and length l are defined as shown in Figure 1.4. The cantilever bends in the direction of the thickness. The optimal beam for sensitive force detection, ignoring for the moment the factors which influence Q, would be long, narrow, and very thin, made of low density, pliant material. The cantilevers produced in this work were all 340 nm thick, 5 μm wide, and 200 or 395 μm long, fabricated from single crystal silicon.

1.4 Pendulum Geometry

The requirements of a close approach to the spin, and an extremely pliant cantilever, requires careful consideration of the geometry of the MFRM experiment. As diagrammed in Figure 1.1, the force of magnet/spin interaction is normal to the plane of the sample, and thus to detect this force the cantilever will need to be pliant in this direction. However, operating in this "AFM" geometry and

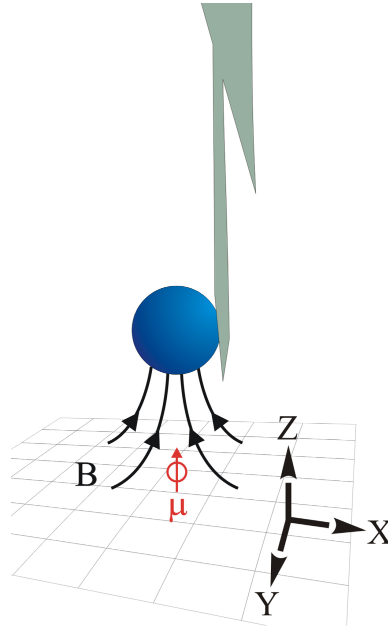

Figure 1.5: Schematic of an ultra-sensitive magnet-tipped cantilever operating in the "pendulum" geometry.

at extremely small separation, van der Waals forces between the sample and both the magnetic particle and the cantilever body will cause the cantilever to be drawn into the sample surface. To prevent this "snap-in" the cantilever must operate with its long axis parallel to the sample surface normal, such that the cantilever tip oscillates parallel to the plane of the sample (Figure 1.5). This change in geometry solves the "snap-in" problem, but now the net force along the sensitive direction of the cantilever is zero, for a static homogeneous spin distribution. To enable detection of the spin in this "pendulum" geometry, new protocols have to be implemented.

1.5 Sample Versus Magnet on Cantilever

Before describing the detection protocols developed to work in the pendulum geometry, a further issue of experiment geometry must be covered. As shown in Figures 1.1 and 1.5 the magnetic particle is attached to the cantilever. However, the formulas governing spin/magnetic particle interaction do not specify which is on the cantilever. Indeed, the first successful MRFM experiments, and the most sensitive to date, were implemented in a "sample on cantilever" geometry [4, 13] in which the sample was affixed to the tip of the cantilever, and then brought close to a stationary magnetic particle. It was not until six years after the first force-detection of electron spins that an experiment with the "magnet on cantilever" geometry was reported [14], and a further 6 years until NMR-MRFM was detected in this geometry [15]. In this work, the magnet-on-cantilever geometry was selected. The selection of geometry is not a trivial choice, and there are significant advantages and challenges to each approach. However, for applicability to the widest range of samples, the magnet-on-cantilever geometry is superior. This is because of the extreme difficulty of attaching the sample to the extremely fragile and pliant cantilevers required of MRFM, especially if it is necessary to employ cryoprotection techniques to study biological samples [16], or if objects such as functioning transistors are desired to be studied.

1.6 Signal Detection in Pendulum Geometry

For a cantilever in the pendulum geometry, as illustrated in Figure 1.5, the net force of a uniform distribution of spins on the cantilever is zero. This is because the relevant field gradient, $\frac{\partial B_z}{\partial x}$, is such that the force of spins to the left of the can-

tilever are equal and opposite to the force of spins to the right of the cantilever. For a spherical magnetic particle polarized along the z direction,

$$B_z = \mu_0 M a^3 \frac{-x^2 - y^2 + 2z^2}{(x^2 + y^2 + z^2)^{\frac{5}{2}}} \tag{1.9}$$

and

$$\frac{\partial B_z}{\partial x} = 3\mu_0 M a^3 \frac{x(x^2 + y^2 - 4z^2)}{(x^2 + y^2 + z^2)^{\frac{7}{2}}} \tag{1.10}$$

For spins directly below the cantilever $x = 0$, and consequently the field gradient, and thus the force, is zero. There are two methods to detecting spins in the pendulum geometry: use of force detection, but of a non-uniform spin polarization; or use of force gradient detection, in which the interaction of the spins is with the second derivative of the tip magnetic field. The first method was demonstrated by Mamin *et al.* [9], who observed the naturally occuring stochastic fluctuations of rotating frame spin polarization using the force-based OScillating Cantilever-driven Adiabatic Reversals (OSCAR) detection protocol. Thus far in this text, the spin polarization described has been the thermal polarization, the tendency for spins to align along a magnetic field which is driven by the slight energy difference between the aligned and anti-aligned states.

The Cantilever-Enabeled Readout of Magnetic-Inversion Transients (CERMIT) method, developed by the Marohn group at Cornell, is able to record both statistical and thermal net spin polarizations, by detecting the interaction between the spins and the second derivative of the tip magnet field [15]. This interaction results in a shift in the force gradient experienced by the cantilever, changing its effective spring constant and manifesting as a shift in the cantilever resonance frequency (although it could also be detected as a change in the cantilever amplitude, if the cantilever driving energy was held constant). In the review article by Kuehn et al [11], a comparison was made between the ther-

mally limited signal to noise ratio for these two detection methods, for a system with a spherical tip magnet of radius a, with a distance d between the closest portion of the magnet and a single spin. In each formula, the conditions of detection have been optimized as to spin lateral position (directly under the tip for CERMIT, slightly to the side for OSCAR) as well as cantilever displacement amplitude.

$$\mathrm{SNR}_{\mathrm{CERMIT}} = \frac{1}{F_{\mathrm{min}}} \frac{\mu \mu_0 M}{a} \left(\frac{a}{a+d} \right)^4 \tag{1.11}$$

$$\mathrm{SNR}_{\mathrm{OSCAR}} = \frac{1}{F_{\mathrm{min}}} \frac{1.16\, \mu \mu_0 M}{a} \left(\frac{a}{a+d} \right)^4 \tag{1.12}$$

From these equations, it can be seen that both detection methods give approximately the same signal to noise ratio. It can also be seen that to achieve a reasonable SNR for a single spin, as in the AFM geometry the tip magnet must be very small, very close to the sample, and the combined measurement noise no larger than the thermal limit. To achieve a SNR of 1, with one second of signal averaging, using the same iron sphere and magnet-sample separation as in the AFM geometry example of section 1.1, the cantilever sensitivity would need to be approximately 0.7 attonewtons for a single proton spin, and approximately 450 attonewtons for a electron spin, using either detection scheme.

1.7 Surface Noise

At extremely small cantilever-sample separations and cryogenic temperatures, thermal noise is usually not the dominant noise source in MRFM experiments [4, 9, 15, 17, 18]. Rather, surface-induced phenomena raises the noise floor above the thermal limit, in both amplitude and frequency shift detection schemes. In

frequency-shift detection protocols such as OSCAR [19] and CERMIT [15], frequency noise or "jitter" is the relevant noise term, while for amplitude-shift detection protocols, dissipation is the relevant noise term. After careful study of this phenomena over polymer surfaces, Kuehn *et al.* showed that over polymer films, surface-induced dissipation was the result of fluctuating electric fields near the sample interacting with charges on the cantilever tip. The fluctuating electric fields were caused by thermal fluctuations in the position and orientation of dipoles in the polymer film [20]. Yazdanian *et al.* extended this to explain surface-induced jitter as arising from fluctuating electric field gradients from the polymer film interacting with charges on the tip [21, 22].

However, over metal surfaces, an experimentally-derived explanation for either of these types of noise is lacking. Experimental observations made by Kuehn (unpublished), taken over a gold surface at 298K found that dissipation decreases with decreasing cantilever cross-section (Figure1.6(a)), and that dissipation is less for metal than for silicon tips of the same size (Figure 1.6(b)). He also discovered that both of these effects decreased to below the thermal noise level when the cantilever tip was moved > 100nm from the surface. In this work the cantilevers were of the same type as described in reference [20]. The as-fabricated cantilevers had silicon tips with a radius of curvature of $\sim$ 50 nm. One of these was used as the silicon tip cantilever in Figure 1.6(b). For the small metal tip in Figure 1.6(a) and the metal coated tip in Figure 1.6(b), a thin layer of platinum was evaporated onto the tips of some of these cantilevers, again as described in [20]. For the large tip in Figure 1.6(a), a $\sim 5\ \mu$m metal sphere was manually attached to a bare silicon cantilever tip with epoxy. This led to the hypothesis that fabricating the magnetic particles so that they extended past the leading edge of the silicon cantilevers, and then making the magnetic particles

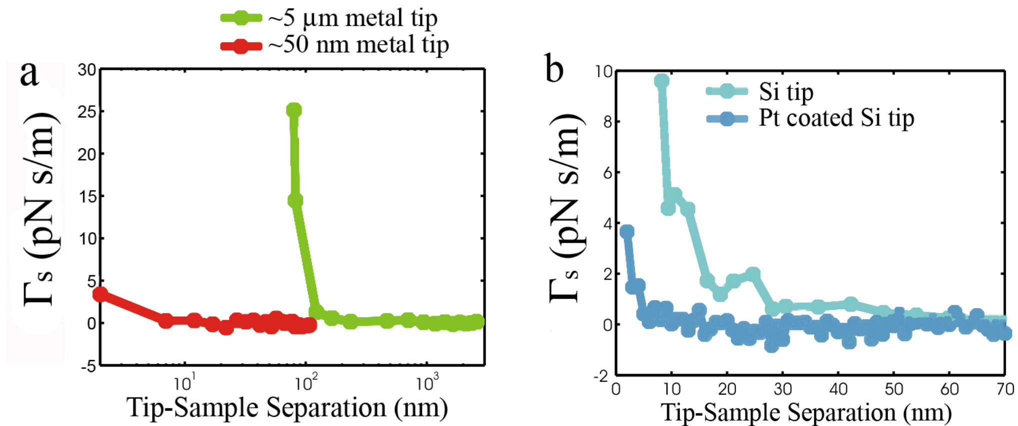

Figure 1.6: Effects of tip cross-section area and surface material on surface-induced dissipation.

as small as possible, would significantly decrease the surface-induced dissipation. Although Kuehn did not take similar jitter measurements, it was hoped that the same design would also lead to a decrease in jitter.

1.8 Other Cantilever Applications

Cantilever frequency fluctuations give information about electric field gradient fluctuations in the sample [22, 23]. This connection has been used to determine the dielectric fluctuation spectrum for a variety of thin polymer films [24]. Quantifying local electric field gradients in these experiments, as well as measurements of local polarizability [25], requires an accurate model of tip charge, e.g. tip-sample capacitance. While reasonable agreement between theory [26] and experiment [20, 22] has been obtained in studies of dielectric fluctuations, work to date has relied on approximating the cantilever tip as a sphere. The cantilever tips described in this work have a much better defined geometry than the tips used in the experiments of references [20, 22, 25]. The tips presented

here should therefore allow a far more accurate estimations of tip-sample capacitance and therefore a far more reliable determination of local electric field gradient fluctuations than has been possible to date.

The extremely low surface-induced dissipation of these cantilevers, combined with the nanoscale tip magnets, makes them useful in magnetic dissipation force microcopy [27,28]. In this technique, local magnetic energy dissipation is recorded as the change in the cantilever quality factor. This technique can be used to image magnetic domain structures, distinguish micromagnetic walls that cannot be differentiated by conventional magnetic force microscopy, and determine domain walls in samples with weak stray fields. Decreasing the surface-induced dissipation would improve the signal quality in magnetic dissipation force microscopy experiments.

These cantilevers could be used to directly study surface-induced dissipation to study charge density [29] or dopant density [30] in semiconductors.

One could also imagine using the metal tips of these cantilevers for tip-enhanced Raman spectroscopy [31], either as an isolated experiment, or in combination with one of the other methods suggested above.

In this chapter MRFM has been introduced as a promising technique for creating three dimensional images of electron and nuclear spins with nanometer resolution. The key technology to enable this imaging is the magnetic tip, which must be placed on the cantilever for use with the widest range of samples. Surface-induced force noise has also been introduced, the dominant noise source in the highest sensitivity MRFM experiments to date. Several other uses for such magnet or metal tipped attonewton-sensitivity cantilevers have also

been presented, which would significantly advance the state-of-the-art in materials characterization.

Chapter 2 summarizes the key mechanical properties of cantilevered beams, including frequency and intrinsic dissipation, and the magnetic properties of selected magnetic materials used in this work or in other MRFM experiments. Chapter 3 describes the fabrication protocol developed for batch-fabrication of nanometer magnets on cantilevers, highlighting the particular challenges of alignment, creating a magnet that extends past the leading edge of the cantilever, and preventing wafer contamination and cantilever breakage in the final "release" steps of the fabrication process. Metal silicides and silicide prevention, the largest challenge overcome in implementing the fabrication process, is covered in Chapter 4. Methods and results of analysis of cantilever and magnet properties for the devices produced in this work are presented in Chapter 5. These results include electron spin resonance signal from the smallest magnet used in a magnet-on-cantilever MRFM experiment to date, and surface-induced dissipation data showing that the same cantilever can approach 8 times closer to the sample surface, with the same amount of dissipation, as the cantilever used in the most sensitive MRFM data yet published [4]. Finally, in Chapter 6 preliminary work for several possible improvements to the cantilevers produced in this thesis are presented.

CHAPTER 2

BACKGROUND

2.1 Cantilever Dynamics

The cantilevers fabricated in this work can be modeled as a singly-clamped beam of rectangular cross-section. In this section formulas to derive the mode shapes and associated frequencies of such a beam are given [32].

The derivation of cantilever properties follows the Euler-Bournoulli beam theory, which requires that the length l of the beam be much larger than than either the thickness t or width w. This is because the theory assumes that the shear deformation of a cross-sectional segment of the beam, caused by the deflection of the beam, is much less than the displacement of that segment from its un-bent location. The calculations here are for the dynamic bending of the beam, and assume that there is no force applied to the beam.

For a singly-clamped beam, the mode shape is given by

$$D[x] = \cosh(\beta_n x) - \cos(\beta_n x) - (\sinh(\beta_n x) - \sin(\beta_n x))\frac{\sinh(\beta_n l) - \sin(\beta_n l)}{\cosh(\beta_n l) + \cos(\beta_n l)} \quad (2.1)$$

where $D[x]$ is the displacement of the cantilever at position x when it is at its maximum deflection, x is the distance from the clamped end of the cantilever beam, and $\beta_n l$ is value of the nth solution of

$$\cosh(\beta_n l)\ \cos(\beta_n l) = -1 \quad (2.2)$$

Note that the value of each β_n is not a constant but will change with cantilever length l. The values of $\beta_n l$ for the first three modes are given in Table 2.1. Figure 2.1 plots the shapes of the first three modes. The horizontal axis is the frac-

tional position from the clamped end of the cantilever at x=0, and the vertical axis is the arbitrary mode amplitude. The modeshapes have been normalized so that their maximum displacement is the same. For an actual cantilever, the amplitude of the higher modes is much smaller than that of the first mode.

For cantilevers used in force detection, the magnitude of an applied force is determined from the size of cantilever deflection caused by the force and the cantilever spring constant. If, as with the cantilevers fabricated in this work, the location at which the force is applied is not the same as the location at which cantilever displacement is measured, a conversion is needed to determine the actual size of the displacement. This is done by using equation 2.1 to calculate the ratio of the mode amplitude at the location the force is applied to the mode amplitude at the location where the displacement is measured.

For cantilevers of the type studied in this work, which, because of their high quality factor, exhibit resonance over a very narrow band of frequencies, the effect of higher order vibrations can be eliminated by proper frequency filtering. Nonetheless, to minimize any noise coming from the second order mode (which should have the second largest amplitude), the motion of the cantilever should be monitored at a point $x = 0.783l$, where the second mode has a node. The resonance frequency ω_n of the nth mode is given by

$$\omega_n = \frac{(\beta_n l)^2 t}{l^2} \sqrt{\frac{E}{12\rho}} \tag{2.3}$$

where E is the Young's modulus and ρ is the density of the cantilever material. The thickness t is the cantilever dimension parallel to the direction of motion.

The calculation of the spring constant for higher order modes is more complicated, as the effective mass of the cantilever decreases with increasing mode

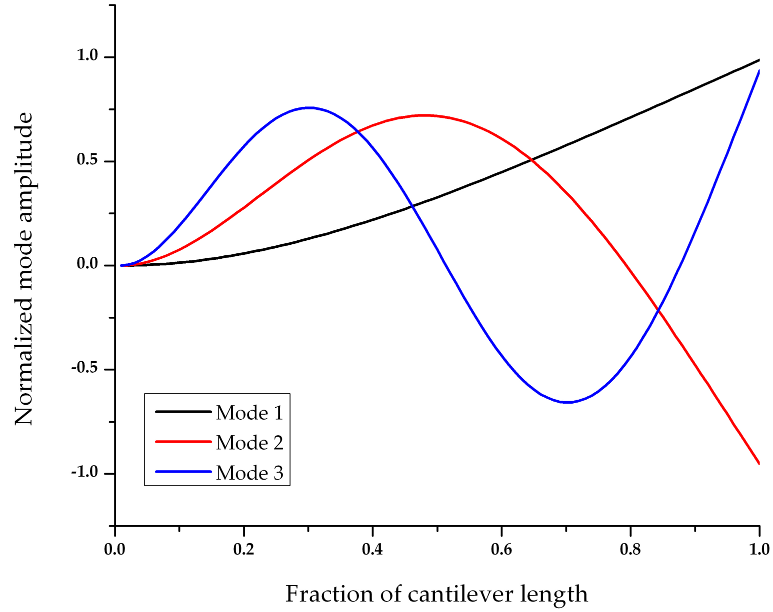

Figure 2.1: Shapes of first three transverse bending modes of a singly clamped cantilever of rectangular cross-section.

Table 2.1: Values of $\beta_n l$ which solve equation 2.2; n = 1, 2, and 3, for Mode 1, 2, and 3, respectively.

	Mode 1	Mode 2	Mode 3
$\beta_n l$	1.8751	4.6941	7.8548

number. The formula for the spring constant of the first order mode is given in equation 2.4, taking the effective cantilever mass as $\frac{l\,w\,t\,\rho}{4}$ [10]. The formulas for the effective mass of the second through fourth modes can be found in Ref. [33]. For the first order mode, the spring constant relates the magnitude of a point force to the displacement of the cantilever, by that force, at the location the force is applied.

$$k = 1.03 \frac{w\,t^3\,E}{4\,l^3} \tag{2.4}$$

2.2 Prior Cantilever Fabrication Work

The realm of fabrication dedicated to making microscale mechanical structures from silicon and other materials has existed for over 30 years. A review published by Petersen [34] in 1982, considered a seminal work in microelectromechanical system (MEMS) fabrication, is a solid launching point for the reader looking for a broad overview. The basic cantilever fabrication process implemented in this work was developed by Stowe *et al.* [35] at Stanford. He developed a process for batch-fabricating very thin, long, and flexible cantilevers from single crystal silicon-on-insulator wafers. Addition of magnets to the tips of these cantilevers was not integrated in the batch fabrication process, but was done serially, using a knife-edge shadow evaporation.

The work by Jenkins [36] integrated definition of nanometer-scale nickel magnets onto these cantilever, as well as translated the Stowe process to work on the tools available at the Cornell Nanoscale Science and Technology facility. But, for application to MRFM, the Jenkins fabrication procedure must be completely revised to produce magnets which *overhang* the cantilever leading edge, to mitigate surface-induced force noise.

2.3 Other Methods for Producing Overhanging Magnets

A variety of methods, primarily from the magnetic force microscopy community, have been developed for placing magnetic materials on cantilevers. As it is necessary, for force noise mitigation, for the magnet to extend beyond the leading edge of the cantilever, MFM tip magnet protocols fabrication protocols

involving evaporation onto the cantilever sidewall [37], evaporation of metal followed by focused ion-beam milling (FIB) [38–41], and evaporation through a nanopore [42] are poorly suited for making high-sensitivity MRFM tips. Further, as explained in section 1.1, imaging subsurface spins requires a tip diameter comparable to the sample depth. Thus the ideal fabrication protocol must be able to produce a range of magnet diameters, in the tens to hundreds of nanometers range.

Hand-gluing of magnet particles to cantilevers [14,15,19,43], and subsequent modification by FIB [19,43], have been successfully used in MRFM experiments. Hand-gluing has so far been limited to $\sim 1\mu$m particle size, which can be improved to $\sim$ 150 nm magnet diameter by FIB. The limit on hand-gluing comes from the difficultly of manipulating small particles, while the limit on FIB modified magnets is a result of damage from the ion beam[1] .

Other techniques to produce magnet tips which extend from the cantilever body are: electron beam deposition of metals from organic precursors [45–48]; electron beam deposition of carbon [49, 50] followed by blanket evaporation of metal [51–54]; evaporation onto a carbon nanocone [55] or carbon nanotube [56, 57]; using the magnetic catalyst particle at the end of a multiwalled carbon nanotube [58, 59] or silicon nanowire [60]; and dielectrophoretic assembly of magnetic nanorods [61]

Unfortunately, all of the approaches given are serial, require significant human control, and yield tips with large device-to-device variation. Magnet uniformity between devices will play an extremely important role as MRFM is extended towards routine imaging of 3-D structures, as the shape of the tip mag-

[1]Modern FIB's may allow for milling with as few as 5 nm of damage by using lower beam energies [44].

net field gradient is needed for accurate image reconstruction [4, 62–64]. Although arrays of singly-clamped metallic nanowires have recently been batch-fabricated in high yield using electric-field and capillary-force assisted self assembly [65, 66], it is hard to see how to integrate the required sacrificial electrodes into the rest of the protocol for ultrasensitivie cantilever fabrication.

2.4 Intrinsic Dissipation and Quality Factor

The intrinsic dissipation of a mechanical oscillator determines the magnitude of the thermal driving of the oscillator and thus the minimum force detectable in a thermal noise limited system. Physically, the intrinsic dissipation term Γ_I is a coefficient of friction. It is a function of the spring constant k, resonance frequency ω_0, and Q, the mechanical quality factor[2].

$$\Gamma_I = \frac{k}{\omega_0 Q} \tag{2.5}$$

The quality factor Q is a measure of the energy lost per cycle of movement, as a proportion of the total energy of the oscillator.

$$Q = 2\pi \frac{\Delta U}{U} \tag{2.6}$$

The factor of 2π is necessary for continuity with the other measure of Q, the width of the resonance peak at half maximum, divided by the resonance frequency.

$$Q = \frac{\Delta f}{f_0} = \frac{\Delta\omega}{\omega_0} \tag{2.7}$$

[2]Each mode of oscillation will have a different dissipation value. All data presented in this work is for the lowest order mode of oscillation.

Equation 2.6 can be used to derive the form of the dissipation term Γ_I, using equations for the energy of the system, and for the energy lost per cycle.

$$U = \frac{1}{2}kx_0^2 \tag{2.8}$$

Where x_0 is the maximum oscillator displacement. The energy lost per cycle ΔU is given by

$$\Delta U = \text{Dissipation term} * \text{velocity} * \text{distance traveled in one cycle} \tag{2.9}$$

$$\Delta U = \text{Dissipation term} * (\omega_0 x_0)(\omega_0 x_0 \frac{2\pi}{\omega_0}) \tag{2.10}$$

Combining equations 2.6, 2.8, and 2.10 we see that

$$\text{Dissipation term} = \frac{k}{\omega_0 Q} \equiv \Gamma_I \tag{2.11}$$

Significant research effort has been conducted into the physical phenomena that determine the quality factor of mechanical oscillators. Some of the mechanisms proposed are: thermoelastic loss [67–69], anharmonic couplings with other cantilever modes, viscous damping [68, 70], crystalline lattice defects [71], dopants and other interstitial atoms [71, 72], and effects related to the crystallographic orientation of the material [73].

A general trend of decreasing Q with decreasing oscillator volume has been observed both for series of nearly identical devices [74], and for devices of different construction [71]. Surface-related phenomena are believed to be responsible for this trend, for as device size shrinks into the micro and nanometer scale, the proportion of material in a surface versus bulk state changes dramatically. In addition to general surface phenomena [73, 75], some of the surface-related mechanisms proposed for changes in quality factor are surface defects and roughness [72, 76–79], layers of SiO_2 [68, 80–82], or layers or particles of other adsorbates [72,78,79, 83–85].

A few methods of enhancing the quality factor of devices, beyond changing device material or design, have been developed. They include annealing, either in UHV [79, 82] or in various gas environments [77], flash heating [73], and deposition of specific organic monolayers [78,84]. The thermal processes are questionable for integration into the fabrication protocol for magnet-on-cantilever single-crystal silicon oscillators, due to the likelihood of silicide formation. The addition of organic monolayers is more tractable with the fabrication protocol, and should be considered.

A fairly recent development has been the use of materials under very high tensile stress. Extremely high quality factors have been reported in such devices [86]. However it is the intrinsic dissipation, rather than the more commonly cited frequency Q product, that is the figure of merit for force detection, and it remains to be seen whether these tensile stress oscillators will have a lower dissipation.

In the fabrication process developed, efforts to obtain high quality factor oscillators have concentrated on preventing damage to the silicon. This includes using high-quality silicon oscillators produced via the Smartcut™ process, preventing exposure of the silicon to any etchant species and to any form of plasma, and thorough cleanliness when removing material such as organic resists and protective silicon oxides.

Finally, though many advances have been made in the fabrication of extremely sensitive mechanical oscillators, in MRFM and indeed all force and frequency detection experiments operating at extremely small sample-oscillator separations, surface related effects, dissipation and jitter, will likely be the dominant noise source. Previously it was shown that to minimize such surface noise,

it is crucially important that the magnetic tip overhang the leading edge of the cantilever. A protocol for producing such cantilevers is presented in the next chapter.

2.5 Magnetic Materials

The ideal material for the tip magnet would have a high saturation magnetization, be easy to integrate into a silicon fabrication process, and be resistant to chemical modification. Depending on the details of the MRFM experiment, high coercivity may be desired. The types of magnetic material can be broadly divided by composition into elemental and alloy magnets, the latter category further divided into low and high coercivity materials.

High-coercivity can be important considerations for MRFM experiments conducted with a small (generally speaking, on the order of less than a Tesla) static magnetic field. In experiments with a small static magnetic field, high coercivity materials are measured to have lower magnetic field fluctuations than low coercivity materials [37], which can increase the relaxation rate T_1 of nearby spins [19]. Additionally, magnetic field fluctuations at the cantilever resonance frequency, for a magnet-tipped cantilever, can increase the cantilever energy dissipation Γ when oscillated in a magnetic field. This can be mitigated by operating the cantilever with the magnetic field applied along the width of the cantilever [15, 87]. Members of the high coercivity category include the rare-earth magnetic alloys, such as praseodymium-iron-boron and neodymium-iron-boron based compounds. Although rare-earth magnets have been used in numerous MRFM experiments, including the first detection of a single electron

spin [18], they will not be considered in this section because of expected extreme difficulty in their use in a batch fabrication process. Use of high-coercivity rare-earth elements would require extensive effort to develop a process that could integrate the necessary tight control over material composition, sintering to create the crystalline lattice, and if they are to be used with the static magnetic field near or below their saturation field, magnetization of the material.

There are four elements that exhibit ferromagnetism above 273 K: cobalt, nickel, iron, and gadolinium. Several other rare-earth elements, including terbium, dysprosium, and holmium, are ferromagnetic at cryogenic temperatures. These materials can be alloyed, in cases resulting in compounds that have a higher saturation magnetization than either of the component elements. As explained in Chapter 1 a high saturation magnetization M_{sat} is important in creating a large field gradient. In most MRFM experiments the applied homogeneous magnetic field is sufficient to reach the saturation magnetization of the tip magnet.

In table 2.2 the M_{sat}, coercivity H_c, and Curie temperature T_{Curie} are presented for several magnetic materials. Note that these are properties for the bulk materials - at the nanometer scale of the magnets produced in this work, these properties may be somewhat different. Most significantly, the bulk coercivity may be less important than other factors such as crystalline and shape anisotropy in determining the low-field behavior of the magnet [88], and thus is omitted for the elemental magnets.

All the room temperature elemental magnets are susceptible to reactions with oxygen [94] and silicon(See Chapter 4). Iron in particular suffers from rapid oxidation, as its oxide is easily removed and thus does not act as a suf-

Table 2.2: Magnetic properties of the elemental magnets and select alloys. The temperature for the M_{sat} values of $SmCo_5$ and $N_2Fe_{14}B$ were not given in the reference cited. Table data are from Refs. [89–93].

	M_{sat} (T, 0K)	M_{sat} (T, 290K)	H_c (T)	T_{Curie} (K)
Nickel	0.66	0.61		631
Cobalt	1.80	1.76		1400
Iron	2.19	2.15		1043
Dysprosium	2.989	N / A		180
Gadolinium	2.116	1.09		293
$SmCo_5$		1.07*	0.877	1020
$N_2Fe_{14}B$		1.61*	1.41	585
CoFe(35:65)		2.45	$20\text{-}60 \times 10^{-4}$	

ficient barrier to further oxidation. To obtain the best performance, the magnet material should be protected from contact with oxygen, whether by storage in an inert atmosphere on encapsulation in a protective medium.

In this chapter properties of cantilevered beams, including oscillation dynamics and intrinsic dissipation, have been discussed. Properties of several ferromagnetic materials, and methods for fabricating overhanging magnets on cantilevers have also been covered. In the next chapter, the batch fabrication process developed in this dissertation to produce overhanging magnets on single crystal silicon cantilevers is covered, with several of the more challenging aspects of that process given in detail.

CHAPTER 3

FABRICATION

3.1 Process Outline

A detailed recipe for the fabrication processes developed in this work are given in the appendices. The following process outline gives a descriptive documentation of the fabrication steps. Following this outline, several of the steps and fabrication considerations are covered in more detail.

1) **Wafers**

The process began with a single crystal silicon-on-insulator (SOI) wafer (Figure 3.1(a)). The wafers used had a device silicon thickness of 340 nm, a buried silicon oxide thickness of 400 nm, and a handle silicon thickness of 550 μm. The wafer radius was 100 mm. With a few exceptions early in the process development, all wafers used in this work had $\langle 100 \rangle$ oriented device and handle silicon.

Though the design of the cantilevers, especially for the magnet and cantilever tip, changed through the course of this work, the basic wafer layout remained the same. On each wafer 21 identical chips were produced, arranged in a 3-5-5-5-3 pattern (Figure 3.2). Each chip had 10 dies, and each die had a single cantilever[1]. The wafers were supplied by SOITEC, and produced using the Smartcut^{TM} process [95]. This method of SOI production has very high (specified better than 40 nm) device silicon thickness uniformity, and does not exhibit any strain in the device silicon that could cause undesired cantilever curling. It

[1] It is possible, and perhaps advantageous to place more than one cantilever on each die, thus increasing the total possible cantilever yield of the wafer.

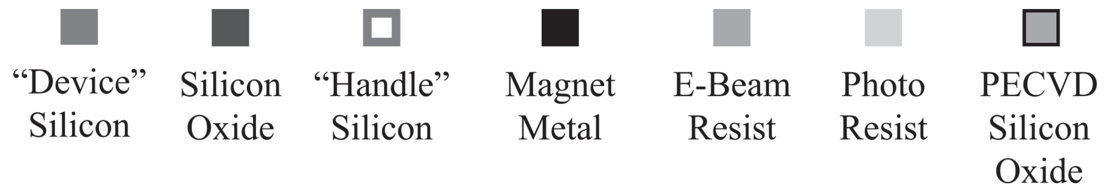

Figure 3.1: Side-view illustration of the key steps of the fabrication process.

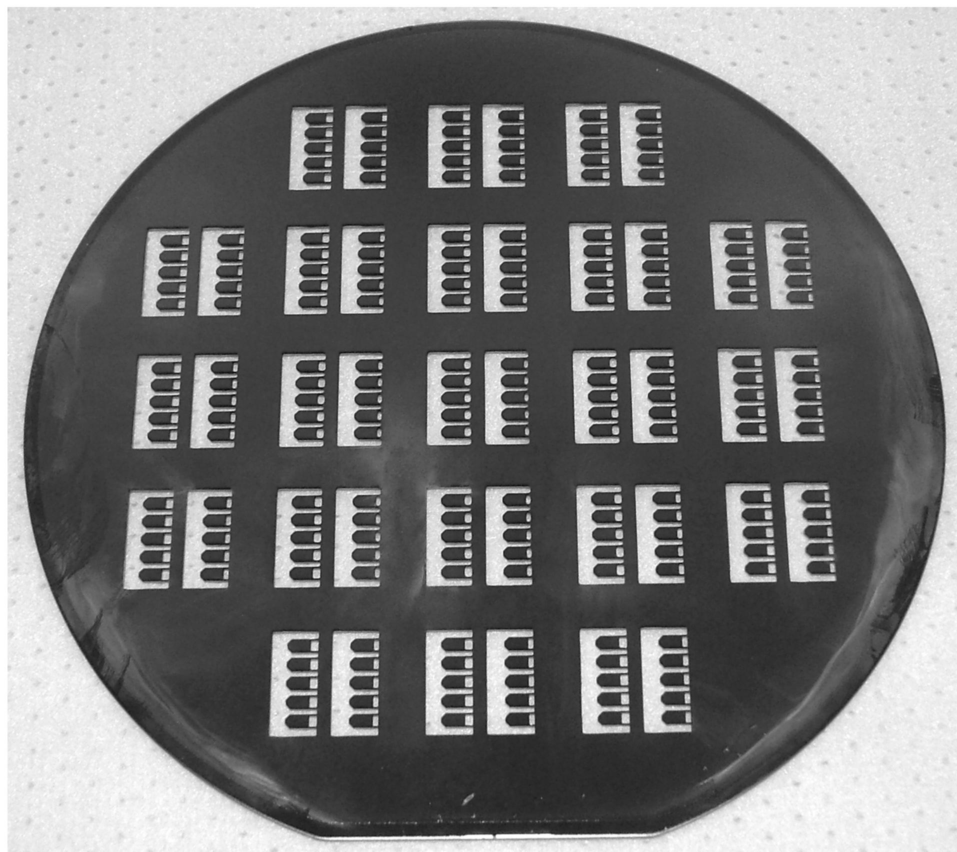

Figure 3.2: Photo of a completed wafer, showing the chip and die arrangement. The individual dies within each chip are visible, however, the cantilevers are too small to see.

is felt that this wafer production process is less likely to result in lattice damage from ion implantation during wafer production, as compared to the alternative SIMOX production process. This is because the Smartcut process involves hydrogen ion implantation, while the SIMOX process uses larger, heavier oxygen ion implantation.

The device layer resistivity was 14-22 $\Omega/\ \mathrm{cm}^2$, giving a boron dopant density of 6 - 9 $\times\ 10^{14}\ \mathrm{cm}^{-3}$. This is currently the only available dopant density from SOITEC in 100 mm wafers. Wafers with a lower doping level could increase the quality factor of produced cantilevers [71,72], and should be used if available.

2) **Alignment Marks**

100 nm thick platinum alignment marks, used for all but the last lithographic step, were created using a lift-off process involving electron beam lithography and electron-gun evaporation. The alignment mark pattern was first defined in e-beam resist. Poly(methyl methacrylate) (PMMA) resists were used, of either 495,000 or 950,000 molecular weight. Typically a resist bilayer was used to prevent deposition of metal on the resist sidewall during the e-gun evaporation [96]. A 5 nm layer of chrome was deposited to promote metal adhesion, followed by 100 nm of platinum. Finally, the resist was removed in a methylene chloride and acetone solvent bath, lifting off all the excess metal on top of the resist. Section 3.3 will cover the importance and design of the alignment marks.

3) **Magnet Deposition**

Magnets were defined and deposited in same manner as the alignment marks, using either cobalt or nickel as the magnet material (Figure 3.1(b)).

4) **Magnet Underetch**

Three methods were developed to overhang the magnet from the silicon cantilever leading edge (Figure 3.1(c)). These are covered in detail in section 3.2. The method used most successfully, sulfur hexafluoride (SF_6) isotropic plasma etching, is detailed below. A U-shaped "etch pit" was defined by electron-beam lithography (Figure 3.5). The pit was placed such that the magnet lay in-between the arms of the U, and was 50 nm from the base of the U. A SF_6 reactive ion plasma etch was then used to remove the silicon in the etch pit, at the same time undercutting the silicon beneath the magnet.

5) **Cantilever Body Definition**

The cantilever body was defined by optical projection lithography, and etched through the device silicon layer using the same etch process as the magnet underetch (Figure 3.1(d)). The alignment marks for the backside lithography step were also created in this step.

6) **Protective Front Silicon Oxide**

A ~ 1.6 μm thick silicon oxide layer was deposited over the front of the wafer via plasma-enhanced chemical vapor deposition (PECVD), using SiH_4 and N_2O precursor gases (Figure 3.1(e)). This layer provided mechanical protection for the magnets and cantilevers during the rest of the fabrication process.

7) **Backside Silicon Oxide**

A 2 μm silicon oxide layer was deposited on the back of the wafer, in the same manner as the front silicon oxide. The back silicon oxide layer was used, after patterning, as a hard etch mask for a portion of the through-wafer silicon etch, described below.

8) **Backside Resist**

A thick, ~ 10 μm photoresist layer was pattered on the back of the wafer by contact optical lithography. This pattern was aligned to the features on the front of the wafer via twinned-optics in the contact lithography tool observing both sides of the wafer. This resist defined the "flop hole" underneath the cantilevers.

9) **Backside Silicon Oxide Etch**

The backside silicon oxide was etched, with the backside resist as the etch

mask, using a CHF_3 reactive ion plasma etch.

10) **Through-wafer Silicon Etch**

The flop holes were etched through the handle silicon using a Bosch process anisotropic silicon etch. The Bosch deep reactive ion etch uses a three-step process to achieve nearly vertical etching. In the first step, a thin layer of fluoropolymer is conformally deposited over the entire face of the wafer. Directional sputtering by argon ions removes the fluoropolymer from horizontal surfaces. A high power SF_6 etch in the third step etches only the horizontal surfaces, the vertical surfaces being protected by the fluoropolymer. The Unaxis 770 tool used in this work achieved silicon etch rates of 1-3 μm/minute with about 200:1 selectivity to the photoresist and silicon oxide etch masks. For the first 425 μm of the etch, a higher-speed ($\sim$ 3 μm/minute) etch recipe was used. Etch depth was monitored by periodic measurement using a mechanical stylus profilometer. For the final 100 μm of silicon etching, the photoresist mask was removed, leaving the silicon oxide mask, and a "handle" wafer was attached to the front of the SOI wafer using a removable paste[2]. During this second etch phase, a less aggressive ($\sim$ 1 μm/minute) etch recipe was used, to decrease wafer heating. The etch process was terminated when either all of the silicon had been removed from the flop holes, verified by optical microscopy, or when cracking in the silicon oxide membranes over the flop holes became excessive.

11) **Buffered Hydrofluoric Acid Silicon Oxide Etch**

The "handler" wafer was removed by hand before the buried and front silicon oxide layers were removed in a hydrofluoric acid etch, buffered with ammonium fluoride(buffered oxide etch or BOE) (Figure 3.1(e)). The buffer keeps

[2] AI Technology Cool Grease 7016.

the concentration of etch species, and thus the silicon oxide etch rate, constant during the etch process. Removal of the silicon oxide layers supporting the cantilevers over the flop holes “releases” the cantilevers, and so is often referred to as the release etch.

12) **Critical Point Wafer Drying**

The released cantilevers are extremely fragile, and meniscus forces during air drying from solution would cause the cantilevers to curl and break. A carbon dioxide critical point dryer (CPD) was used to remove the wafers from solution without passing through a defined liquid/vapor transition. The wafers must be transferred from the water-based BOE solution to isopropanol (IPA) before being placed into the CPD. For safety reasons the wafers must be transferred into a water bath between the acid and IPA solutions. To prevent the wafers from prematurely drying, a custom-made Teflon transfer carrier was used. This carrier kept the wafer under a small amount of liquid while moving between baths. Because of this solution transfer, numerous water and IPA baths were needed to ensure that none of the acid or etch products end up in the first IPA bath (see section 3.5.4 for contamination caused by insufficient water baths), and that a minimal amount of water remained in the IPA solution when the wafer was transferred into the CPD.

3.2 Methods to Produce Overhanging Magnets

Three methods were developed to create the desired magnet overhang on the cantilever leading edge. Two of the methods removed the silicon under the magnet after the magnet was deposited, while the third method fabricated the

magnet partially over a sacrificial silicon oxide pillar.

3.2.1 Magnet Undercut Via Anisotropic Silicon Etching

The use of the anisotropic silicon etchant potassium hydroxide (KOH) to produce overhanging magnets was first proposed by Sean Garner. KOH etches ⟨100⟩ and ⟨110⟩ silicon crystallographic planes significantly faster than the ⟨111⟩ plane. This selectivity can be used to rapidly etch silicon into well-defined shapes with extremely smooth finished surfaces, but requires careful consideration of the crystallographic structure of the material with respect to the desired feature orientation [97]. The process developed in this work used SOI wafers with a ⟨111⟩ orientation. After magnet deposition, a thin silicon oxide was deposited over the wafer by PECVD to protect the silicon that will become the cantilever body from the etch. A specially shaped feature, the 'etch pit', (Figure 3.3) was patterned by electron beam lithography around the magnet. The placement of the etch pit was such that the sides were either parallel or perpendicular to ⟨111⟩ plane. As shown in fig. 3.3(a) the ⟨111⟩ planes run horizontally. This alignment was accomplished by careful loading of the wafer into the e-beam tool, so that the major flat of the wafer is parallel to the loading pins in the e-beam tool wafer chuck. The major flat in a 4 inch, ⟨111⟩ silicon wafer is along the ⟨110⟩ plane, and so in this way proper crystallographic orientation of the 'etch pit' was accomplished. This feature was etched through the thin silicon oxide layer and the device silicon via a timed reaction ion plasma etchs, stopping at the buried silicon oxide layer. The e-beam resist was removed before the KOH etch. This proved critical, as the etch did not proceed when the resist was left in place. The wafer was then placed in a 70 °C KOH solution for 70 seconds. This

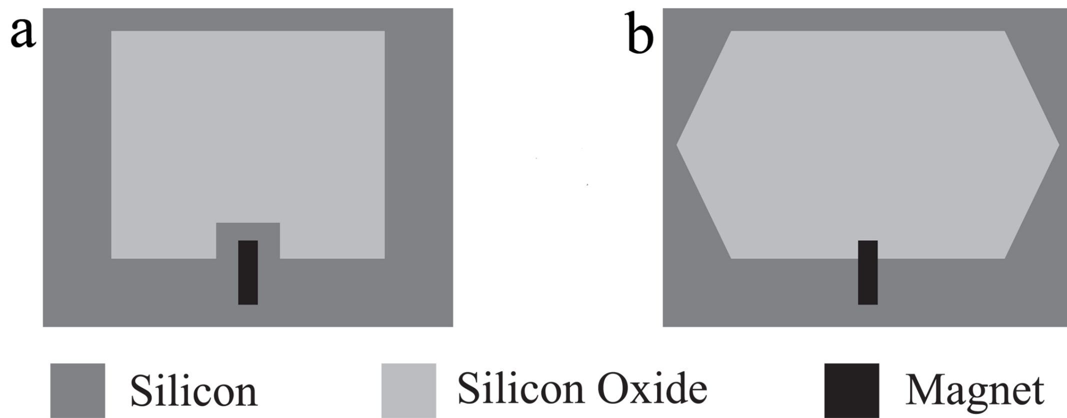

Figure 3.3: Illustration of the KOH magnet underetch. (a) The magnet and etch pit after CF_4 etching, but prior to the KOH etch. The thin protective silicon oxide has been omitted for clarity. (b) The same feature after the completion of the KOH etch.

etched the ⟨100⟩ and ⟨110⟩ faces exposed during the CF_4 etch. For the peninsula of silicon surrounding the magnet, the two sides etched in and met in the center, under the magnet, before a continuous ⟨111⟩ face formed, thus removing the silicon under the magnet. At the leading edge of the silicon, under the magnet, the ⟨111⟩ face is re-entrant, leaving an advantageous knife-edge profile.

An SEM of a magnet overhanging a test structure, after the KOH etch, is shown in Figure 3.4. Although this method produced excellent results on test wafers, the unavailability of ⟨111⟩ SOI wafers required a different process to be developed.

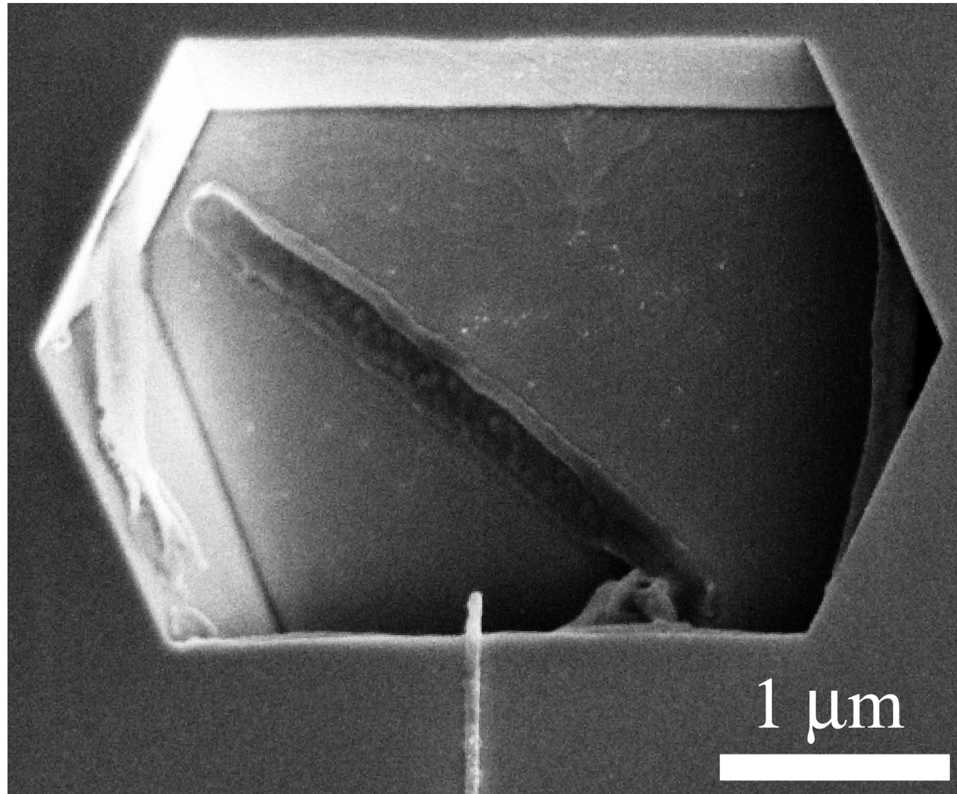

Figure 3.4: SEM image of a 50 nm magnet overhanging a etch pit test structure after a KOH etch. The thin protective silicon oxide was removed in a BOE etch prior to imaging.

3.2.2 Magnet Undercut Via Isotropic Plasma Etching

A process using an isotropic SF_6 reactive ion plasma etch to underetch the magnets was developed in response to the unavailability of $\langle 111 \rangle$ SOI wafers. Initially, the lithographic mask used for this process was the same shape as that used for the KOH etch. Later, the peninsula of silicon was lengthened to ~ 6 μm, giving the resist pattern a "U" shape. This in turn allowed the silicon tip of the cantilever to be defined by e-beam lithography, rather than optical lithography as used for the rest of the cantilever body. This allowed for very narrow silicon tips to be defined with high registration to the magnets, and also reduced

the required alignment tolerance for the cantilever body lithographic step from 250 to 2500 nm. The reduced required alignment tolerance greatly decreased the alignment demands on the optical stepper.

The use of SF_6 eliminated the need for deposition of a thin protective silicon oxide before the magnet underetch, and also eliminated the hassle of integrating a wet chemical process. In most ways, the SF_6 process is superior to the KOH etch. Its only deficiencies is that it leaves a vertical or slightly non-vertical cantilever leading edge, and the etched silicon faces are much rougher than those which resulted from the KOH etch.

The U-shaped etch pit was defined in e-beam resist so that the end of the magnet is 50 nm from the base of the U (Figure 3.5(a)). As the etch proceeds, the silicon (shown in red) is etched down towards the buried silicon oxide layer (grey), as well as laterally under the resist (Figures 3.5(b) and (c)). The vertical portion of the etch stops when the buried silicon oxide is reached, but lateral etching continues until the process is terminated (Figure 3.5(d)). By varying the total etch time, the degree of undercut or overhang can be controlled (Figure 3.6). As the amount of undercut is increased, the width of the U must increase as well. If not, the silicon tip of the cantilever can become too narrow to support the magnet (Figure 3.7).

The etch is very rapid – typical etch times were between 30 and 40 seconds – and so steps must be taken to ensure uniform etch conditions for each run. This was done by using the same etch tool for every wafer, and running etch chamber cleaning and seasoning[3] processes prior to each etch. Also, after any

[3]In the seasoning process, the same recipe that will be used to etch the wafer is run for several minutes on an empty etch chamber. This ensures that any reaction between the walls of the etch chamber and the etch gasses will be completed before starting the actual wafer etch, thus increasing etch uniformity.

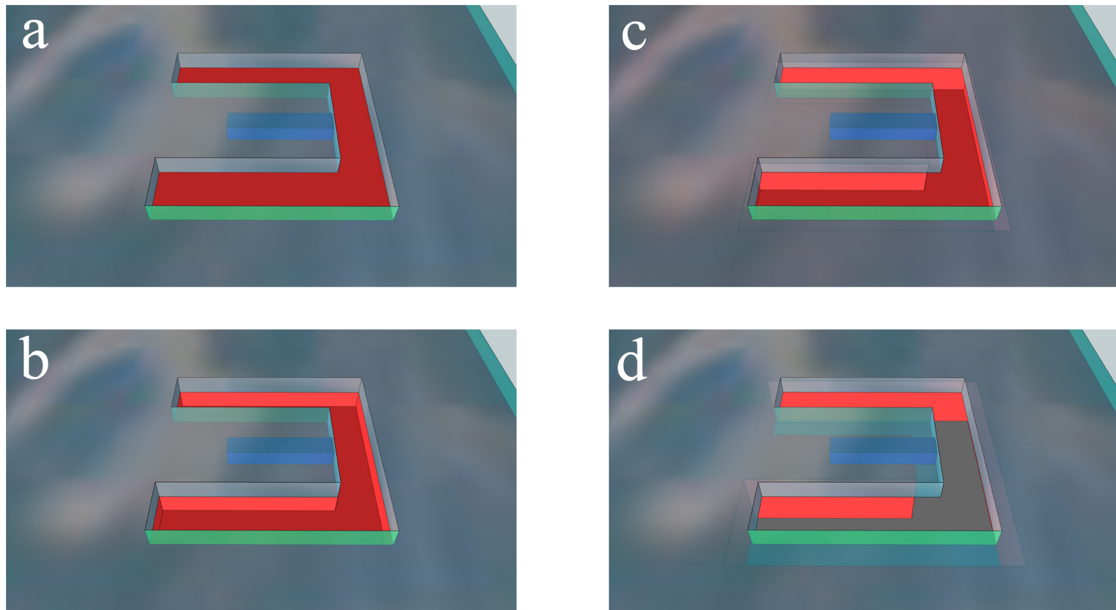

Figure 3.5: Conceptual illustrations showing the progression of the SF_6 silicon underetch. The magnet (dark blue) is visible under the semi-transparent e-beam resist (light blue). In (a), before the start of the etch, the end of the magnet is 50 nm from the edge of the resist. As the etch proceeds the silicon etch reaches the front of the magnet (b) and starts to undercut it (c). Once the silicon oxide layer (grey) is reached (d) the vertical etching stops, but the lateral etching continues until the process is terminated.

major change to the etch tool, such as replacement of the RF generator or etch chamber liner, a test wafer was run to check the underetch rate.

There was early concern that the fluorine ions would damage the magnet metal. However, the magnet is only exposed to the ions on the bottom, with the top and sides protected by the resist layer. The bottom of the magnet is protected by the chrome adhesion layer. So minimal direct exposure to or damage from the fluorine ions is expected.

Some work was also done on using a plasma-free xenon difluoride isotropic

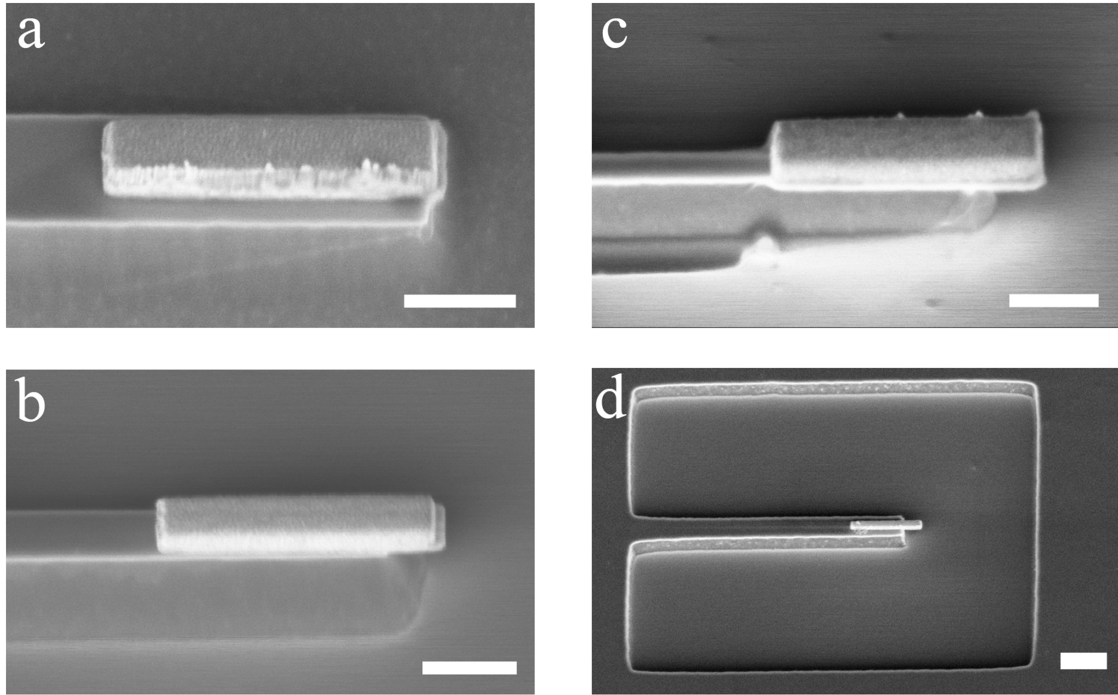

Figure 3.6: SEM images illustrating the SF_6 magnet underetch process. Images a-c show the increase in length of overhang with increasing etch time. (a), (b), and (c) were taken on a test wafer after 10, 20, and 30 seconds of etching. The magnets are all nickel, 600 nm wide by 200 nm thick. Scale bar is 400 nm. (d) A larger view of the etch pit - the long tongue of silicon on which the magnet rests will become the tip of the cantilever body. Scale bar is 1 μm.

silicon etch. This etch was very hard to control because of the extremely high etch rate, and was not pursued after initial test runs.

3.2.3 Silicon Oxide Pillars

A third method was developed in which the magnets would not be exposed to any etch, plasma or wet, until the final BOE release. In this process, the magnets

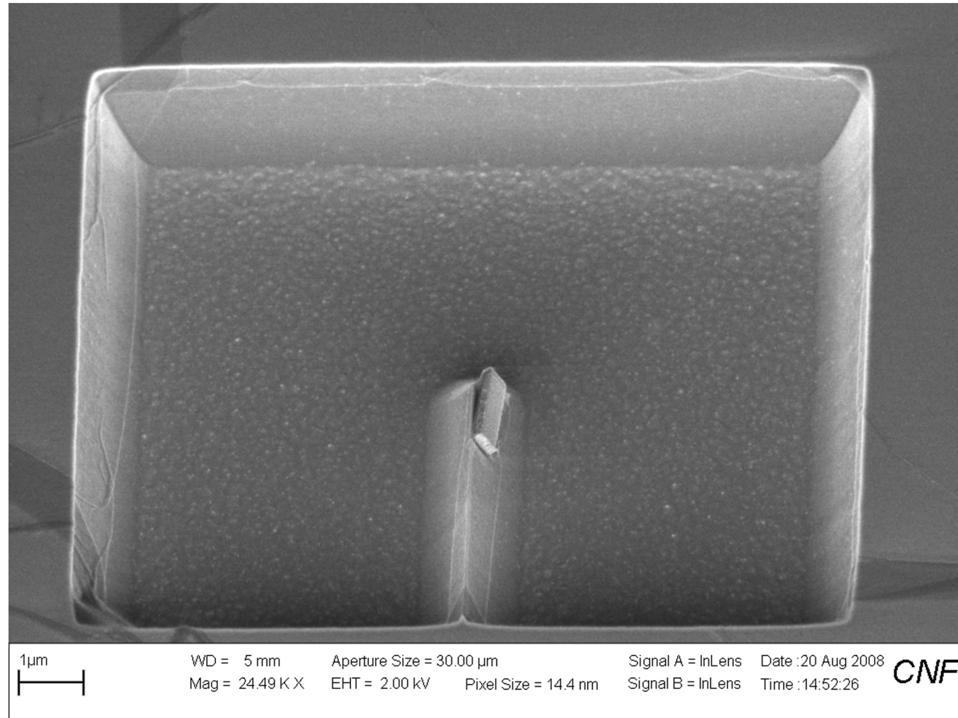

Figure 3.7: SEM image of a SF_6 test etch pit on a standard (non-SOI) wafer after a 40 second etch. The etch pit lithographic pattern was not properly sized for the degree of silicon underetch, leading to the magnet falling onto the side of the "silicon tip". Because there is no buried silicon oxide layer to terminate the vertical silicon etching, this etch pit is significantly deeper than those generated on SOI wafers.

were fabricated partially over silicon oxide pillars that extended through the device silicon layer to the buried silicon oxide layer, and whose tops were polished to be coplanar with the top of the device silicon. The pillars were created by localized thermal oxidation of the device silicon, as follows. After creating etched alignment marks (described in section 3.3), a thin layer of silicon nitride was deposited and patterned using e-beam lithography and CHF_3 reaction ion plasma etching (Figure 3.8(a)). The exposed silicon was oxidized in a high temperature furnace, with the silicon nitride film protecting the rest of the wafer

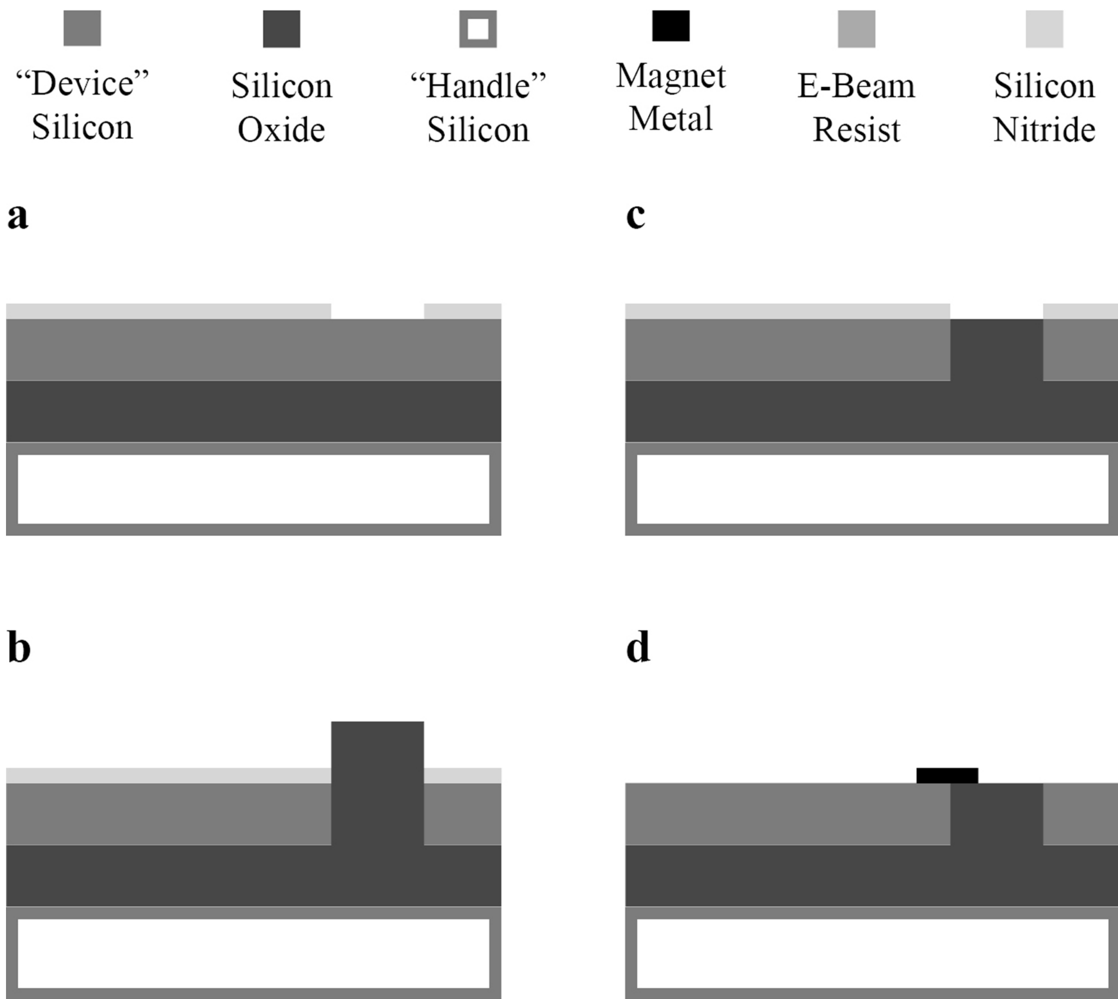

Figure 3.8: Cut-away illustration of the fabrication of silicon oxide pillars conformal with the device layer silicon. (a) After alignment marks have been created (not shown), a thin silicon nitride layer is deposited on the wafer, patterned, and used to define the width and length of the oxide pillars. (b) The exposed silicon is thermally oxidized. The increase in volume from the growing silicon oxide causes it to extend above the top of the silicon nitride. (c) The wafer is planarized by chemical mechanical polishing, removing the excess silicon oxide. (d) The silicon nitride is removed, and the magnet deposited partially over the pillar.

(Figure 3.8(b)). After silicon oxide growth, the wafer was planarized by chemical mechanical polishing (CMP), using a polishing slurry that was selective to silicon oxide. In the polish step, the silicon nitride layer acted as both a protective layer for the device silicon and a stop layer for the polishing process. The polish step was calibrated so that the silicon oxide would be polished below the top of the silicon nitride, so that when the the silicon nitride was removed in a phosphoric acid etch, the top of the silicon oxide pillar would be conformal with the top of the device silicon (Figure 3.8(d)). The rest of the fabrication process, starting from the magnet deposition, was the same as described in section 3.1, skipping the underetch step.

The outcome of this process is similar to that of the damascene process, which is widely used in semiconductor manufacturing. In the damascene process, holes are first etched into a layer of material A. These are filled by a blanket deposition of material B. The excess material B is removed by CMP, leaving pillars of material B conformal with material A. Silicon oxide pillars grown by thermal oxidation have been used to make sacrificial supports for pressure sensor fabrication [98] but does not appear to have been implemented with single crystal SOI wafers.

In addition to limiting the etchant exposure of the magnets, because of the large size of the silicon oxide pillars this process could allow for μm-sized two-dimensional structures of arbitrary complexity to be produced overhanging the end of an attonewton-sensitivity cantilever.

To date, this process has been demonstrated on polycrystalline SOI wafers, producing cantilevers with overhanging gold nanorods (Figure 3.9). The use of polycrystalline SOI wafers during development was due to the cost and avail-

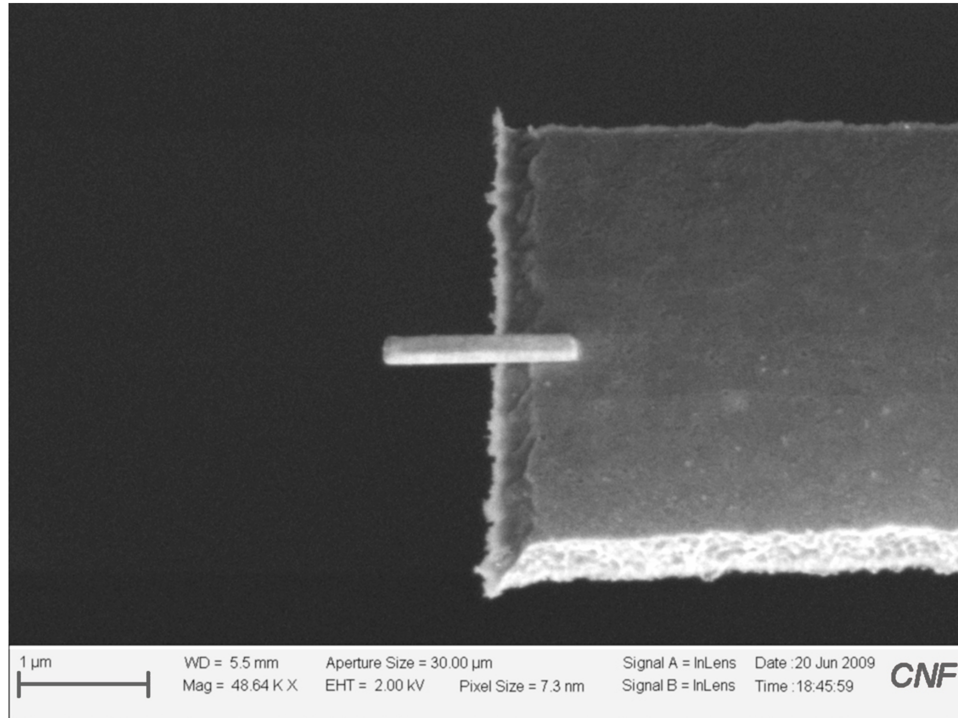

Figure 3.9: A 200 by 100 nm gold nanorod fabricated on a polysilicon cantilever. The nanorod overhang was created using via a sacrificial silicon oxide pillar. The length of unsupported nanorod is ~1300 nm.

ability of single crystal SOI wafers. Transferring the developed process to single crystal SOI wafers will be straightforward.

3.3 Alignment Challenges

In the process described in section 3.1, every lithographic step must be in good registry with all preceding lithographic steps. The alignment tolerances vary from 50 nm for the separation between the magnet and the etch pit, to several μm for the placement of the flop holes on the back of the wafer. With the exception of the backside pattern, all processes align to marks defined in a single write

by e-beam lithography. This alignment strategy takes advantage of the spatial accuracy of the e-beam tool, and eliminates additive alignment error. The shape and size of the marks are set by the requirements of each tool, and separate marks are used for each tool. Marks can be constructed either from material deposited on the wafer, or trenches etched into the wafer. The requirements of mark construction are excellent visibility to all the tools used, resistance to modification in processing, and minimal defects and line edge roughness.

Except for the silicon oxide pillars process, all of the wafers and test structures created in this work used deposited marks. This is because generating etched marks proved extremely difficult with the SOI wafers. For sufficient visibility in the e-beam, the marks needed to be $\geq 1\ \mu$m deep. This required etching completely through the device silicon and buried silicon oxide layers, and into the handle silicon. There were two ways this could be accomplished: a 3 step process, using SF_6 etches for the silicon layers, and a CHF_3 reactive ion plasma etch for the silicon oxide layer; or a 1 step process using a CF_4 reactive ion plasma etch etch for all layers.

The 3 step process was unsuitable because the isotropic SF_6 etch caused the marks to be sloped - this in turn unacceptably decreased the alignment accuracy of the e-beam, which requires a vertical mark edge.

The 1 step process had a sufficiently vertical etch profile, however, the CF_4 etch had very poor selectivity to the PMMA e-beam resist used, and sufficiently deep trenches could not be etched with reasonable ($< 2\ \mu$m thick) resist layers.

Initially, the alignment marks were written and deposited at the same time, and thus were of the same thickness and material as the magnets. For 200

nm thick magnets, the alignment marks were sufficiently resolved by the e-beam. However, as the magnet thickness decreased the signal from the marks decreased as well, to below the e-beam detection threshold.

Platinum and tungsten marks, written and deposited in a separate process before the magnets, were then tried. These metals were selected because they are very dense, resistant to chemical modification, and (unlike gold) broadly compatible with the tools in the CNF. Both marks gave suitable performance in both optical and e-beam alignment tests. Tungsten was more difficult to use than platinum, as it had to be sputtered as a blanket film over the wafer, then etched to define the alignment marks. Platinum could be used in a lift-off process, and so was selected.

100 nm thick platinum marks, with a 5 nm chrome adhesion layer, are currently used for the e-beam and optical stepper alignment processes[4]. The strong signal from these marks in the e-beam allowed for a significant decrease in the signal averaging that was required to detect marks co-defined with the magnets, and thus the alignment time decreased from $\sim$ 1 minute to $\sim$ 15 seconds per chip. This decrease, in turn, decreased the overall time needed to write both the magnets and the etch pits, as in both steps the alignment process was longer than the writing process. Figure 3.10 shows an SEM image of a e-beam alignment mark, while figure 3.11 shows an SEM image of an optical stepper alignment mark. The shape and size of the alignment marks were dictated by the requirements of the tools used.

[4]The backside alignment marks are written and etched during cantilever body fabrication.

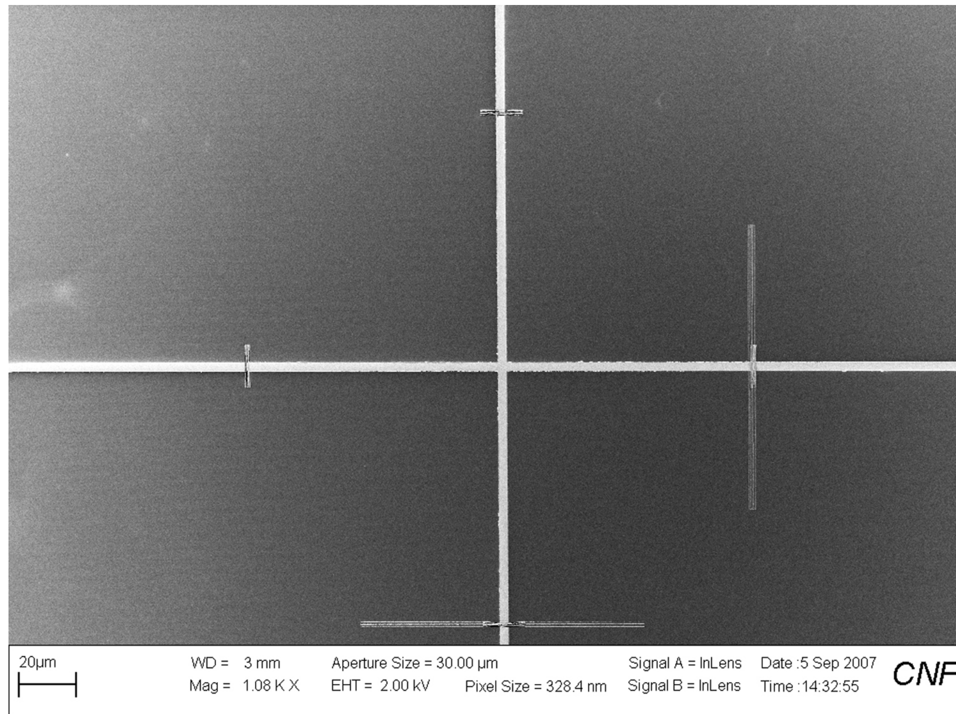

Figure 3.10: SEM of a e-beam alignment mark. This is the "global" alignment mark, of which two are placed at opposite edges of the wafer, and used for the initial, rough alignment. "Local" alignment marks in each die are then read to do the final alignment of wafer features. The shorter lines intersecting the large cross show the areas in which the e-beam exposed the wafer while reading the alignment mark.

3.3.1 Marks for the Silicon Oxide Pillar Process

Platinum marks could not be used for the silicon oxide pillar process, however, as the high temperature silicon oxide growth caused platinum silicide to form. Conversion of platinum to platinum silicide significantly changed the shape of the platinum marks, rendering them unusable. Etched marks were selected because, protected by the silicon nitride layer, they would not be affected by the furnace processing. To etch the necessary depth into the wafer while still us-

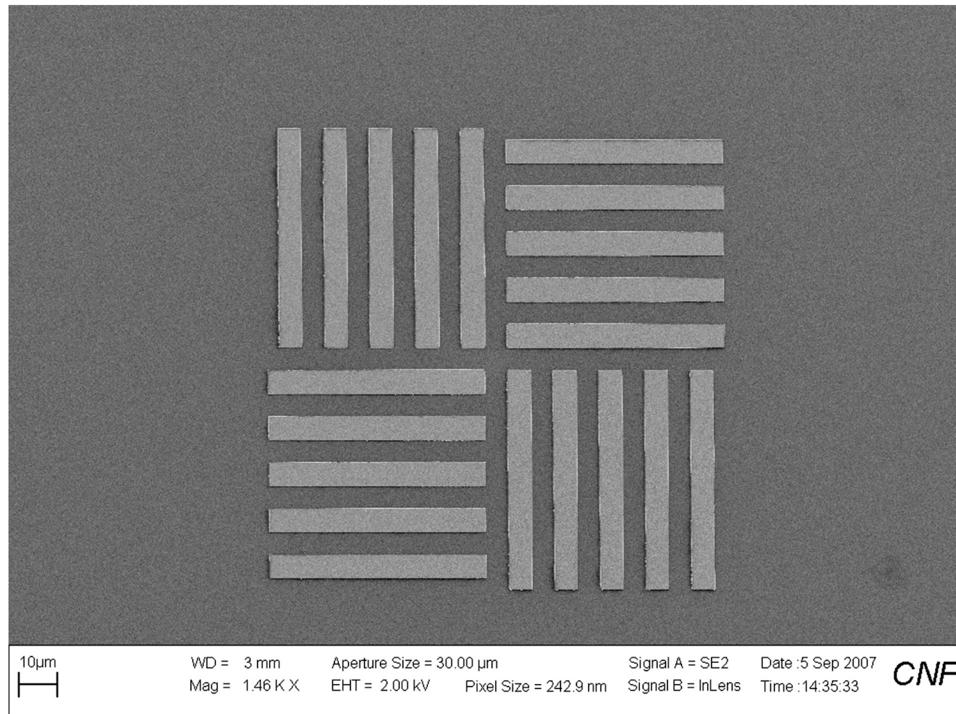

Figure 3.11: SEM image of an optical stepper alignment mark. This is the "local" alignment mark, placed in each die on the wafer, and used to align the stepper system to each die.

ing e-beam lithography to define the marks, an aluminum hard mask was used. Prior to e-beam lithography, a 300 nm blanket layer of aluminum was deposited on the wafer by e-gun evaporation. The mark pattern, written in PMMA resist, was transferred into the aluminum layer using a chlorine based plasma etch. The marks were then etched ~ 1 μm into the SOI wafer, using a CF_4 reactive ion plasma etch. The aluminum hard mask was removed in a wet chemistry etch using a commercial solution of phosphoric, acetic and nitric acid[5].

[5]Transcene Aluminum Etchant Type A

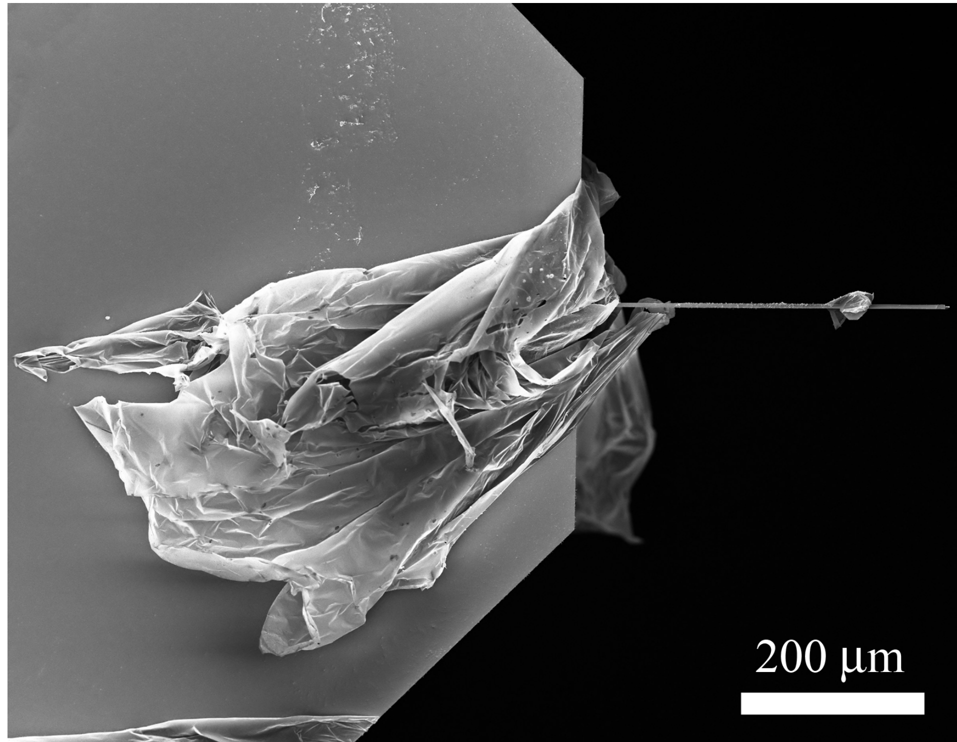

Figure 3.12: SEM of photoresist contamination after critical point drying. This resulted from failure to remove the through-wafer etch photoresist mask before the release etch.

3.4 Backside Silicon Oxide

The use of a backside silicon oxide mask was necessary to prevent disastrous cantilever contamination from through-wafer-etch photoresist during the release process. During the release process, any remaining photoresist tends to detach from the back of the wafer, and often re-deposits on the cantilevers (Figure 3.12). The use of the backside silicon oxide mask allows the photoresist to be removed in a solvent bath midway through the through-wafer etch, while there is still sufficient handle silicon remaining to give the wafer mechanical stability.

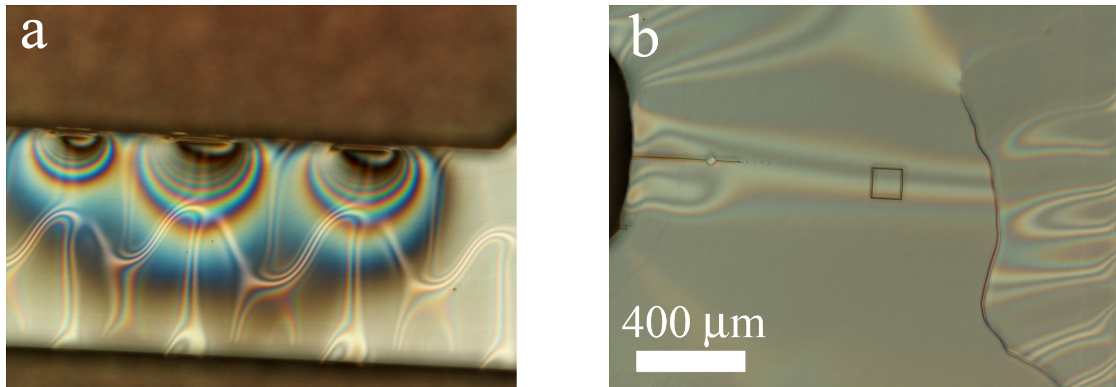

Figure 3.13: Optical micrographs of the silicon oxide membrane between two dies (a) and adjacent to a cantilever (b). Taken in differential interference contrast imaging mode, they show the distortion in the membrane caused by the compressive stress of the silicon oxide layers. In (b) a crack is clearly visible. The scale is the same for both images.

3.5 Release Process Issues

3.5.1 Silicon Oxide Membrane Cracking

At the completion of the through-wafer etch, the flop holes are covered with a thin silicon oxide membrane composed of the thermally grown buried silicon oxide layer and the PECVD deposited top silicon oxide layer. Both of these layers are in compressive stress, which causes the membrane to wrinkle when the handle silicon is removed (Figure 3.13). The stress and thinness of these films makes the silicon oxide membrane very susceptible to cracking and tearing. If the cracks intersect with a cantilever the cantilever is also cracked.

If the crack enlarges to a hole in the membrane, this complicates further through-wafer etching using the Bosch tool. The helium cooling control sys-

tem in the Bosch tool regulates the flow rate by maintaining a setpoint pressure of ~ 3 Torr in the portion of the tool chamber facing the front (non-etching) side of the wafer. Breaks in the silicon oxide membrane allow the He to rapidly escape into the etching portion of the chamber (which is at 24 mTorr) so that the He pressure cannot be maintained at the setpoint and the etch process automatically terminates. If the system is run without the cooling He flow, the etch process rapidly and deleteriously heats the wafer (see chapter 4).

To allow the through-wafer etch to continue with the He cooling after there are breaks in the silicon oxide membrane, a second silicon wafer is attached to the front of the SOI wafer using thermally conductive paste (Figure 3.14). The second, "handler" wafer is etched so that the majority of the wafer surface is 100-200 μm below the height of the ~ 5 mm wide rim. This inset prevents the silicon oxide membrane from sticking to the handler wafer. The handler wafer is attached when the backside resist mask is removed, when there is ~ 100 μm of handle layer silicon remaining in the flop holes. The handler wafer may also prevent silicon oxide membrane cracking by adding mechanical stability to the SOI wafer. The handler wafer is removed by carefully prying the wafers apart, and removing the paste with acetone-soaked swabs. This is done shortly before the SOI wafer is placed in the BOE solution. Chapter 4 covers how the handler wafer was originally added to minimize heating of the SOI wafer during the through-wafer etch.

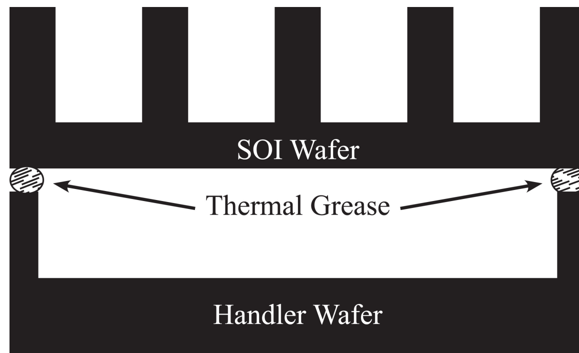

Figure 3.14: Illustration of the handler wafer as it is attached to the SOI wafer. The thicknesses of both wafers has been exaggerated, as well as the thickness of the thermally conductive paste.

3.5.2 Through-wafer Etch Non-uniformity and Resulting Silicon Overetch

In all of the plasma etch processes described in this work, there is a radial non-uniformity in the etch rate, such that material at the rim of the wafer etches ~ 10 % faster than material at the center. In the through-wafer etch, this means that ~ 40 μm of handle silicon remains under the cantilevers in the center chip when the buried silicon oxide layer is reached in chips closest to the wafer rim. In removing all of the handle silicon at the center of the wafer, the chips near the rim are significantly overetched. This causes three complications: thinning of the buried silicon oxide layer, cracking of the silicon oxide membrane, and lateral etching of the handle silicon.

The Bosch etch process, as implemented in this work, has a selectivity of ~ 200:1 silicon : thermally grown silicon oxide. Thus, about 200 nm of the buried silicon oxide is removed in chips near the rim of the wafer during the removal of the final ~ 40 μm of handle silicon from chips at the wafer center. This trans-

fers the radial non-uniformity into the buried silicon oxide layer thickness. In the BOE release etch, this radial non-uniformity causes the silicon oxide under cantilevers near the rim to be removed well before the cantilevers in the center, increasing the exposure of the magnets near the rim to the BOE which, as will be shown in section 3.5.3, can cause damage to the magnet metal.

Longer exposure of the buried silicon oxide layer to the Bosch etch also increases the amount of silicon oxide cracking. It is not known why this is the case, as the resulting thinning of the buried silicon oxide layer should decrease the amount of stress, and the estimated loss of 200 nm of silicon oxide is only 10% of the total membrane thickness. However, this is the observed result, and often the decision on when to stop the through-wafer etch is a compromise between increasing cantilever yield by completing the etch for cantilever near the center of the wafer, and decreasing cantilever yield from membrane cracks.

Over-etching in the through-wafer etch can result in a lateral etching of the handle silicon. This leaves the edges of the device silicon die unsupported by handle silicon. Vibration of the unsupported silicon ledge could dissipate energy from the cantilever, lowering the quality factor. Figure 3.15 shows optical micrographs of three cantilevers, in different locations on the same wafer. The device silicon with handle silicon underneath is a darker shade than the unsupported device silicon. Figure 3.15(a) shows insufficient etching leaving some handle silicon (appearing purple) under the cantilever, Figure 3.15(b) a nearly perfect amount of etching, with just a slight amount of unsupported device layer silicon, and Figure 3.15(c) a large degree of underetching, leaving a ledge of unsupported device silicon several tens of μm wide.

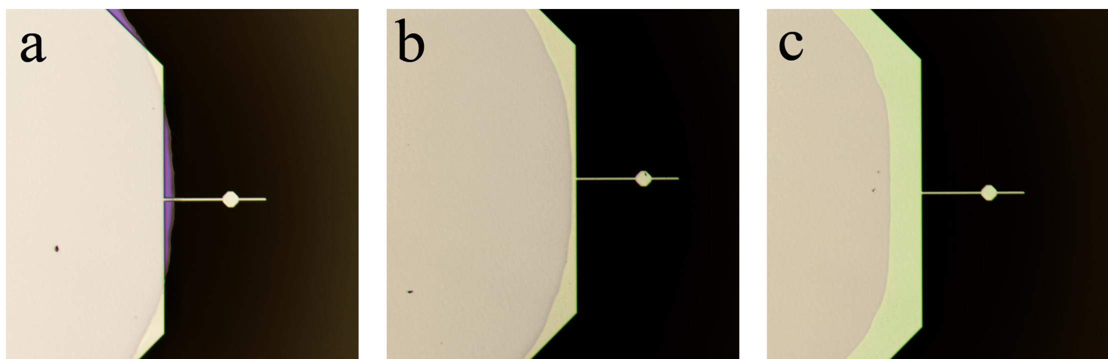

Figure 3.15: Optical micrographs illustrating varying degrees of handle silicon under and over etching. All cantilevers are from the same wafer, and are 200 μm long. The cantilever in (a) was closest to the center of the wafer, and the cantilever in (c) the closest to the wafer rim.

3.5.3 Magnet Damage From Hydrofluoric Acid Etch

Both nickel and cobalt are etched by the BOE solution used to remove the silicon oxide membranes in the release etch. For the few hundred nm sized magnets used in this work, noticeable damage occurred between 2 and 3 minutes of etching for cobalt, and between 6 and 8 minutes for nickel. This degradation was measured by timed etches combined with SEM imaging (Figure 3.16). For both metals, this etching of the magnet material by the BOE left a fairly narrow process window to ensure complete silicon oxide membrane removal without causing magnet damage. To minimize the time the magnets were exposed to the BOE, the top silicon oxide layer thickness was set so that it would etch in the same time as the full 400 nm of the buried silicon oxide layer. Thermally grown silicon oxide etches at $\sim$ 100 nm per minute, while the top silicon oxide was measured to etch at $\sim$ 400 nm per minute. By balancing the silicon oxide layer thicknesses by their respective etch rates, the magnets would not be exposed to

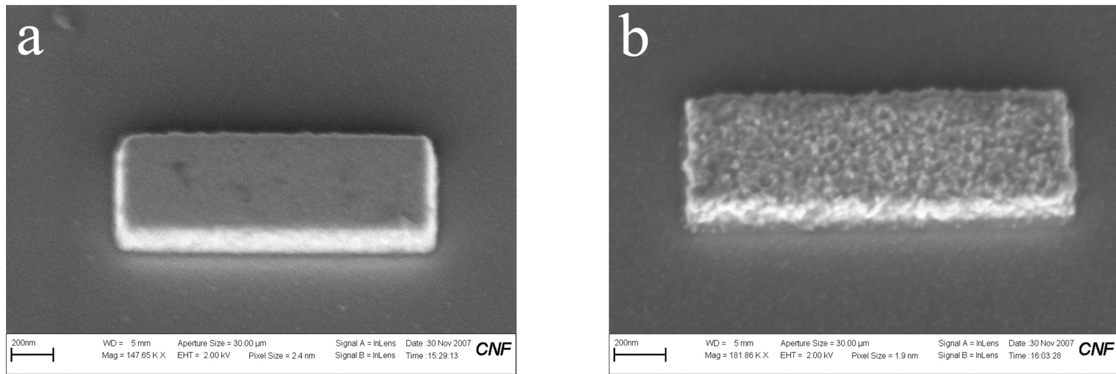

Figure 3.16: SEM images of 600 by 200 nm cobalt magnets, taken after (a) 1 minute and (b) 3 minutes of etching in 6:1 buffered hydrofluoric acid. The samples examined after 1 and 2 minutes were early identical to the un-exposed magnets (not shown) while the 3 minute samples showed obvious degradation.

the BOE until both silicon oxide layers were nearly gone. As mentioned earlier, this balancing was complicated somewhat by the radial non-uniformity in the buried silicon oxide layer caused, ultimately, by the non-uniformity of the Bosch etch.

3.5.4 Precipitation of HF etch products

During a few of the wafer release processes, an oily film was observed to form on the wafer in the first isopropanol bath. After critical point drying, these wafers were covered by a large amount of tiny debris (3.17). It is suspected that this contamination was the precipitated etch product of the BOE silicon oxide etch. The product of the reaction between SiO_2 and F is the gas SiF_4. This can react with the buffering agent $(NH_4)F$ to form the water soluble $(NH_4)_2SiF_6$. If there are insufficient water baths after the BOE etch to dilute this reaction

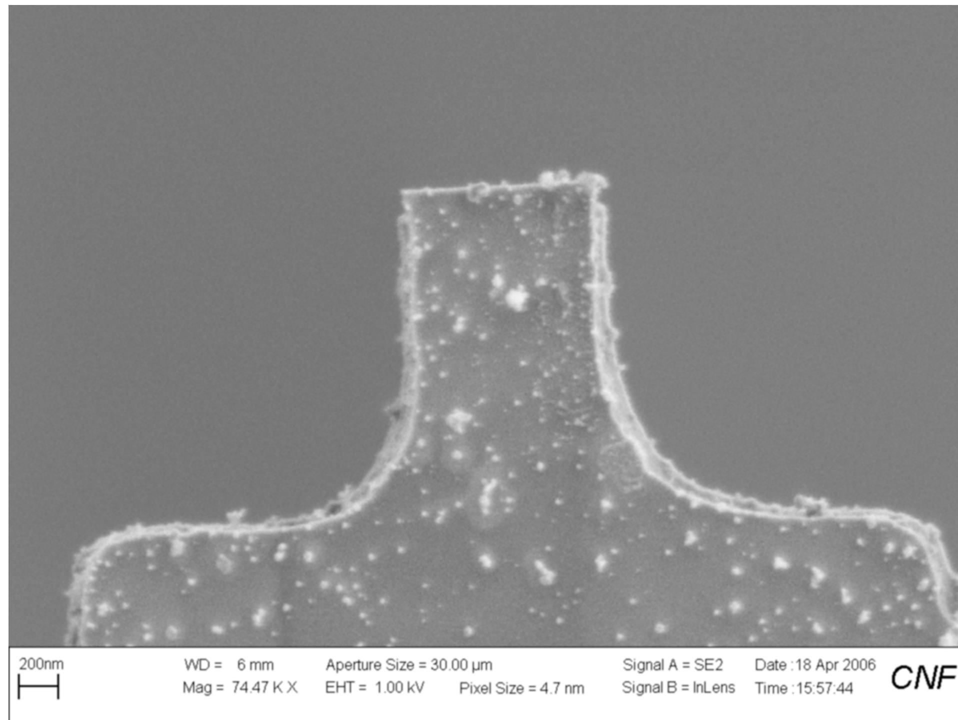

Figure 3.17: SEM image of a cantilever tip coated with debris, after completion of the fabrication process. It is suspected that these debris are $(NH_4)_2SiF_6$ particles from the silicon oxide buffered hydrofluoric etch reaction, precipitated in the isopropanol rinse bath.

product in the water retained between baths in the wafer carrier, the $(NH_4)_2SiF_6$ precipitates on the wafer when placed in the less polar IPA bath. This contamination has been eliminated through the use of 6 H_2O baths after the BOE etch. It is reported [99] that $(NH_4)_2SiF_6$ can be removed by vacuum annealing. If conducted at suitably low temperature to avoid silicide formation, this could allow recovery of contaminated wafers post-release.

CHAPTER 4

SILICIDES

A silicide is a binary silicon-containing compound. Nearly all metals form silicides, and they play a major role in the semiconductor industry, finding use as ohmic contacts, gate electrodes, interconnects, and diffusion barriers. All of the room temperature ferromagnetic metals form silicides. This work focused on the silicide behavior of nickel and cobalt, however, iron [100] and gadolinium [101] have been show to form silicides at similar temperatures to Ni and Co. It is anticipated that the silicide problems experienced with Ni and Co will be experienced with all of the elemental ferromagnets, and that methods of silicide prevention will be broadly applicable.

Nickel and cobalt silicides form at the metal/silicon interface at room temperature, upon deposition of the metal [102, 103]. After a thin layer of the silicide has formed, the layer acts as a diffusion barrier preventing more of the metal ions from reaching the silicon layer, and the reaction rate is thus diffusion limited [104]. As the sample temperature is increased, the metal atoms become more mobile and penetrate the silicide layer, forming more silicide. The growing silicide film, in turn, increases the diffusion barrier. The process is similar to the thermal oxidation of silicon. For thin metal films, this process continues until all of the metal is reacted, forming a metal-rich silicide.

If there is still un-reacted silicon present, a further temperature increase drives the formation of more silicon rich silicides. In thick metal films, the formation of more silicon-rich silicides begins before the complete reaction of all the metal, as the thermodynamic barrier to the formation of the more silicon-rich silicide species becomes smaller than the growing barrier to diffusion. Be-

cause the process is diffusion limited, defining a temperature for the start of silicide formation is difficult, and the literature has widely reported values. Based on differential scanning calorimetry studies of multilayer metal / polycrystalline silicon samples, in this research it is assumed that silicide formation starts at an appreciable rate for nickel at ~450K, and cobalt at ~550K [105, 106].

In the fabrication process of chapter 3, only in the deposition of the protective silicon oxide layers is the sample heated to a known temperature above 465 K. However, it appears that it is during the backside silicon etch in the Bosch etch tool that the silicide formation occurs. This was an extremely unexpected result, because there is no deliberate heating in this etch. Significant research effort trying to discover the mechanism for magnet damage in the cantilever fabrication process was unsuccessfully expended before this discovery. The heating is most likely caused by the exothermic reaction between silicon and fluorine ions, which has an enthalpy of 602 kJ/mol. As an illustration of the heating this reaction can cause, assume a 10 by 10 μm area of the handle silicon, 20 μm tall, sitting on the buried silicon oxide layer. Etching of the first 10 μm of this block generates $\sim$ 5 kJ. If all this energy is transferred to the remaining silicon in the block (neglecting energy loss to the SiF_4 etch products, surrounding silicon, and the silicon oxide layer), the temperature increase will be $\sim 3 \times 10^4$ K. Clearly the silicon etch reaction with fluorine is a potential cause of material heating.

In the final portion of the through-wafer silicon etch, the magnet is surrounded by the topside protective silicon oxide and the buried silicon oxide layer, with only the thin cantilever body and any remaining backside silicon providing a thermal conduit for heat to flow to other portions of the wafer. The Bosch etch tool does have a cooling flow of room temperature helium, at a rate

of a few SCCM, but even when it is applied directly to the magnets, in a sample with no protective front silicon oxide, the gas flow is not sufficient to prevent silicide formation. The importance of the thermal contact provided by the backside silicon is demonstrated in Figure 4.1. This series of SEM images are taken of the same wafer, showing cobalt magnets after the completion of the fabrication process. This wafer was processed before the formation of silicides was identified, and no steps were taken to prevent heating during the through-wafer etch. Cobalt silicide is soluble in HF [107]. Thus, the disappearance of the cobalt magnets after the release process is attributed to the formation of silicides. In this wafer, the etch was stopped after only the cantilevers nearest the rim of the wafer were completely free of handle-wafer silicon (Fig. 4.1(f)). The dies closer to the center of the wafer had an increasing amount of silicon remaining under the cantilever (Fig. 4.1(d)). The die in the center of the wafer had backside silicon remaining under the entire region of the flophole (Fig. 4.1(b)). The degree of damage to the magnets increased the further away from the center of the wafer - the only change being the amount of backside silicon remaining. This leads to the conclusion that the backside silicon must provide sufficient thermal contact or, alternately, insulation to prevent the formation of silicides.

4.1 Evidence for Silicides

Unfortunately, all of the evidence for silicide formation is indirect. Because of the fragility of the unreleased, through-etched wafers it would be nearly impossible to prepare samples of the suspected silicides for transmission electron microscopy analysis, and the size of the magnets is too small for elemental analysis techniques such as X-ray photoelectron spectroscopy, energy dispersive X-ray

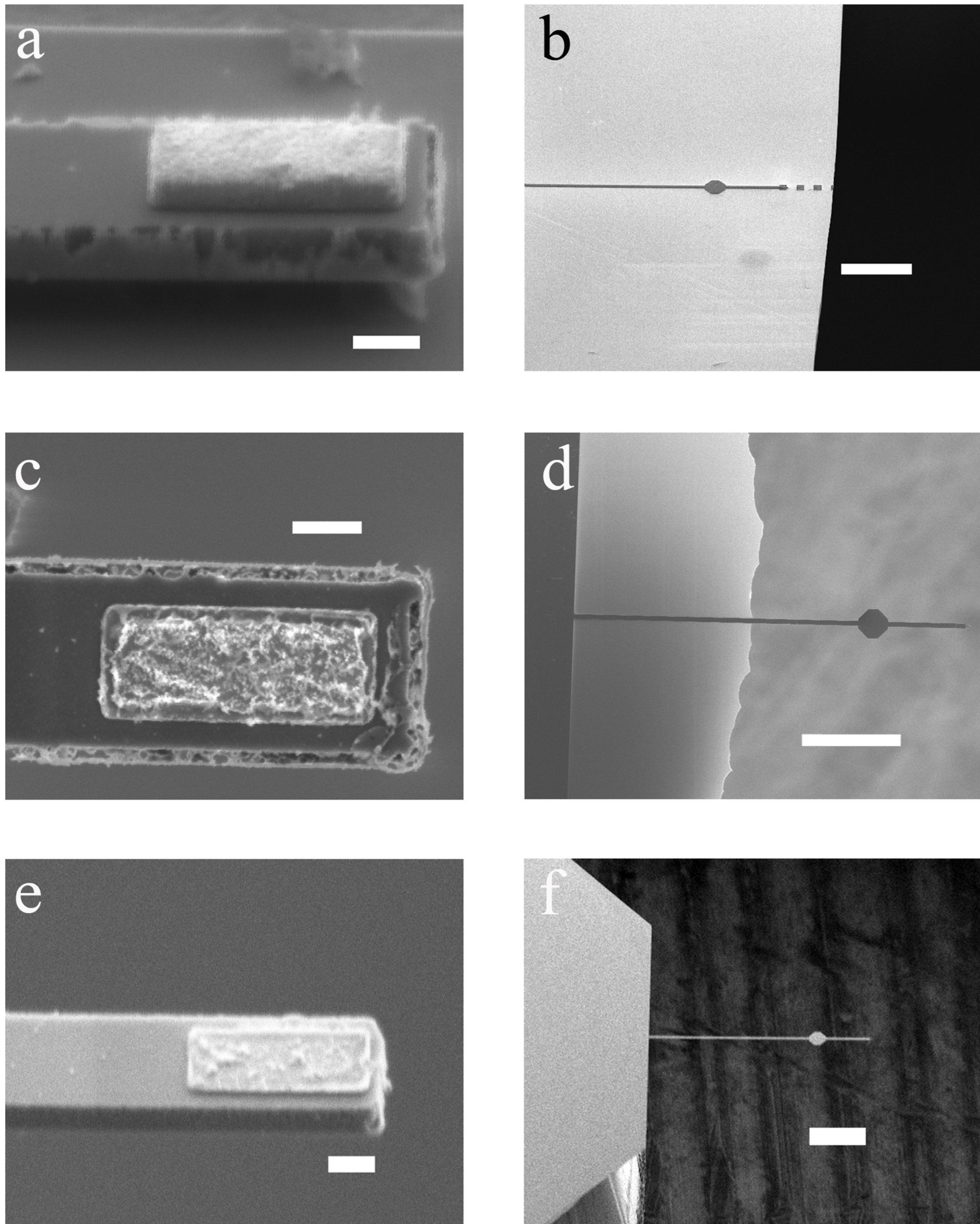

Figure 4.1: SEM images of wafer with incomplete through-wafer silicon etch. Images on the left are close-up images of the tip magnets of the cantilevers on the right. The scale bar is 400 nm long in the images on the left, and 100 μm long in the images on the right.

spectroscopy, and Auger electron spectroscopy. As noted previously, Ni and Co silicide are destroyed in the buffered hydrofluoric acid etch during the release process.

The conclusion that silicide formation is the cause of loss of tip magnet material is drawn from the careful SEM observation of numerous wafers up to the protective silicon oxide deposition step (after which the magnets cannot be seen until post release processing), combined with numerous control experiments that ruled out magnet damage from the hydrofluoric etch, the critical point drying, or the protective silicon oxide layer. The backside silicon oxide etch is not suspected as the cause, as the loss of magnet material was observed before the backside silicon oxide layer was added to the fabrication procedure. This leaves the backside silicon etch as the only step in which the damage to the magnetic material could occur.

The most definitive proof of both silicide formation and the Bosch etch being the cause was a wafer processed without a front silicon oxide layer, thus allowing SEM observation at points during the backside etch. Comparisons of images taken after 360 μm of etching (Figure 4.2) with those at the completion of the backside etch (Figure 4.3) shows a large growth next to each magnet, associated with varying amounts of structural change to each magnet. These large growths were not observed anywhere but next to the magnets. The only materials in contact or nearby the wafer during the etch were the silicon cantilever body, the buried silicon oxide layer, the chrome adhesion layer, the helium cooling gas, and the aluminum lower plate of the etch tool. Given these materials, silicide formation is the most reasonable conclusion. As additional proof, with several of the magnets imaged, the growth appeared to be issuing

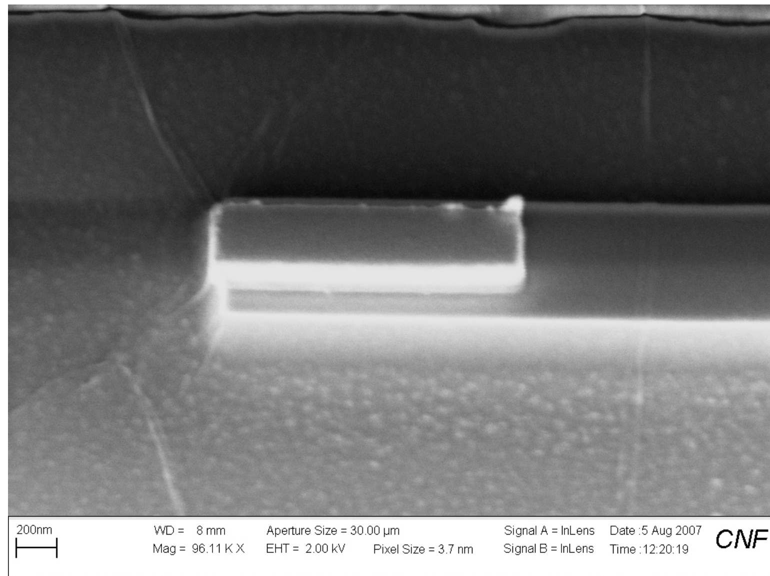

Figure 4.2: SEM images of wafer with no front protective silicon oxide, after 360 μm of silicon has been removed in the through-wafer etch.

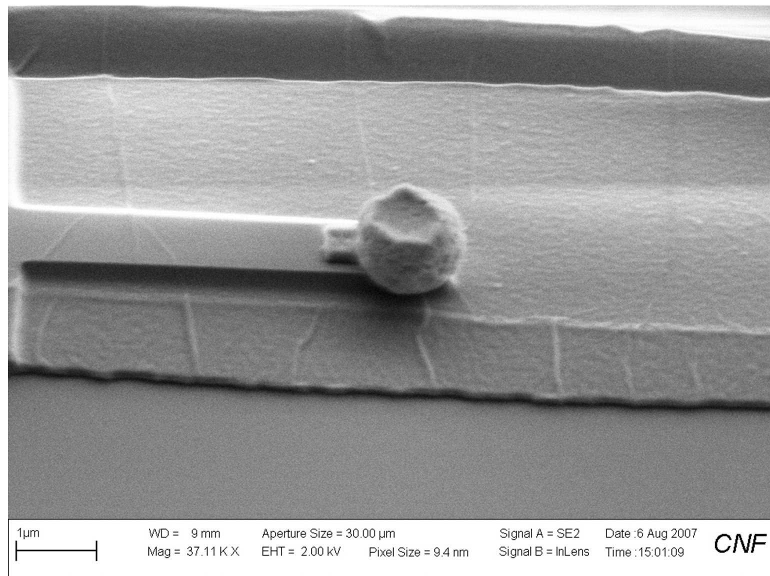

Figure 4.3: SEM images of wafer with no front protective silicon oxide, after completion of through-wafer etch. Cantilever body is sitting on buried silicon oxide layer.

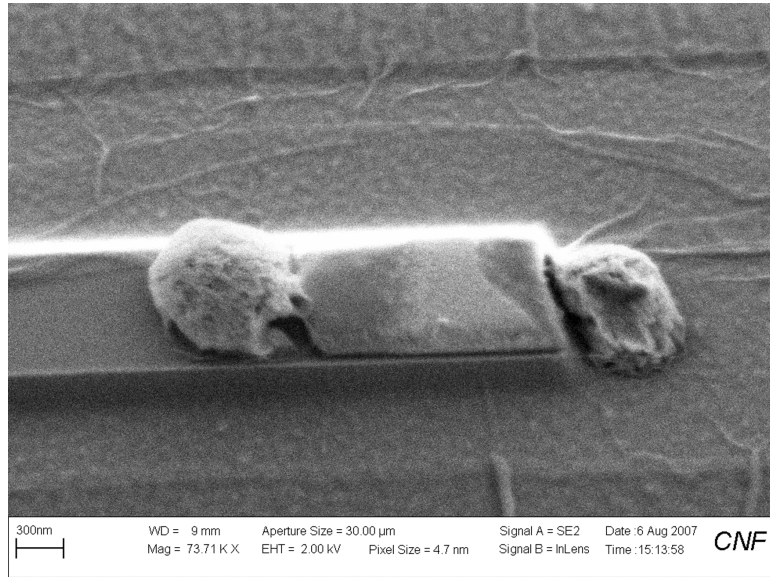

Figure 4.4: SEM images of wafer with no front protective silicon oxide, after completion of through-wafer etch. Silicide appears to be coming from metal/silicon interface.

from the metal/silicon interface, consistent with silicide formation (Figure 4.4).

4.2 Barrier Layer for Silicide Prevention

In the semiconductor industry the method for preventing silicide growth is use of a barrier layer. The barrier layer must be highly impervious to the diffusion of metal atoms, and not react with the metal of interest. To be applicable to the fabrication process for MRFM cantilevers, the barrier material must also be resistant to HF etch. In order to not increase the surface-induced dissipation expected when the cantilever approaches a surface, the barrier layer must be thin, perhaps 20 nm or less. The material must promote sufficient adhesion between the silicon and the magnet. The ideal barrier layer for this process would also be deposited by evaporation, so that it could be applied in the same step,

and using the same lithographic mask, as the magnet. The two materials used most commonly for silicide prevention barriers, SiO_2 and Si_3N_4, are inapplicable as both etch readily in HF, and evaporated films of these materials tend to be porous. Three metals were tested as barrier materials: chromium, titanium, and tantalum. The first was already in use in the fabrication process, as a 5 nm adhesion layer. Titanium was selected as it is another commonly used adhesion material. Tantalum was selected because it is extremely dense, and is used as a copper diffusion barrier in integrated circuits. The magnet material was cobalt. All materials were deposited with electron-gun evaporation, a 20 nm layer of the barrier metal, followed by a 200 nm layer of cobalt. Because of the material, tool and time costs in performing the full backside etch process on SOI wafers, a simple furnace test was developed to mimic or exceed the thermal conditions found in the Bosch etch tool. For each barrier metal, 4 samples were prepared: one left bare, and the other three coated with a ~250 nm PECVD silicon oxide layer after the metal deposition. The bare sample and 2 of the silicon oxide-coated samples were loaded into a 500 °C N_2 furnace. The furnace run length was 5 minutes, with an additional $\sim$ 3 minutes in a load or unload step. During the loading and unloading, the temperature of the samples was unknown but likely close to 500 °C (from the thermal mass of the furnace load arm) and the atmosphere that of the cleanroom air. The final sample was not heated, but left as a control for any changes caused by the PECVD silicon oxide deposition. After heating, the silicon oxide was removed from the control sample, as well as one of the silicon oxide-coated, heated samples, in a 2.5 minute buffered HF etch. The damage seen in the bare samples (Figures 4.5, 4.6, and 4.7) is now believed not to be caused by silicide formation but rather oxidation of the magnet that occurred during the load process. Comparison of the morphology

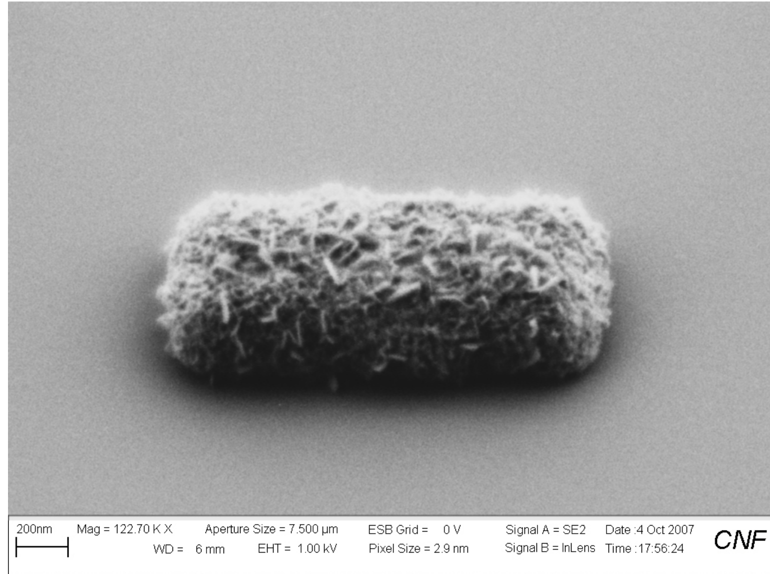

Figure 4.5: Ta barrier layer test structure, annealed with no protective silicon oxide.

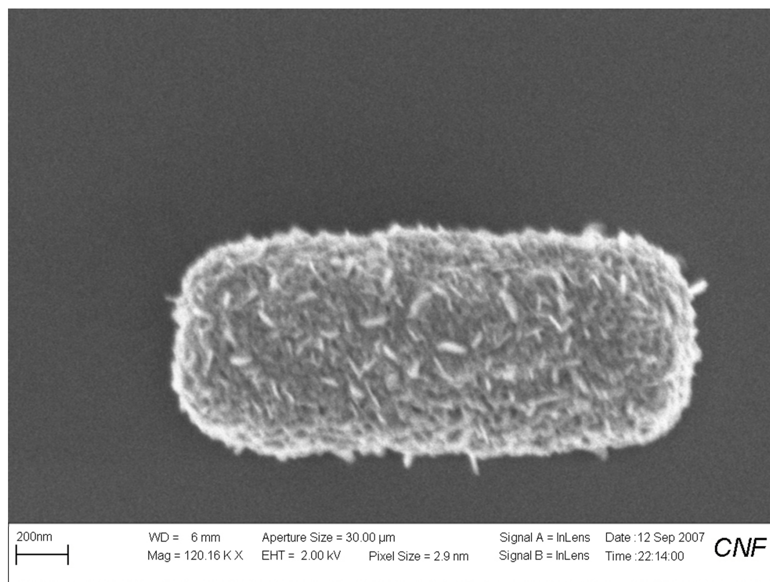

Figure 4.6: Ti barrier layer test structure, annealed with no protective silicon oxide.

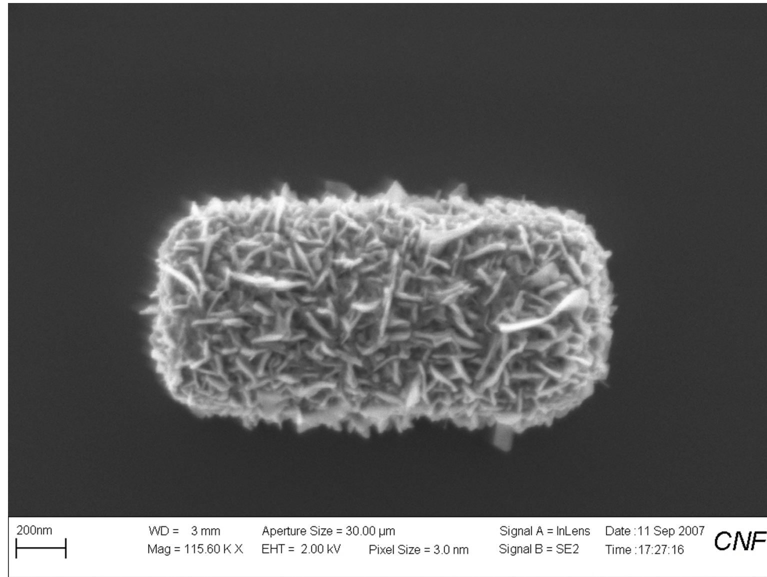

Figure 4.7: Cr barrier layer test structure, annealed with no protective silicon oxide.

of the tantalum barrier layer sample annealed under silicon oxide (Figure 4.8), to the sample coated with silicon oxide but not annealed (Figure 4.9), suggests that the changes in morphology may be related to the BOE etch, as the time for noticeable damage to cobalt magnets in this etch is between 2 and 3 minutes.

This testing was conducted when the silicide formation temperature of cobalt was believed to be approximately 500 °C. With the currently accepted value of ~ 250 °C, and the suspicion that the damage seen was related to cobalt oxide formation, it may be worth revisiting these tests, using a rapid thermal annealing device to precisely control both the length of heating time, and to mitigate cobalt oxide formation.

Finally, films of aluminum oxide produced by atomic layer deposition (ALD) are also an interesting possible barrier layer material. Although the ALD process results in a conformal film, it has been reported [108] that when deposited

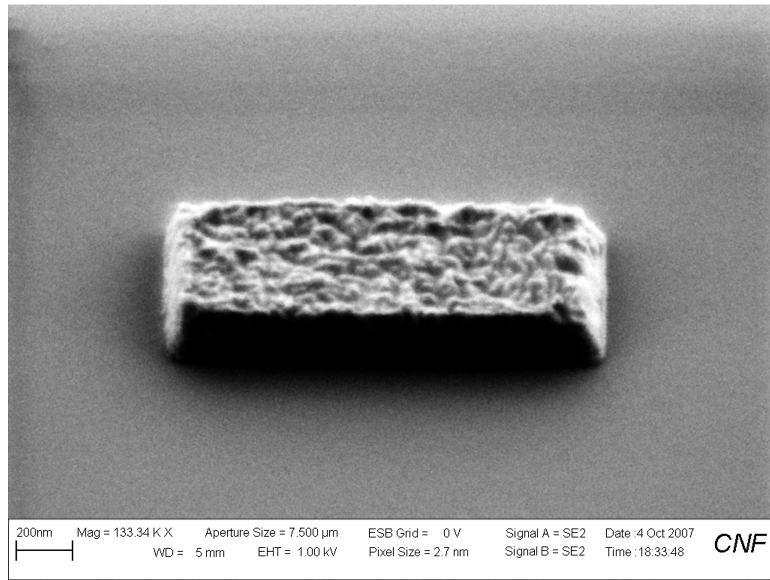

Figure 4.8: SEM images of 200 nm thick cobalt magnet atop a 20 nm tantalum barrier layer. The sample was covered with PECVD silicon oxide and annealed at 500 °C.

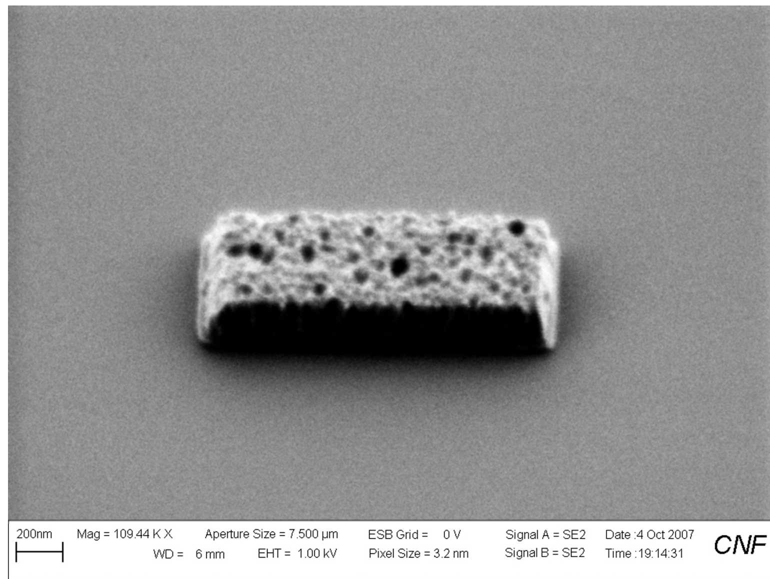

Figure 4.9: SEM images of 200 nm thick cobalt magnet atop a 20 nm tantalum barrier layer. The sample was covered with PECVD silicon oxide but not annealed.

over a patterned resist layer, thin films of Al_2O_3 shatter when the resist is removed, allowing it to be deposited in a lift-off type process. Al_2O_3 is an extremely dense film, resistant to chemical etch, and unreactive to metals. ALD deposition allows defect free films of only a few nanometers thickness to be reliably deposited.

4.3 Alternative to the Bosch Etch

In the work by Stowe [109] the backside silicon was removed in a tetramethylammonium hydroxide (TMAH) etch. TMAH, like KOH, anisotropically etches silicon. With proper design of the backside mask to account for the non-vertical etch, this method, which can be done in a few hours at 50-60 °C, would presumably not have the concerns of heat build-up.

KOH etching was tested as a method for performing the last $\sim$ 100 μm of through-wafer etch. The initial 400 μm of etching was performed in the Bosch tool. The KOH etch was performed at 90 °C, where silicon etch rates are $\sim$ 1.3 μm/minute. These tests encountered several difficulties. Bubbles from the etch and the viscosity of the KOH solution were believed to have caused significant breakage of the silicon oxide membrane. This breakage was a problem even through a surfactant was added. The selectivity of KOH to the silicon oxide was quite a bit worse than in the Bosch process. For the front silicon oxide layer, this could be surmounted by thickening the layer. The problem with the buried silicon oxide layer was the low (50:1) selectivity to silicon, combined with the radial non-uniformity of the Bosch etch. This meant that the buried silicon oxide at the outer edge would be completely removed by the KOH before the silicon

for the innermost dies was removed. This, however, would not be a problem if KOH was used to etch through the entire wafer. Because of the selectivity issue and silicon oxide membrane cracking, KOH etching was unsuitable for the through-wafer silicon etch.

4.4 Heat Management in the Bosch Etch

4.4.1 Heat Sink Wafer

Controlling the heat generated in the Bosch process is difficult as there is no direct temperature measurement of the wafer or wafer holder. Further, the average temperature of the wafer likely does not reflect the local temperature of the magnets, especially during the crucial final portion of the backside silicon etch. The addition of a second wafer as a heat sink was tried as a simple solution to wafer heating. The wafer was attached to the front of the SOI wafer using thermally conductive paste. Because of the fragility of the silicon oxide membranes at the completion of the etch process, this second, ”handler” wafer could only be in direct contact with the SOI wafer along the rim. This likely significantly reduced any thermal flow between the two wafers, and perhaps not unexpectedly, its inclusion did not resolve the silicide problem. Indeed, it is possible that the addition of the second wafer worsened the SOI wafer heating, as it blocked the flow of cooling helium. As noted in chapter 3 the handler wafer has nevertheless been kept in the process to allow etching to continue after cracks develop in the silicon oxide membranes over the flop holes.

4.4.2 Aperture Plates

The radial non-uniformity of the Bosch etch complicated application of heat management schemes. As noted earlier, the crucial period for heat management in the Bosch etch was while there was less than ~100 μm of silicon remaining. Because of the etch non-uniformity the outermost dies reached this thickness threshold when the innermost dies had ~140 μm of silicon to be removed. Thus any heat management process had to be applied for 40% more etching than if the Bosch etch rate was uniform across the wafer. As most of the heat management schemes developed significantly decreased the etch selectivity to silicon oxide and resist, and also decreased etch speed, increasing etch uniformity would be beneficial. To improve the radial uniformity of the through-wafer etch, a series of circular aperture plates were produced from silicon nitride-coated silicon wafers. The goal was to create an inverse of the non-uniformity initially, by selectively etching regions of the wafer exposed through the plates. The apertures were 25, 50, and 75 mm in diameter. Testing of various combinations of the plates and etch depths found that three apertures did not provide sufficient gradation to create the needed inverse of the etch non-uniformity, and the improvement was 20% at best. If this approach is tried again, use of a greater number of apertures might improve performance.

4.4.3 Slow Etching

The most successful silicide mitigation scheme prevented heat buildup by decreasing the duration of continuous Bosch etching, and implementing timed periods between etches to allow the tool chamber (in particular the poorly con-

ductive ceramic wafer clamp) to cool. As there is no way to monitor the temperature of this clamp, the length of the cooling periods was a best-guess, and this led to variability and difficulty in reproducing the fabrication process. Repeatedly restarting the Bosch etch decreases the selectivity to silicon oxide. This is because C_4F_8, the source of the protective fluoropolymer that gives the Bosch process its anisotropy, is an aggressive silicon oxide etchant if there is an applied bias between the sample and the plasma. Such a bias is necessary in lighting the plasma. As mentioned in section 4.3 a high selectivity to silicon oxide is needed to completely remove the silicon in the center of the wafer without destroying the cantilevers nearest the wafer rim. A suitable balance between silicon oxide selectivity and heat buildup was found with etch periods of 20 to 30 loops (with etch period time 260 to 390 seconds), removing approximately 4 to 6 μm of silicon per period. The cooling period of 10 minutes was also a trade-off between desire to allow the chamber to full cool, and the time availability of both the equipment and researcher. [1] This procedure is highly dependent on the specific Bosch tool used - moving the process to a different tool will require care and detailed inspection of the tool's wafer handling and cooling mechanisms, as well as its etch rate (as a proxy for the thermal load).

4.4.4 Cryogenic Etch

The ideal tool to accomplish a low temperature backside silicon etch is a cryogenic silicon etcher. This type of tool, while having a slower etch rate, lower directional anisotropy, and worse selectivity to silicon oxide and photoresist than

[1] Experience gained from opening the etch chamber of the Bosch etch tool to check the clamp temperature after etching suggests that a wait time of 30 minutes would allow the wafer clamp to cool to room temperature.

Bosch process tools, has the excellent property of keeping the wafer at cyrogenic temperatures throughout the etch process [110]. Thus there should be no silicide formation. Another potential advantage over the Bosch etch is that there is no remaining sidewall material after completion of etching, in comparison with the extremely difficult to remove fluoropolymer that remains on the sidewalls after a Bosch etch. If such a tool is available, its use is highly recommended.

CHAPTER 5

CANTILEVER AND MAGNET ANALYSIS

5.1 Probe

A custom-built probe [1] operating at 4.2 K and high vacuum (P $\leq 10^{-6}$ mbar) was used for cantilever spring constant, frequency, and quality factor measurements. The same probe was used to conduct cantilever magnetometry measurements of the magnetic moment and coercivity of the tip magnets, surface-induced dissipation and jitter measurements, and electron spin resonance MRFM experiments [112].

5.2 Frequency, Spring Constant and Quality Factor Measurement

Cantilever motion was monitored via a fiber optic Fabry-Pérot interferometer, operating at 1310 nm [113]. The laser was temperature tuned so that the cantilever motion was centered on a fringe [114]; in normal operation cantilever motion did not exceed the distance of one fringe. The spring constant was determined by measuring the thermally driven motion of the cantilever, x_{th}, and using the relationship $k = k_B T / x_{\mathrm{th}}^2$. The interferometer is aimed at the hexagonal reflector pad, which is located 75 μm from the cantilever tip. To account for the difference in amplitude of motion at the pad versus the tip, the measured x_{th} was multiplied by a factor α_{PT} derived using the modeshape for the first can-

[1] See appendix C of Ref [111] for a complete description of the probe design.

tilever mode. $\alpha_{\mathrm{PT}} = 2.02$ for 200 μm long cantilevers, and $\alpha_{\mathrm{PT}} = 1.35$ for 395 μm long cantilevers. Any non-thermal driving of the cantilever, such as mechanical vibrations, will result in a lower value for the spring constant when measured in this way. Because the thermal driving is very small at 4.2K, the uncertainty in the spring constant is fairly large.

Cantilever resonance frequency was measured by driving the cantilever into self-oscillation [115] using a piezoactuator at the cantilever base, controlled by a custom-built analog controller implemented in a fixed-gain positive feedback loop. The digitized output of the interferometer was processed with a software frequency demodulator [21], giving the instantaneous cantilever frequency.

The quality factor was determined by measuring the cantilever ring-down time. The cantilever was driven into self-oscillation, the driving circuit turned off, and the cantilever signal recorded. A plot of cantilever amplitude versus time was created, and fit to $A(t) = A_0 e^{-\frac{t}{\tau}} + A_\infty$ where A_∞ is the thermally driven cantilever amplitude. Q was calculated from $Q = \pi f_c \tau$, with f_c the cantilever frequency. The time τ is often referred to as the 1/e time, as in a time τ the cantilever amplitude will decay to 1/e of its original magnitude.

5.3 Cantilever Magnetometry

The magnetic moment of the tip magnet was determined by frequency-shift cantilever magnetometry [37, 87, 116, 117]. In this technique a homogeneous magnetic field is applied along the long axis of the cantilever, while the cantilever is driven in self-oscillation (Figure 5.1). The applied field exerts a torque on the tip magnet as the bending of the oscillating cantilever creates an angle between the

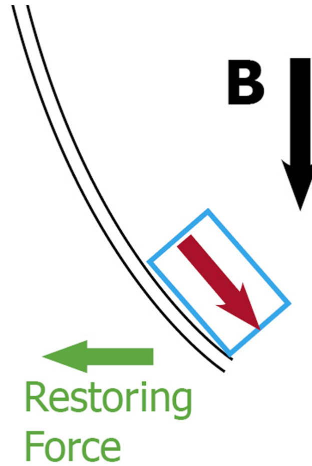

Figure 5.1: Illustration of geometry for cantilever magnetometry measurements.

field of the tip magnet and the applied field. This torque acts as a restoring force on the cantilever. The cantilever frequency is recorded as a function of applied field. Modeling the tip magnet as a single-domain particle with uniaxial shape anisotropy, the frequency shift versus field data was fit to:

$$\frac{\Delta f}{f_0} = \frac{\mu}{2k}\left(\frac{\alpha}{l}\right)^2 \frac{B\Delta B}{B + \Delta B}. \tag{5.1}$$

with μ the saturated magnetic dipole moment, μ_0 the permeability of free space, k the cantilever spring constant, l the cantilever length, $\alpha = 1.377$ a constant related to the modal shape of cantilever vibration, $B = \mu_0 H$ the applied magnetic field, and $\Delta B = \mu_0 \mu \Delta N / V$ with V the magnet volume and $\Delta N = N_t - N_l$ the difference in the demagnetization factors for the nanomagnet along the cantilever's thickness and length, respectively. To compute magnetic volume, the magnet area was estimated from scanning electron microscope images and the magnet thickness was taken from a quartz crystal microbalance thickness monitor during magnet metal deposition.

Figure 5.2b shows a plot of frequency shift versus applied magnetic field for

one of the magnet-tipped cantilevers analyzed. The red line is the fit to equation 5.1. Figure 5.2(a) is the residuals of the fit, which shows extremely good agreement except near zero applied field. This disagreement near zero field is due to the hysteresis of the tip magnet, which is not accounted for by the model of equation 5.1. Figure 5.2(c), a zoom-in of the data near zero applied field, shows more clearly this hysteresis behavior. The arrows in the figure indicate the direction of the magnetic field sweep for each trace. The hysteresis shown is consistent with single-domain switching at a coercive field $\mu_0 H_c$ = 50 mT. Above the switching field the traces for the two field sweep directions are essentially indistinguishable. The magnetometry data from all cantilevers analyzed is presented in section 5.6.

5.4 Force Gradient Detection of Electron Spin Resonance

A limitation of cantilever magnetometry is that it provides information only about the total magnetic moment of the sample. For MRFM experiments, it is crucial that the leading edge of the magnet, the edge closest to the sample, be well magnetized (i.e. free of non-magnetic material caused by oxidation or silicide formation). Any such "dead layer" effectively increases the magnet-sample distance, decreasing the magnetic field gradient and thus the spin signal. To show that the tip magnet's leading edge is well magnetized, one cantilever was used to mechanically detect electron spin resonance (ESR) from a nitroxide free radical using a force-gradient approach [15, 43] modified to detect fast-relaxing spins [118]. The sample was a 230 nm thick film of 40 mM TEMPAMINE in perdeuterated polystyrene coated with 20 nm of gold. Operating at 4.2 K and 10^{-6} mbar, the cantilever was brought to 80 nm above the sample surface in the

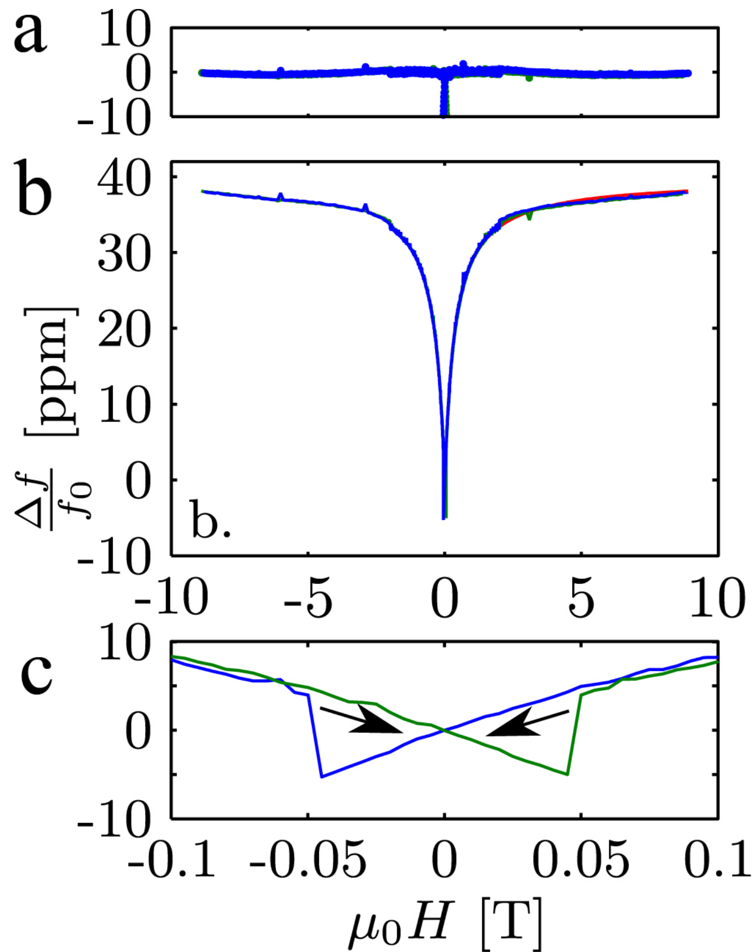

Figure 5.2: Data from cantilever magnetometry analysis of a overhanging nickel nanomagnet. (b) Frequency shift versus applied magnetic field. The blue and green lines are data taken sweeping the field in opposite directions, and the red line is the fit used to calculate the tip magnetic moment. (a) The residuals from the fit. (c) The magnet hysteresis near zero field. The arrows indicate the direction of field sweep for each of the traces.

pendulum geometry and driven to peak-to-peak amplitude of 80 nm. A static magnetic field was applied along the width of the cantilever [15,87] which mitigates damping of the cantilever arising from tip-field interactions [14]. Note that this is somewhat different than the geometry illustrated in Figure 1.5. In this experiment, the static magnetic field was applied in the direction that would be out of the plane of the illustration in Figure 1.5. To saturate sample spins, a cantilever-synchronized train of 17.7 GHz microwave pulses was applied to the sample, modulated at 9.56 Hz. Each pulse lasted for 6 cantilever cycles, followed by 6 cycles without microwave irradiation. The cantilever frequency was recorded using the method described in section 5.2.

5.5 Surface-induced Dissipation and Frequency Noise

Cantilever dissipation and frequency noise (or jitter) were measured as the cantilever was moved towards the same gold-coated polymer sample used for the ESR-MRFM measurements. The total dissipation value at each point was determined by measuring the cantilever ringdown time, and then calculating Γ from that value and the measured cantilever frequency and spring constant. The jitter is determined by recording the instantaneous frequency of the cantilever for time t, and then taking the power spectrum of fluctuations of the frequency from the average frequency over that time period [22].

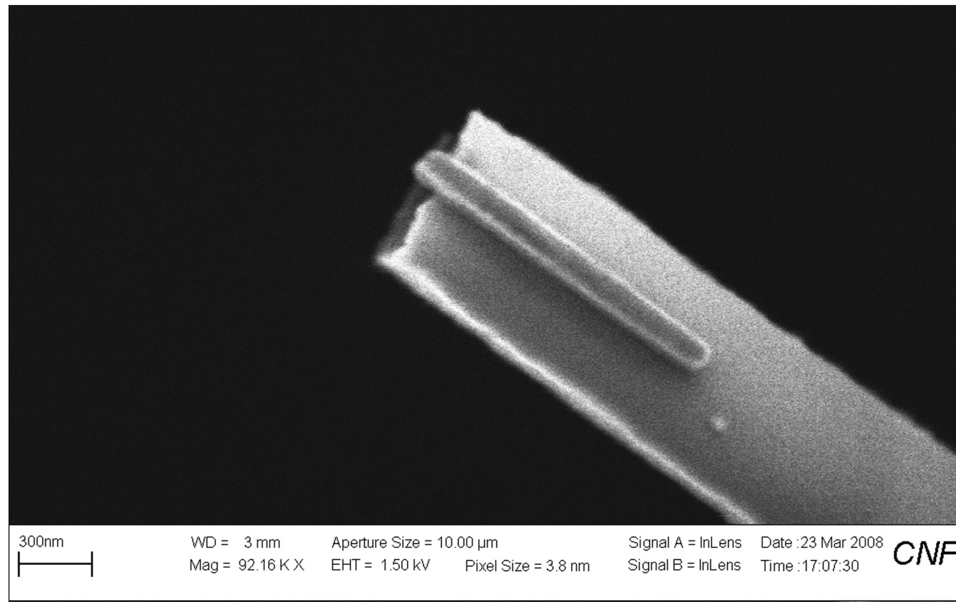

Figure 5.3: Cantilever with a nickel magnet with a ~ 50 nm overhang. This was a result of insufficient SF_6 etching.

5.6 Results of Cantilever Analysis

Following the fabrication process in chapter 3, five wafers were produced that, from SEM analysis, had at least one undamaged magnet at the completion of processing. All were nickel magnets. On two of the wafers, the undercut etch was insufficient, leaving the magnets either negligibly (Figure 5.3) or not overhanging the silicon (Figure 5.4). Initial analysis was performed with a scanning electron microscope. Typically, it was extremely obvious by this "visual" inspection whether the fabrication process was successful, from the significant morphological changes and/or lack of magnets on unsuccessful cantilevers (Figure 5.5). Although SEM analysis does not provide information about the magnetic properties of the magnets, it is much faster than the methods that do, and is a simple check to select candidates for more time-consuming analysis such as cantilever magnetometry.

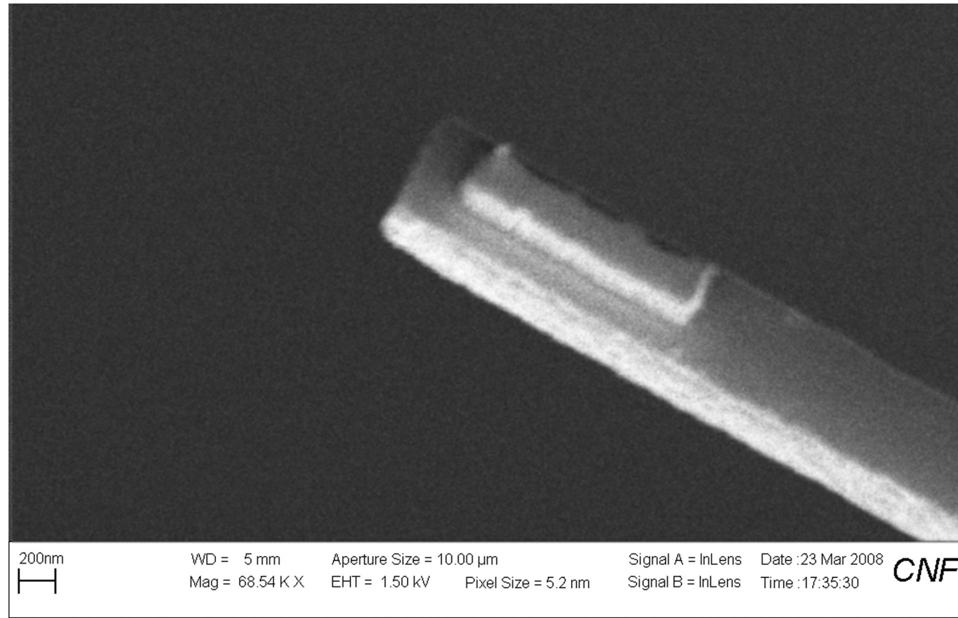

Figure 5.4: Nickel magnet positioned several hundred nm back from the cantilever tip. This was a result of an incorrect position adjustment in the "etch pit" lithography.

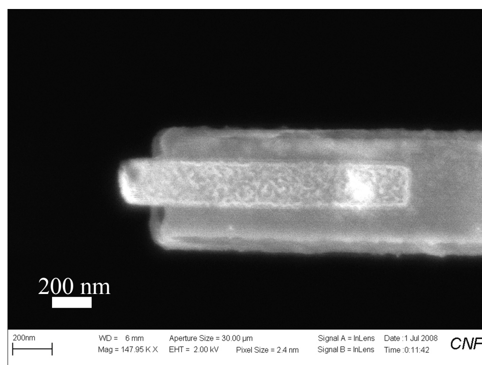

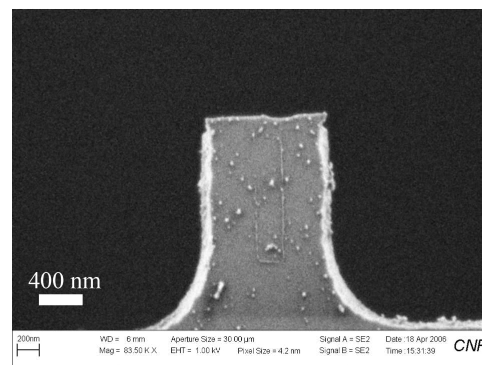

Figure 5.5: SEM analysis showing partially or completely absent tip magnets after cantilever fabrication.

The magnification at which the tip magnets could be imaged, at best 150,000x, was far less than the 250,000x images that could be obtained at the cantilever base. At higher magnifications, the tip would appear to oscillate rapidly from the electron beam (Figure 5.6). Initially this was believed to be caused by the electron beam driving the cantilever on resonance when focused closely on the end of the cantilever. However, the time in which the oscillations disappeared when the magnification was decreased did not correlate with the long ringdown times measured for these cantilevers. A second hypothesis was formed, that the charge deposited on the end of the cantilever was causing deflection of the electron beam, rather than the cantilever. This theory, however, does not explain why the problem increased at higher beam voltages, which should make the electron beam harder to deflect. As a practical concern, the cantilever "driving" was decreased by decreasing the beam voltage, scanning at a $\sim$ 45 degree angle to the long axis of the cantilever, and using a frame-averaging imaging mode rather than pixel averaging. Supporting the cantilever with a grounded knife-edge near the tip should also decrease the driving, but would increase the chance of breaking the cantilever.

From SEM analysis, magnets of dimensions from 70 nm by 100 nm to 600 nm by 200 nm were fabricated on cantilevers both 200 and 395 μm long. Measured magnet overhang lengths were from $<$ 50 nm to ~400 nm. It is possible that magnets were also successfully produced on cantilevers of 1 and 1.5 mm length, however, it proved impossible to image the cantilever tips with the required resolution. This speculation is based on the presence of magnets on shorter, 395 μm long cantilevers on the same wafer.

From the cantilevers with tip magnets identified from SEM analysis, 3 were

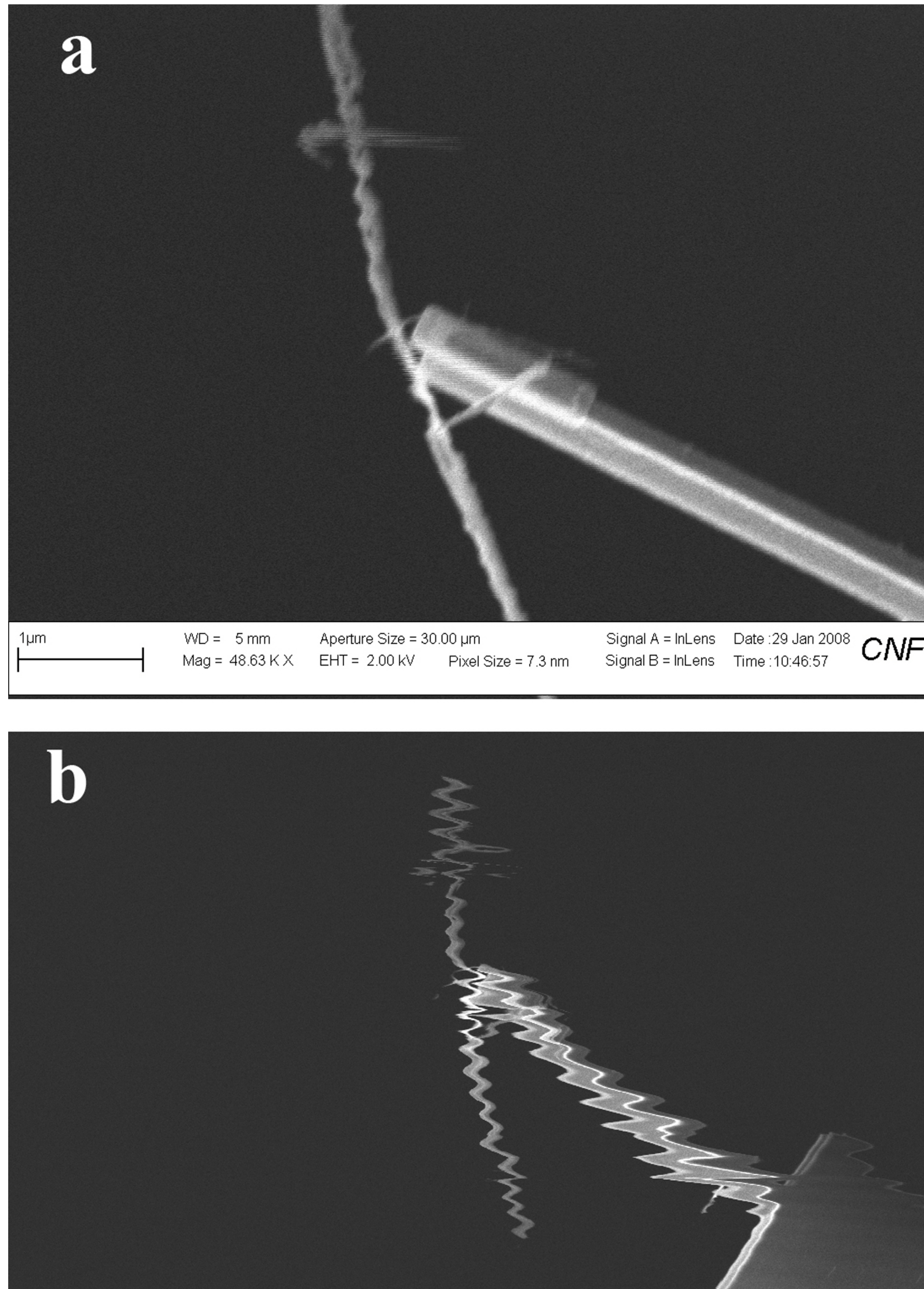

Figure 5.6: SEM images showing the end of a cantilever with some debris attached. (a) This image was taken quickly, with no signal averaging, to minimize the oscillations. (b) This image was taken using a pixel averaging mode, which increases the beam dwell time in each pixel, and results in significantly more apparent cantilever oscillation.

Table 5.1: Measured cantilever and tip magnet properties. All of the cantilevers studied had dimensions of 200 μm by 4 μm by 0.34 μm. Every cantilever produced on the same wafer as B and C has shown a $Q > 10^5$. l_m, w_m, and t_m are the length, width and thickness of the magnet, and l_{over} is the length the magnet overhangs the cantilever tip. f_0, k and Q are the measured frequency, spring constant, and quality factor for the cantilever's first mode of oscillation. μ_s is the tip saturation magnetic moment, ΔN is the calculated difference in the demagnetization factors for the nanomagnet along the cantilever's thickness and length, and $\mu_0 M_s$ is the saturation magnetization of the magnet. The magnetometry data from cantilever C was only fit between -4 and 4 T.

	A	B	C	D	
l_m	1500	1475	1475		nm
w_m	200	110.6	123		nm
t_m	50	100	100		nm
l_{over}	0	349	279		nm
f_0	8778	8920	8705	8928	Hz
k	0.78 ± 0.13	0.78 ± 0.03	0.87 ± .08	0.71	mN/m
Q	86 500	235 000	189 000	85 000	
μ_s	8.04 ± 1.29	5.24 ± 0.24	5.85 ± 0.53		fA/m^2
ΔN	0.54 ± 0.09	0.69 ± 0.03	0.71 ± 0.07		
$\mu_0 M_s$	0.68 ± 0.11	0.40 ± 0.08	0.41 ± 0.04		T

selected for analysis by cantilever magnetometry. These were drawn from two different wafers, produced 6 months apart. All of the cantilevers analyzed were 200 μm long. Table 5.1 presents the data for these cantilevers. Data for cantilever D, produced on the same wafer as cantilever A but without a tip magnet, is included to show that the addition of the magnet does not significantly modify the cantilever properties.

From the data for the best cantilever analyzed, the calculated minimum detectable force at 4.2K is 3.7 attonewtons in a 1 Hz bandwidth. This is a 4x im-

provement over the best cantilever produced by Jenkins [36].

The saturation-magnetization magnetometry measurements show that the tip magnets are almost fully magnetized. The large uncertainty in the $\mu_0 M_s$ value is primarily from uncertainty in the measurement of the spring constant. The difference between cantilever A and cantilevers B and C is attributed to differences in processing, and not caused, we believe, by the larger magnet overhang distance of cantilevers B and C.

ESR-MRFM measurements were done with cantilever B, to confirm that the overhanging tip magnet material was magnetic. The measured spin-induced cantilever frequency shift is shown in Figure 5.7(a) as a function of applied magnetic field. The field at which spins far away from the tip are in resonance is estimated to be near 0.62 T. The negative-going high-field peak in Figure 5.7(a) is attributed to a small number of spins just below the tip, where the field from the tip opposes the applied static magnetic field. The amplitude and lineshape of the mechanically detected resonance signal – particularly the "local" high-field peak – is a very sensitive function of the shape and magnetization of the tip's leading edge.

In Figure 5.7(b) the observed signal (circles) is compared to the signal calculated numerically by modeling the tip as a uniformly magnetized cuboid (solid lines). The sample temperature is taken to be $T = 11\,\mathrm{K}$ based on prior work with larger tips affixed to the cantilever by hand. The signal calculated assuming that the entire overhanging region is damaged and nonmagnetic is essentially zero (Model 1), completely inconsistent with the observed signal. Assuming a fully magnetized tip (Model 2), on the other hand, overestimates the signal size and the width of the local signal, suggesting that the tip may be partially damaged.

Signal was therefore simulated for two additional models of tip damage. In Model 3 the lower 50 nm of the tip is assumed to be magnetically dead while in Model 4 a uniform 12 nm thick magnetic dead layer is assumed. Both of these models better reproduce the width of the local signal, but the agreement between simulated and observed lineshape is not quantitative. The most likely reason for this disagreement is that the tip geometry deviates from the ideal cuboid geometry assumed in the simulation. The general agreement between observed and calculated signal seen in Figure 5.7(b) for models 3 and 4 nevertheless allows the conclusion that the tip's leading edge is well magnetized with a damage layer no thicker than ∼15 nm. The accuracy of the simulation model was confirmed by excellent agreement between predicted and recorded signal using the same TEMPO sample and a cantilever with a μm-diameter hand-glued nickel magnet [118].

The dissipation and jitter, as a function of distance above the gold-coated sample, were measured for cantilever B, in vacuum at 4.2K. The dissipation data is shown in Figure 5.8. This excellent result shows that surface-induced dissipation is less than the intrinsic dissipation until the magnet is ∼ 10 nm from the surface. This is a dramatic improvement over the dissipation measured using a bare silicon cantilever of the same leading edge dimensions (though 395 μm long), over a similar gold-coated polymer sample (Figure 5.9) [11]. The dissipation of the bare cantilever increases above the intrinsic dissipation at a distance of ∼ 130 nm above the surface. This is a complete validation of the hypothesis that smaller, metal tips extending the silicon cantilever body will experience much smaller surface-induced dissipation than a similar cantilever with a non-overhanging magnet.

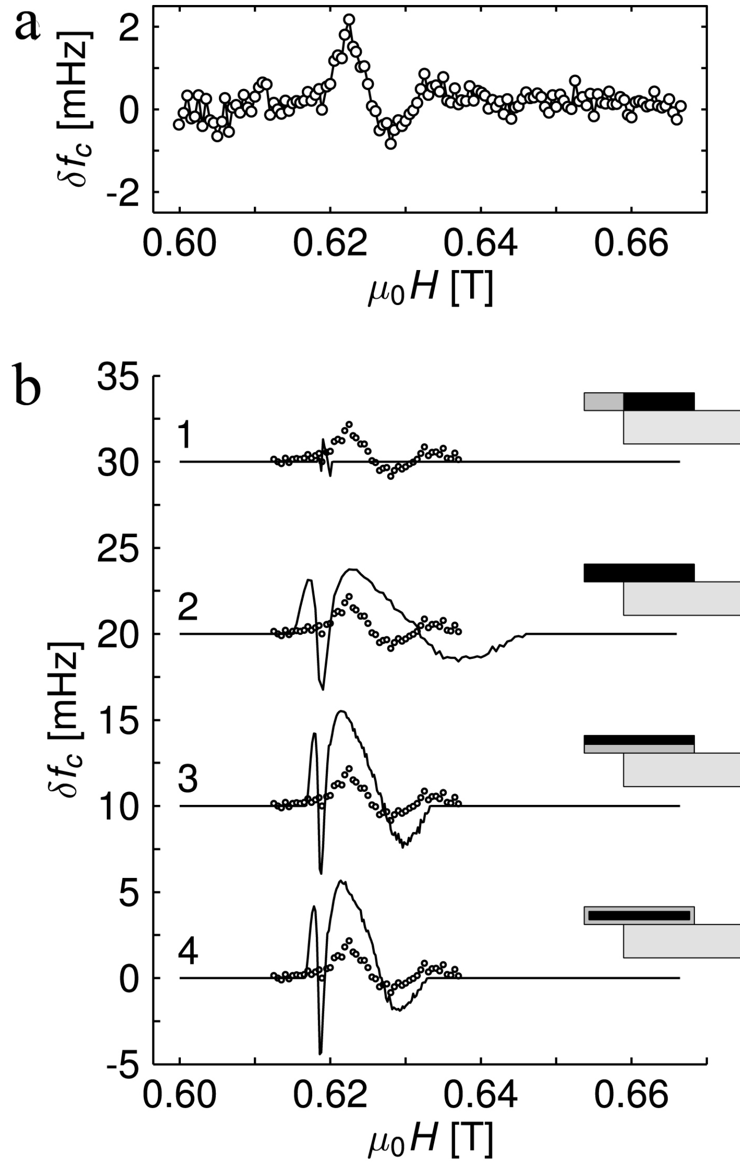

Figure 5.7: ESR-MRFM data collected with cantilever B, and associated modeling to estimate the size of the magnetically dead layer.

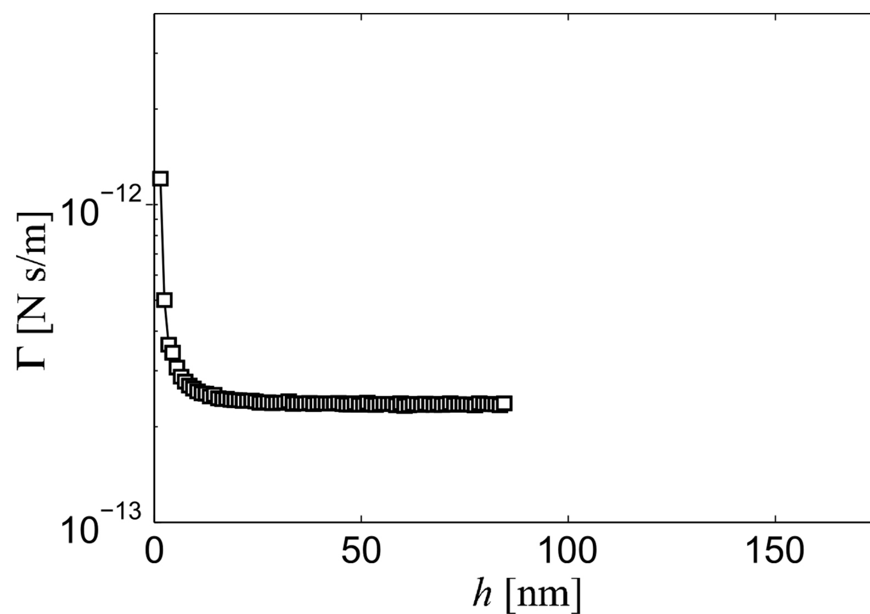

Figure 5.8: Dissipation versus tip-sample separation data collected with cantilever B over a gold coated polymer sample, at 4.2K.

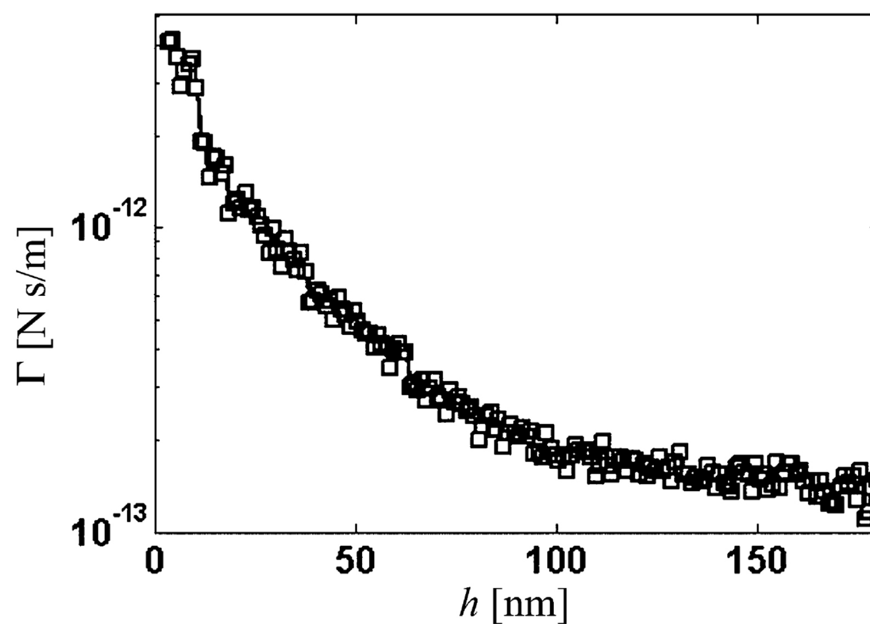

Figure 5.9: Dissipation versus tip-sample separation data collected with a bare silicon cantilever, over a gold surface at 4.2K.

Figure 5.10 shows the jitter spectrum for cantilever B, taken at several distances from the surface. The intersection between the surface-induced jitter, which has a frequency dependence proportional $1/f$, and the detector frequency noise, which is proportional to f^2, results in a different optimum frequency of lowest frequency noise at each tip-sample separation. Figure 5.11 shows the frequency noise at this optimum frequency as a function of distance. This graph shows that surface-induced jitter increases above the thermal minimum at much greater distances than surface-induced dissipation, for reasons that are not clear. This result is less promising for the application of these cantilevers in frequency shift MRFM experiments, as it limits their use in measurements at close tip-sample separation to amplitude-shift [4] rather than frequency shift [15, 18] detection protocols.

5.7 Other Applicable Analysis Techniques

There are several other techniques that might be able to determine the material or magnetic properties of the tip magnets, to non-destructively verify the success of the fabrication process. In the area of material analysis is scanning transmission electron microscopy (STEM) with electron energy loss spectroscopy (EELS). The overhanging portion of tip magnets is less than 100 nm thick and is therefore amenable to STEM-EELS analysis without the need for destructive material thinning. The combined STEM-EELS data can show crystal grain sizes, elemental content, and material electronic state with nanometer resolution. The electronic state information would allow one to distinguish between elemental nickel, and nickel in compounds such as oxides or silicides. It is the lack of electronic state information that makes other elemental identification techniques

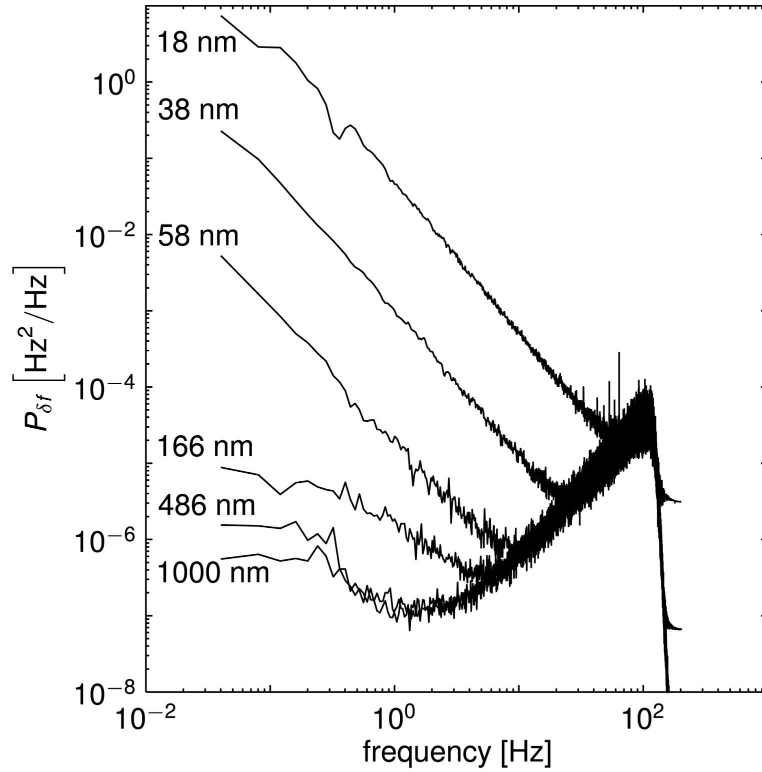

Figure 5.10: Power spectrum of frequency noise measured for cantilever B at various heights over a gold coated polymer surface.

less useful, techniques such as energy dispersive X-ray spectroscopy and Auger electron microscopy. X-ray photoelectron spectroscopy might be able to differentiate between elemental nickel and nickel in compounds, but does not have the spatial resolution needed, with X-ray spot sizes at least several μm across.

Methods to directly measure the magnetic field from the tip magnet could be used, with modeling, to determine the magnetic material structure. This data could also be used to map out the tip field gradient, necessary for successful image reconstruction in an MRFM imaging experiment.

Three techniques identified with this capability are electron holography [119], scanning SQUID magnetometry [120], and scanning diamond NV cen-

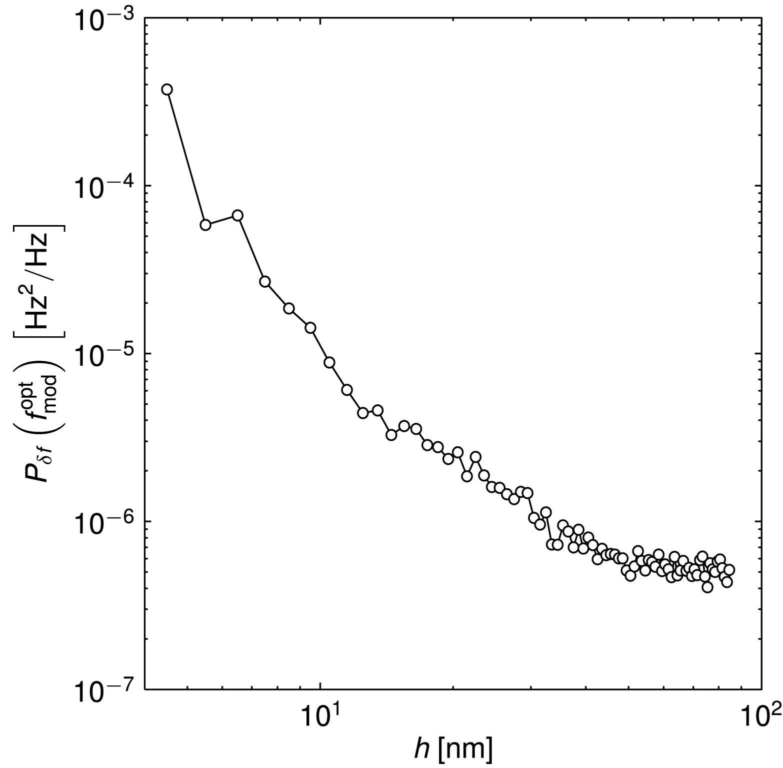

Figure 5.11: Frequency noise power at the optimum frequency versus height measured for cantilever B.

ter magnetometry [121]. The field gradient of interest is that of the tip magnet in saturation, which requires operating in an applied magnetic field with a magnitude on the order of the tip magnet material's saturation magnetization. This rules out N-V diamond magnetometry. It would also introduce a fair degree of difficulty in using electron holography and scanning SQUID magnetometry. For such an electron holography measurement, the applied field would need to be homogeneous over the entire electron beam path. For scanning SQUID magnetometry, the applied field would need to be very steady, as minute changes in the applied field magnitude would appear as changes in the tip magnetic field. Additionally, to achieve the required spatial resolution the SQUID detection loop would need to be much smaller than so far demonstrated [122].

Briefly, electron holography can produce images of magnetic field lines with sub-μm resolution, and give quantitative measurement of the field at any point in the image [123]. The technique is based on the interaction between the magnetic field and a beam of electrons, creating interference patterns in the electron beam image. Scanning SQUID magnetometry can map out the spatial field magnitude from the tip magnet. A nanoscale scanning SQUID demonstrated a field resolution of 74 bohr magnetons per root hertz with a detection loop of 0.3 square μm [122].

While these other methods might yield corroborating evidence of tip magnetization, it seems unlikely that they will produce more detailed information about tip magnetization and damage layer thickness and shape than MRFM measurements combined with STEM-EELS.

CHAPTER 6

CONCLUSION AND FUTURE DIRECTIONS

There are a few future directions possible for this work: using materials with a higher saturation magnetization, adding a protective coating to prevent magnet oxidation and reaction with silicon during processing, decreasing the magnet size, and increasing the cantilever sensitivity. Initial work has been done in all these areas, and the last three will be considered in more detail.

6.1 Better Cantilever Force Sensitivity

Returning to equation 1.8 and momentarily disregarding the quality factor, increased force sensitivity can be realized by making the cantilevers longer, narrower, or especially, making them thinner. Two factors limit this progression towards long, narrow, and very thin cantilevers: the increase in frequency noise at low frequencies, and the decrease in Q with decreasing oscillator volume. A single experiment was run to explore the limits of cantilever length using this fabrication protocol. The long cantilevers were of the same width and thickness as the other cantilevers produced in this work, but were 1 and 1.5 mm long. Small flutes (see Figure 6.1) were added to the base of these cantilever, to reduce the strain at the clamping point. Yields were surprisingly high, 79 % and 57 %, compared to the 43 % yield for 395 μm long cantilevers produced on the same wafer. Optically, the cantilevers showed no sign of curling, indicating that the silicon is virtually strain-free. While the cantilever properties have not been measured, the theoretical minimum detectable force at 4.2K, assuming a moderate Q of 50000, are 3.5 and 2.9 attonewtons, respectively. The calculated

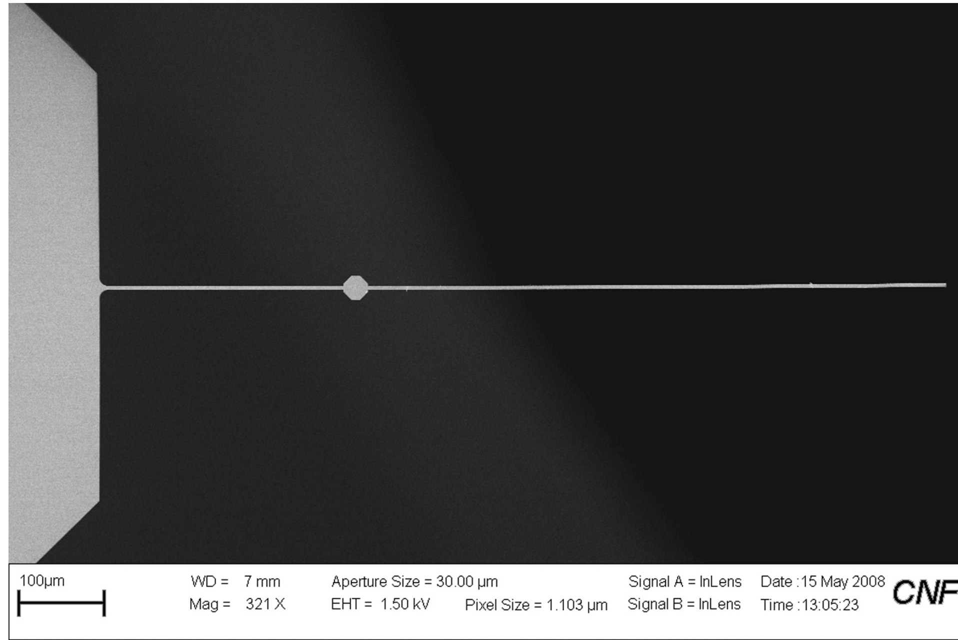

Figure 6.1: SEM image of a 1 millimeter long cantilever.

resonance frequencies are very low, around 440 and 200 Hz, respectively.

6.2 Smaller Magnets

Maximizing equations 1.11 and 1.12 finds that, for force detection of magnetic resonance, the optimum magnet radius for a given magnet-sample separation is 3 times the separation. This is calculated for spherical magnets, but should be similar to the optimal separation versus magnet radius ratio for the magnets produced in this work, which tend to have rounded corners. Based on the dissipation measurements reported in Chapter 5, the cantilever used in those measurements should be able to operate at the thermal noise limit 10 nm from the sample surface. The magnet in that measurement was approximately twice the optimal diameter for that separation. Shrinking the magnet to the optimal size

of ~ 60 nm should decrease surface-induced dissipation further, allowing for an even smaller magnet-sample separation. One of the goals moving forward on this work is to decrease the magnet dimensions to 50 nm and below.

The smallest overhanging magnets produced in this work were approximately 50 by 50 nm, made on test structures during development work on the potassium hydroxide underetch. The smallest magnets fabricated on finished cantilevers were ~ 70 by 100 nm, though they have not been analyzed by cantilever magnetometry.

As magnet width decreases, successful fabrication becomes increasingly difficult, the ends of the magnets more rounded, and the edges rougher[1]. This rounding and roughening is due to the resolution of the e-beam tool, the molecular structure of the polymer resist, and the mechanics of the lift-off process. Of these three, it is the liftoff process that sets the limit on magnet size. As the magnet width decreases, it becomes increasingly difficult for the evaporated metal to reach the bottom of the resist pattern, and more likely to adhere to the sides of the resist, and in the worst case pinches off the resist pattern, allowing no metal in. Thinning the resist mitigates this to some degree, but also reduces the amount of material that can be deposited. Material deposited on the sidewalls makes it difficult to lift-off the unwanted metal on top of the resist, and often leaves jagged edges to the magnets from sidewall material that remained stuck to the magnet. Reducing the magnet width to below 70 nm, although well above the stated 15 nm resolution of the e-beam tool, is clearly not as simple as changing the feature size on the software layout.

Process development was done targeting a 30 nm wide, 20 nm thick magnet.

[1] Magnets can be made almost arbitrarily thin by decreasing the amount of material deposited.

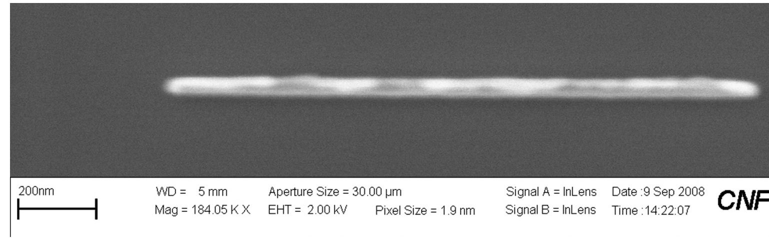

Figure 6.2: Sub 50 nm wide cobalt magnet test structure fabricated on a silicon wafer.

Factors varied were magnet size in CAD, resist thickness, resist development method, and remnant resist removal or "descum" method. To allow for the thin resist layers needed, a single layer of resist was used, rather than the bilayer used for larger magnets. The best result obtained is a ~ 40 nm wide, 30 nm thick cobalt magnet, produced on a bare silicon wafer (Figure 6.2). When the process was repeated using an SOI wafer, no magnets were found after the cantilever etch step, the first time that the magnets locations could be identified. The observed zero yield was attributed to the difference in secondary electron yield between bare silicon and SOI wafers. Further development work towards smaller magnets needs to be conducted on SOI wafers, which will greatly increase the development cost.

As the size of the magnet decreases to the tens of nanometers range, preventing damage to the magnetic material from oxidation or silicide formation becomes extremely critical. Nonmagnetic material, especially on the magnet leading edge, effectively decreases the size of the magnet, requiring an even closer approach to the spins in order to achieve the maximum signal per spin. In other words, this same magnetically dead material effectively buries the spin deeper beneath the surface of the sample, in terms of how close the leading edge of the (dead layer) of the magnet must be to the sample surface. Returning

again to the simplified spherical model, if a 30 nm diameter magnet had a 5 nm oxide layer, it would be impossible to reach the optimum approach for the 20 nm effective magnet, before the sphere impacted the surface. Development of preventative schemes for oxidation and silicide formation are therefore crucial to achieving single proton sensitivity via mechanical detection.

6.3 Other Magnetic Materials

Stronger magnetic field gradients, and thus better magnetic force sensitivity, could be realized by using a higher saturation magnetization material such as iron or cobalt. After successful fabrication of nickel magnets, the same process was used to attempt to produce similar cobalt magnet-tipped cantilevers[2]. The first trials were unsuccessful, and extensive SEM analysis during subsequent fabrication runs found that the cobalt magnets were transformed into large blobs (Figure 6.3). Further investigation found that the blobs formed after the SF_6 RIE plasma cantilever body etch, but the morphological change was only visible after the wafer had been allowed to sit overnight, in the cleanroom. Energy dispersive X-ray spectroscopy (EDS) analysis of the blobs, using a Bruker Esprit EDS attached to a Zeiss Supra 55 SEM, identified the presence of chlorine, which was found nowhere else on the wafers examined (Figure 6.4). At the time of writing, the favored hypothesis is that, by an unknown mechanism, the cobalt is converted to cobalt chloride during the cantilever body etch, which then overnight absorbs moisture from the cleanroom air to become cobalt chloride hydrate. This explains both the presence of chlorine, the overnight morphological change, and the significant magnet volume change.

[2]Iron was not tried because of the expected difficulty in preventing iron oxidation.

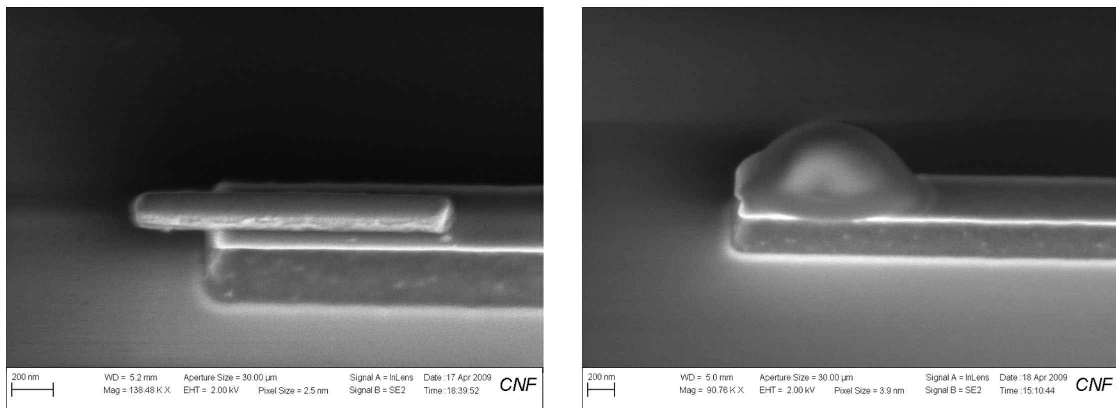

Figure 6.3: Cobalt magnet after the cantilever body etch (left), and a "blob" on the same wafer after it was left to sit overnight in the cleanroom.

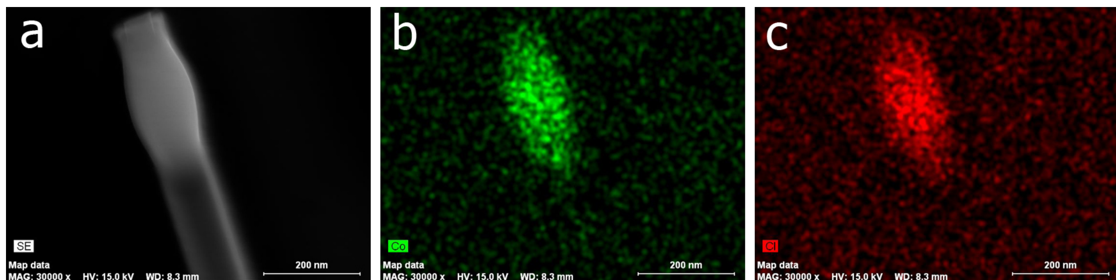

Figure 6.4: Spatial map of EDS analysis of a blob from the same wafer as figure 6.3. (a) An SEM image of the blob analyzed. (b) The green dots indicate the spatial distribution of cobalt in the same area as shown in (a). (c) The red dots indicate the spatial distribution of chlorine in the same area as shown in (a).

6.4 Magnet Capping Layers

To prevent chlorine contamination of cobalt magnets, and the oxidation of magnet material during fabrication, conformal capping layers over the magnets could be deposited. Silicon oxide and aluminum oxide films deposited by atomic layer deposition were tried in preliminary experiments, and much thicker layers of PECVD silicon oxide were used during the early stages of this project, in conjunction with the KOH magnet underetch. As all are blanket deposition methods, covering the entire wafer with material, these are not suitable for a long-term capping layer, as they will need to be removed at the conclusion of cantilever processing to prevent degradation of the cantilever quality factor. Both SiO_2 and Al_2O_3 are reported to etch in HF [124], and so the capping layers could be removed as a part of the cantilever release process. By quickly moving the wafer through the necessary baths after the HF etch, and taking care to blanket the cantilevers in an inert atmosphere after the completion of the critical point drying process, the total time exposed to oxidizing environments can be minimized.

The results with ALD silicon oxide suggest that the 25 and 50 nm thick layers were too thin to be mechanically robust after the underlying silicon was removed – SEM's of test structures show that the silicon oxide was mostly or completely broken away after the SF_6 underetch (Figure 6.5), and more significantly it did not prevent the underlying cobalt magnets from reacting to form a presumed cobalt chloride (Figure 6.6). This assumption is based on similarity to other wafers on which cobalt chloride was confirmed by energy dispersive X-ray spectroscopy. ALD aluminum oxide was also tried, but work halted when it did not readily etch in buffered HF. The literature reference cited above did not

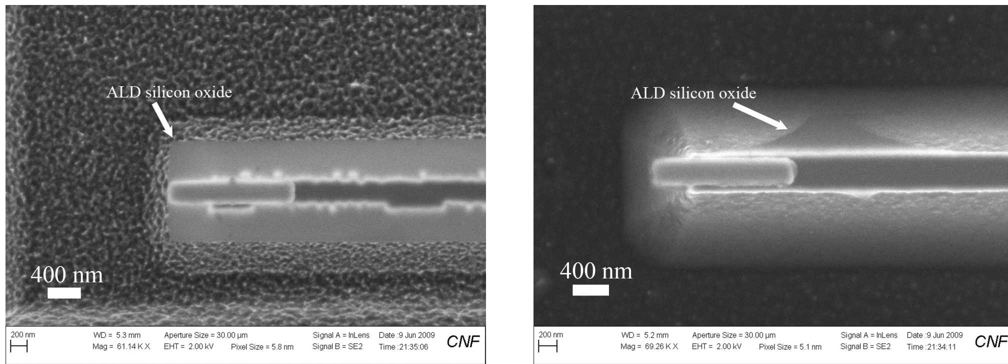

Figure 6.5: 50 nm ALD deposited protective silicon oxide film over cobalt magnet test structures. Images show an intact film (left) and one which has mostly broken away (right). The images were taken after the completion of the magnet underetch process step.

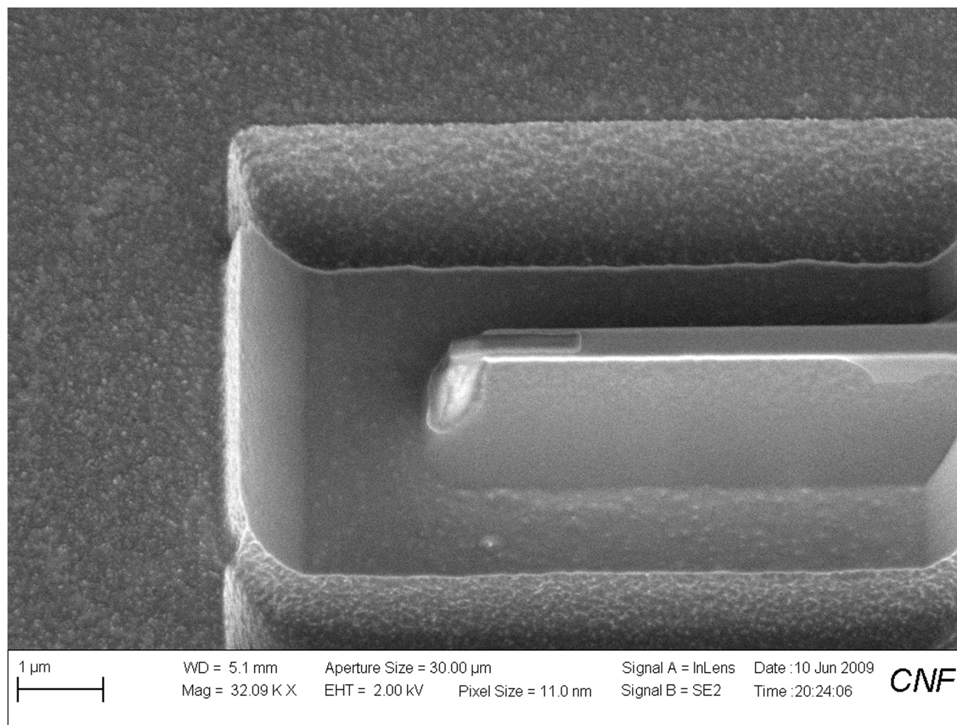

Figure 6.6: 50 nm ALD deposited protective silicon oxide film, which has failed to prevent chlorine contamination of the underlying cobalt magnets.

test buffered HF on an ALD Al_2O_3 film, which could explain the negative result. Sub - 1 nm nanometer thickness ALD Al_2O_3 films have been reported to allow 9 months of atmospheric storage of silver coated nanospheres without change to the silver layer, measured by continued activity in surface-enhanced Raman experiments [125].

In this work, a protocol to fabricate nanometer-scale magnets overhanging the ends of attonewton-sensitivity silicon cantilevers has been described, and demonstrated with nickel magnets as small as 70 by 100 nm. Properties of these cantilevers were confirmed by cantilever magnetometry and ESR-MRFM detection of the nitroxide electron spin label TEMPO in a perdeuterated polystyrene film. This work is a significant improvement on the fabrication protocol of Jenkins [36]. The magnets produced here are smaller and, because of the magnet overhang, have extremely low surface-induced dissipation.

For the first time, ESR-MRFM has been demonstrated with a batch-fabricated, magnet-tipped cantilever. This represents two important steps in the development of MRFM as a general analytical technique. By placing the magnet on the cantilever, the widest range of possible samples can be studied. And with batch fabrication of such cantilevers, a path to mass production and wide distribution of cantilevers is opened. In the probe used in this work, the cantilever was the only hardware component that was neither off-the-shelf nor could be easily produced by a commercial machine shop. Thus it is cantilever mass-production which limited commercial production of such an MRFM microscope. The process developed in this work now provides a pathway to such mass-production.

With these cantilevers, operating in a surface-dissipation limited ESR-

MRFM experiment at a 10 nm separation, a single electron spin should be detectable with a SNR of 5 (Modeling the magnet tip as a sphere of radius 70 nm, and with 1 second of signal averaging).

With the extremely low surface-induced force noise and high force sensitivity demonstrated by the cantilevers produced in this work, single proton detection is feasible. To reach this milestone, only the magnet needs improvement. Specifically, the size of the non-magnetic dead layer must be reduced. Further investment is warrented to develop protection schemes, compatible with the rest of the fabrication process, to eliminate magnet material damage.

APPENDIX A

FABRICATION PROCESS FOR OVERHANGING MAGNET-TIPPED CANTILEVERS USING SF_6 ETCHING

Notation for resist spinning

Resist spinning and baking information are listed in an abbreviated form:

Resist type / spin speed / spin time

Post-spinning bake temperature / bake time

Unless noted, all spinners were set to accelerate at 1000 rpm/sec.

All solvents were obtained from Fisher Scientific or J. T. Baker and used as received.

All metals were obtained from Kurt J. Leskar.

E-beam resists were obtained from Microchem, supplied in solvent.

A.1 Alignment Mark Preparation

1. Resist Bilayer

   (a) 495,000 MW poly(methyl methacrylate) (495PMMA), 8 % by weight in anisole (A8)[1] / 3000 rpm / 70 sec
   Bake 170 °C / 20 min

   (b) 950,000 MW poly(methyl methacrylate) (950PMMA), 2 % by weight in methyl isobutyl ketone(M2) / 4000 rpm / 60 sec
   Bake 170 °C / 15 min

[1]If a specified concentration of resist is unavailable, the next higher or lower concentration can be used, adjusting the spin speed to give the same approximate resist thickness.

2. E-beam pattern writing

   A JEOL JBX9300FS gaussian beam tool was used for all electron beam lithography in this work.

   (a) Magazine file "zerolayer" (unless specified otherwise, all magazine and associated files are in directory "hickman" on the JEOL tool.)
   (b) Before running job, run calibration routines CURRNT, INITBE, INITAE, HEIMAP.
   (c) Electron dose 2000 μCouloumbs cm^{-2}
   (d) Run job.

3. Resist development

   (a) Soak in 1:3 methy isobutyl ketone (MIBK) : isopropanol (IPA) solution for 75 sec with gentle agitation.
   (b) Spray-rinse with IPA, blow dry with nitrogen.
   (c) Remove any residual resist (descum) in the feature areas using the Glen 1000 oxygen plasma cleaner, recipe # 3, 100 watts, 60 sec. Place wafers on shelf B, set up to operate in RIE mode. (The same tool and process is used for all resist descums, and will hereafter simply be called "descum").

4. Metal Evaporation

   CVC SC4500 electron-gun evaporator used for all metal evaporations. The CNF has two such tools, the "odd hour" tool was usually used.

   All metals used were from CNF supplied stock, sourced from Kurt J. Leskar.

   Chrome (99.95% purity): 50 Å deposited at ~ 2.5 Å/sec

   Platinum (99.9% purity): 1000 Å deposited at ~ 2.5 Å/sec

5. Lift-off

   (a) Soak in ~ 1:1 acetone : methylene chloride (MeCl) solution for 10-15 minutes, until no metal is visible on the wafer surface [2].

   (b) Remove wafer from lift-off bath, constantly spraying with IPA to prevent metal particles from drying on the wafer surface.

   (c) Blow dry with nitrogen.

A.2 Magnet Preparation

1. Resist bilayer [3]

   (a) 495 PMMA A8 / 3000 rpm / 70 sec
   Bake 170 °C / 20 min

   (b) 950 PMMA M2 / 4000 rpm / 60 sec
   Bake 170 °C / 15 min

2. E-beam pattern writing

   (a) Magazine file "onelayer_magnetom_0109". This will define magnets 50, 100, and 200 nm wide by 1500 nm long on 200 μm long cantilevers.

   (b) Electron dose 1800 μCouloumbs cm^{-2}

   (c) Before job, run calibration files CURRNT, INITBE, INITAE, SFOCUS, HEIMAP.

[2] Concerns about chlorine contamination from the MeCl has prompted use of pure acetone lift-offs. This requires either several hours of soaking or sonication.

[3] The resist bilayer base layer thickness should be ≥ 2x the desired magnet thickness. The procedure presented here works for magnets up to 200 nm thick.

(d) Determine proper gain setting using the program ACGRG. Mark position for this program is 158250, 43140. Marks are 3 μm wide, 2000 μm long. Set sweep position 90 μm from mark center. All other settings, such as scan time, number of scans, and sweep width, depend on the quality of the marks and how well the wafer is loaded in the tool chuck.

(e) Check gain settings and alignment quality by running SETWFR.

(f) Run job.

3. Resist development

   (a) Soak in 1:3 MIBK : IPA solution for 75 sec with gentle agitation.

   (b) Spray-rinse with IPA, blow dry with nitrogen.

   (c) Descum.

4. Metal Evaporation

   Chrome: 50 Å deposited at ~ 2.5 Å/sec

   Cobalt or Nickel (99.995 % purity): deposit at ~ 2.5 Å/sec

5. Lift-off

   (a) Soak in 1:1 acetone : MeCl solution for 10-15 minutes, until no metal is visible on the wafer surface.

   (b) Remove wafer from lift-off bath, constantly spraying with IPA to prevent metal particles from drying on the wafer surface.

   (c) Blow dry with nitrogen.

A.3 Etch Pit Preparation

1. Resist layer

   495 PMMA A8 / 2000 rpm / 75 sec

   Bake 170 °C / 20 min

2. E-beam pattern writing

   (a) Magazine file "twolayer_magnetom_0109".

   (b) Electron dose 1800 μCouloumbs cm^{-2}

   (c) Before job, run calibration files CURRNT, INITBE, INITAE, SFOCUS, HEIMAP.

   (d) Determine proper gain setting using the program ACGRG. Set sweep position 70 μm from mark center.

   (e) Check gain settings and alignment quality by running SETWFR.

   (f) Run job.

3. Resist development

   (a) Soak in 1:3 MIBK : IPA solution for 75 sec with gentle agitation.

   (b) Spray-rinse with IPA, blow dry with nitrogen.

   (c) Descum.

A.4 Etch Pit Etching

SF_6 / O_2 RIE etch in Oxford Plasmalab 80. The CNF has two of these tools, the "MOS clean" tool #2 was used.

1. Run a 15 minute oxygen plasma chamber clean.
2. Without venting the chamber, run a 5 minute seasoning SF_6 / O_2 plasma.
3. Load wafer in center of platen, using quartz chips around the rim to keep wafer in place.
4. Run 40 sec etch [4]. Tool settings most recently used were 20 SCCM SF_6, 10 SCCM O_2, 200 W, chamber pressure 200 mTorr.
5. Resist removal
   (a) Soak in ~ 1:1 acetone : MeCl solution for about half of the time it took to remove the metal during the lift-off processes.
   (b) Remove wafer from lift-off bath, constantly spraying with IPA.
   (c) Blow dry with nitrogen.

A.5 Cantilever Body Preparation

1. Resist layer
   (a) Prime wafer with Microposit P-20.
   (b) Shipley SPR 700 1.2 (Microchem)/ 4000 rpm / 40 sec
       Bake 90 °C / 60 sec
2. Cantilever exposure

   Exposed on GCA AS200 Autostep I-line stepper.
   (a) Mask is “Magnetometry frontside all short”.

[4] Etch time is rate dependent, and as of 9/6/2009 generated a ~ 400 nm magnet overhang. The etch rate should be checked periodically and etch time adjusted. This also should be done after any major change to the tool.

(b) Stepper account is [100,66] with password “STEVE”.

(c) Run setup before exposing.

(d) Exposure command is “MAP CANT\MAP,EXPO”, exposure time 0.15 sec, alignment mark tone negative (N).

(e) Once alignment marks are found, manually rotate wafer chuck for coarse alignment, then use keyboard for fine rotation and position alignment.

(f) Note alignment residuals.

3. Post-exposure bake 115 °C for 60 sec.

4. Develop in Hamatech automated wafer developer, process “300 MIF 60 sec DP”.

5. Use optical microscope to check cantilever to etch pit alignment. If poor, strip resist in acetone and re-shoot.

A.6 Cantilever Body Etching

1. Follow steps 1-4 of “Etch pit etch”.

2. Resist removal

   (a) Soak in acetone for 2 minutes, with sonication.

   (b) Spray rinse with IPA.

   (c) Blow dry with nitrogen.

A.7 Protective Top Silicon Oxide Deposition

GSI UltraDep plasma-enhanced chemical vapor deposition tool (PECVD)

1. Run the automated clean recipe with a 10 minute clean time.
2. Deposit silicon oxide on front of wafer using recipe "N1.46 undoped oxide", deposition temperature of 275 °C. 325 sec deposition time. Target layer thickness is 1.6 μm [5] .

A.8 Backside Silicon Oxide Deposition

1. Run immediately following the top silicon oxide deposition.
2. Same recipe as the top silicon oxide, but with a deposition time of 430 sec, for a target layer thickness of 2 μm.

A.9 Backside Resist Preparation

1. Resist layer
   (a) Prime with P-20.
   (b) Shipley SPR 200 7.0 (Rohm and Haas electronic materials) / 500 rpm (accel at 250 rpm / sec) / 5 sec // 1800 rpm / 40 sec.
   For adequate coverage use two droppers of resist.
   Bake 115 °C / 60 sec. Do not quench after the bake.

[5] Silicon oxide layer thickness set by the thickness of the buried silicon oxide layer and the relative etch rates of the buried silicon oxide and the deposited silicon oxide. See Section 3.5.3.

2. Expose on electronic visions EV-620 contact aligner. Use the backside alignment, soft contact recipe “Marohn_harrell2” with a 25 sec exposure time. Mask is “magnetometry backside all short”.
3. Develop in Hamatech, recipe “300 MIF 120 sec DP” followed by “300 MIF 60 sec DP”.
4. (Opt) Place wafer in 90 °C oven for >8 hour hard bake, if not done after the backside silicon oxide etch.

A.10 Backside Silicon Oxide Etch

CHF_3 / O_2 RIE in Oxford Plasmalab 80.

1. Run a 5 minute oxygen plasma chamber clean.
2. Load wafer in center of platen, using quartz chips around the rim to keep wafer in place.
3. Run a 20 minute CHF_3 / O_2 etch. Tool settings most recently used (80 #2) were 50 SCCM CHF_3, 2 SCCM O_2, 240 W, chamber pressure 40 mTorr.
4. Check if silicon oxide was completely removed – etched areas will look like standard silicon when removal complete.
5. Repeat steps 3 and 4 until silicon oxide is removed.
6. (Opt) Place wafer in 90 °C oven for >8 hour hard bake. This can also be done before the backside silicon oxide etch.

A.11 Through-wafer Silicon Etch

Bosch-process deep RIE using a Unaxis 770 tool.

1. Run 200 loops of recipe "1thru".
2. Measure the etch depth using a P–10 mechanical stylus profilometer.
3. Let etcher cool for 15 minutes, then run an additional 200 loops of "1thru".
4. Measure etch depth, and from calculated etch rate determine the number of additional loops needed to reach a 400 μm etch depth.
5. Let etcher cool 15 minutes, then etch to 400 μm depth. If it requires more than 200 loops of "1thru" to reach that depth, split into two etches, letting tool cool 15 minutes between etches.
6. Strip resist in a 2 minute acetone soak.
7. Attach handler wafer to front of SOI wafer with Cool Grease 7016 thermally conductive paste [6] .
8. For the last 100 μm of the through-wafer etch, the etch rate is progressively slowed and the cooling period between etches somewhat increased. There is no set steps for this process. When in doubt, allowing greater cooling periods is always better. The general process followed is to run 50 loops per cycle until the handle silicon clears nearest the edge of the wafer, then run 25 loops per cycle until the etch is finished.
9. Continue etching until all the handle silicon is removed under the cantilevers (determined by optical microscopy) or the membrane cracking be-

[6]Handler wafer created by etching a standard silicon wafer ~ 200 μm deep in the Unaxis 770. The rim is created by the area of silicon protected by the wafer clamp.

comes severe (see chapter 3 for a more detailed discussion of the end of the through-wafer silicon etch).

A.12 Release

1. Remove handle wafer using a razor blade to carefully pry wafers apart.
2. Remove cool-grease with acetone-soaked swabs.
3. Buffered hydrofluoric acid (BOE) silicon oxide etch.
   (a) Place Teflon transfer boat in a plastic tub. Fill tub with 6:1 BOE (35% NH_4OH, 7% HF, in H_20, J. T. Baker) so that that the liquid level is ~ 1 cm above the rim of the transfer boat.
   (b) Place wafer face-up in the transfer boat, and let etch for 6 minutes.
   (c) Move transfer boat and wafer to a water bath, keeping under liquid (in transfer boat) during the move.
   (d) Using the same transfer technique, run the boat and wafer through a total of 6 water baths.
   (e) Run the wafer through 3 IPA baths.

A.13 Critical point drying

Tousimis Automegasamdri CO_2 critical point dryer.

1. Set purge time to 5 (= 25 minutes).
2. Fill CPD chamber ~ 5 mm deep with IPA.

3. Quickly move wafer from transfer boat to chamber.

4. Run CPD process.

APPENDIX B

PROCESS MODIFICATION TO ELIMINATE PROTECTIVE FRONT SILICON OXIDE

The purpose of producing a wafer with no protective front silicon oxide is to allow SEM inspection of the magnets during the last stages of the through-wafer etch, to monitor for silicide formation.

B.1 Backside Silicon Oxide Deposition

GSI UltraDep PECVD

1. Run the automated clean recipe with a 15 minute main etch time. Extend the "wafer-unloaded" etch times to 4 minutes for the "clean" etch, and 2 minutes for the "high" etch.
2. Load SOI wafer face-down.
3. Run recipe "N1.46 undoped oxide", temperature of 400 °C. Target film thickness is 2.5 μm.

Follow procedure of appendix A, from A.1.1 through A.6.2.

B.2 Protective PMMA Front Coating

495 PMMA A11 / 2000 rpm / 75 sec

Bake 170 °C / 20 min

Follow process steps in appendix A for “backside resist preparation” and “backside silicon oxide etch”.

B.3 Through-wafer Silicon Etch with SEM Monitoring

Unaxis 770 Bosch deep RIE

1. Etch to a depth of ~ 350 μm with recipe 1thru. Use sets of 200 loops, allowing 15 minutes of cooling between each etch cycle.
2. Strip backside photoresist and frontside PMMA in a acetone or acetone / MeCl bath.
3. Magnets are now uncovered for SEM inspection.
4. Continue the through-wafer etch process, periodically inspecting the wafer with SEM.

B.4 Release

The release process is the same as in A.12 and A.13, with the BOE etch time shortened to 3 minutes because of the absence of the top silicon oxide. However, since the magnets will be exposed to the BOE for the entire etch, it is likely that the magnets will be damaged.

APPENDIX C

FABRICATION PROCESS FOR OVERHANGING MAGNET-TIPPED CANTILEVERS USING SILICON OXIDE PILLARS

C.1 Alignment Mark Preparation

1. Blanket aluminum deposition CVC SC4500 evaporator
   2000 Å of aluminum at ~ 5 Å/sec
2. Resist 495 PMMA A11 / 4000 rpm / 75 sec
   Bake 170 °C / 20 min
3. E-beam pattern writing
   (a) Magazine file “zerolayer”.
   (b) Electron dose 2000 μCouloumbs cm^{-2}
4. Resist development
   (a) Soak in 1:3 MIBK : IPA solution for 75 sec with gentle agitation.
   (b) Spray-rinse with IPA, blow dry with nitrogen.
   (c) Descum.

C.2 Alignment Mark Etching - Aluminum

Plasmatherm PT–740 chlorine etcher

1. Season chamber for 5 minutes using sapphire wafer.

2. Etch marks using recipe “aletch”. Etch times 3 minutes breakthrough etch, 5 minute aluminum etch, no passivation etch.
3. Immediately on unloading, place wafer in water tub, and then rinse using a spin-rise-dryer.

C.3 Alignment Mark Etching - Silicon and Silicon Oxide

CF_4 RIE etch in Oxford Plasmalab 80.

1. Run a 10 minute oxygen plasma chamber clean.
2. Without venting the chamber, run a 5 minute seasoning CF_4 plasma.
3. Load wafer in center of platen, using quartz chips around the rim to keep wafer in place.
4. Run 40 minute CF_4 etch. Target etch depth > 1 μm[1].
5. Resist removal
   (a) Soak in ~ 1:1 acetone : MeCl solution.
   (b) Remove wafer from lift-off bath, constantly spraying with IPA.
   (c) Blow dry with nitrogen.
6. Aluminum removal.

   Etch aluminum in wet chemical etch “aluminum etchant type A”.

[1]This can be monitored during calibration work with the P-10 profilometer. However, more critical than the actual depth is that the marks are deep enough to provide adequate contrast in the e-beam alignment process.

C.4 Silicon Nitride Layer Deposition

GSI UltraDep PECVD

1. Run the automated clean recipe with a 10 minute clean time.
2. Deposit silicon nitride on front of wafer using recipe "LS nitride", deposition temperature of 400 °C. Target layer thickness is 50 nm.

C.5 Silicon Nitride Mask Preparation

1. Resist
   495 PMMA A8 / 2000 rpm / 70 sec
   Bake 170 °C / 20 min
2. E-beam pattern writing
   (a) Magazine file "Ox_pillars_0609".
   (b) Electron dose 1800 μCouloumbs cm^{-2}
   (c) Before job, run calibration files CURRNT, INITBE, INITAE, SFOCUS, HEIMAP.
   (d) Determine proper gain setting using the program ACGRG. Set sweep position 70 μm from mark center.
   (e) Check gain settings and alignment quality by running SETWFR.
   (f) Run job.
3. Resist development
   (a) Soak in 1:3 MIBK : IPA solution for 75 sec with gentle agitation.

(b) Spray-rinse with IPA, blow dry with nitrogen.

(c) Descum.

4. Silicon nitride etch CHF_3 / O_2 RIE etch in Oxford Plasmalab 80.

   (a) Run a 10 minute oxygen plasma chamber clean.

   (b) Without venting the chamber, run a 5 minute seasoning CHF_3 plasma.

   (c) Load wafer in center of platen, using quartz chips around the rim to keep wafer in place.

   (d) Run 2 minute etch, recipe "Nitride etch".

5. Resist removal

   (a) Soak in ~ 1:1 acetone : MeCl solution.

   (b) Remove wafer from lift-off bath, constantly spraying with IPA.

   (c) Blow dry with nitrogen.

C.6 Silicon Oxide Pillar Growth

"Anneal 3" furnace, "wet oxide no HCL" recipe.
Run growth at 1100 °C for 85 minutes. Target silicon oxide thickness > 2.2x device layer thickness.

C.7 Silicon Oxide Pillar Chemical Mechanical Polishing

Strasbaugh 6EC chemical mechanical polisher, Pad IC 1000, Slurry Celexis CX495.
Run recipe “oxynitirde select”, polish time 85 seconds. The focus for the polish time is that the pillars are conformal with the device silicon.

C.8 Silicon Nitride Layer Removal

1. Soak wafer in boiling 85 % phosphoric acid solution, 30 minute etch time.
2. Rinse in spin-rinse-dryer.

C.9 Magnet Preparation

Same as the procedure in appendix A, with the magazine file for e-beam writing “mags_for_ox_pillars”.

C.10 Cantilever Body Etch

Same as the procedure in appendix A.

For the rest of the fabrication process, follow the procedure given in appendix A. With regards to the release etch time, the silicon oxide pillar effectively doubles the thickness of silicon oxide under the magnets. This requires doubling the BOE etch time. This, in turn, requires doubling the thickness of

the top protective silicon oxide layer, to ensure that the silicon oxide above and below the magnets clear at approximately the same time.

APPENDIX D

FABRICATION PROCESS FOR OVERHANGING MAGNET-TIPPED CANTILEVERS USING POTASSIUM HYDROXIDE UNDERETCHING

Follow the process given in appendix A for both alignment mark and magnet preparation, through A.2.5. For these two e-beam writes, the magazine files are "zerolayer.mgn" and "onelayer.mgn" in folder "garner" on the e-beam tool. However, since the optical masks for this process are likely destroyed, it is strongly recommended that all e-beam files be recompiled, and masks re-made, from the CAD file "Harrell 20050829 magnets and stepper cantilevers".

D.1 Thin Silicon Oxide Layer Deposition

GSI UltraDep plasma-enhanced chemical vapor deposition tool (PECVD)

1. Run the automated clean recipe with a 10 minute clean time.
2. Deposit silicon oxide on front of wafer using recipe "LS TEOS oxide", deposition temperature of 400 °C. 32 sec deposition time. Target layer thickness is 180 nm.

D.2 Etch Pit Preparation

1. Resist layer
   495 PMMA A11 / 4000 rpm / 75 sec
   Bake 170 °C / 20 min

2. E-beam pattern writing
    (a) Magazine file "twolayer" in folder "garner".
    (b) Electron dose 2000 μCouloumbs cm^{-2}
    (c) Before job, run calibration files CURRNT, INITBE, INITAE, SFOCUS, HEIMAP.
    (d) Determine proper gain setting using the program ACGRG. Set sweep position 70 μm from mark center.
    (e) Check gain settings and alignment quality by running SETWFR.
    (f) Run job.
3. Resist development
    (a) Soak in 1:3 MIBK : IPA solution for 75 sec with gentle agitation.
    (b) Spray-rinse with IPA, blow dry with nitrogen.
    (c) Descum.

D.3 Etch Pit Silicon Oxide Etching

CHF_3 / Ar RIE etch in Oxford Plasmalab 80.

1. Run a 15 minute oxygen plasma chamber clean.
2. Without venting the chamber, run a 5 minute seasoning CHF_2 / Ar plasma.
3. Load wafer in center of platen, using quartz chips around the rim to keep wafer in place.
4. Run 10 min etch, to clear through thin protective oxide layer.

D.4 Etch Pit Silicon Etching

SF_6 / O_2 RIE etch in Oxford Plasmalab 80.

1. Run a 15 minute oxygen plasma chamber clean.
2. Without venting the chamber, run a 5 minute seasoning SF_6 / O_2 plasma.
3. Load wafer in center of platen, using quartz chips around the rim to keep wafer in place.
4. Run 30 sec etch
5. Resist removal
   (a) Soak in a MeCl solution for about half of the time it took to remove the metal during the lift-off processes.
   (b) Remove wafer from lift-off bath, constantly spraying with IPA.
   (c) Blow dry with nitrogen.

D.5 Potassium Hydroxide Silicon Underetch

1. 50 % KOH solution, 70 °C etch temperature.
2. Etch wafers in a 182-39M or 182-39MU teflon wafer holder, keeping the wafers horizontal in the etch solution.
3. Etch time 70 seconds.
4. Rinse in DI H_2O bath, followed by a spin-rinse-dryer.

For the rest of the fabrication process, follow the procedure given in appendix A, starting with A.5.1, and using the appropriate masks for the cantilever and backside optical lithography processes. As noted above, the masks for these two exposures are likely destroyed, but can be recreated from the CAD file “Harrell 20050829 magnets and stepper cantilevers”.

APPENDIX E

CAD AND MASK SETS

All cad files are in L-EDIT format.

The .JDF and .SDF files have the same names as the associated magazine file.

For 395 μm long cantilevers, with 400 and 600 nm wide, 1500 nm long overhanging tip magnets.

CAD: "wide_mag_100_nm_fromedge_20070817"

Magnet magazine file: "onelayer_100nm_from_edge"

Etch pit magazine file: "twolayer_big_etchpit"

(Both of these files are in folder "GARNER" on the e-beam)

Front optical mask: "Hickman 200802 frontside no pass shift"

Back optical mask: "Harrell 20051013 backside no edge bead removal"

For 200 and 395 μm long cantilevers with 50, 100, and 200 nm wide, 1500 nm long overhanging tip magnets.

CAD: "magnetometry_01_29_08"

Magnet magazine file: "onelayer_magnetom_0108"

Etch pit magazine file: "twolayer_magnetom_0108"

Front optical mask: "Hickman 20080131 magnetometry front"

Back optical mask: "Hickman 20080206 magnetometry back"

For 1 and 1.5 mm long cantilevers with 400 and 600 nm wide, 1500 nm long overhanging tip magnets.

CAD: "wide_mag_100nm_long_20080328"

Magnet magazine file: "onelayer_longcant_0508"

Etch pit magazine file: "twolayer_longcant"

Front optical mask: “Hickman long levers front”

Back optical mask: “Hickman long levers back”

For 200 μm long cantilevers with 50, 100, and 200 nm wide, 1500 nm long overhanging tip magnets.

CAD: “magnetometry_01_17_09”

Magnet magazine file: “onelayer_magnetom_0109”

Etch pit magazine file: “twolayer_magnetom_0109”

Front optical mask: “magnetometry frontside all short”

Back optical mask: “magnetometry backside all short”

For 200 μm long cantilevers with 50, 100, and 200 nm wide, 1500 nm long overhanging tip magnets created by the silicon oxide pillars process.

CAD: “oxide_pillar_magnetom_060609”

Silicon oxide pillar magazine file: “ox_pillars_0609”

Magnet magazine file: “mags_for_ox_pillars”

Front optical mask: “magnetometry frontside all short”

Back optical mask: “magnetometry backside all short”

There are two cad files, with associated JEOL magazine files, that write arrays of rectangular boxes for test structures.

Array of 200, 400 and 600 nm wide, 1500 nm long rectangles, with 4 copies of the array per wafer.

CAD: “mega_mag_array_spc”

Magazine file: “vary_mag_array_4copies_spc2”

Array of 20, 30 and 50 nm wide, 1000 nm long rectangles, in sets of arrays with varying electron beam dose between each array.

CAD: “mega_mag_array_small”

Magazine file: “small_mag_array_varydose”

BIBLIOGRAPHY

[1] G. Binnig, H. Rohrer, Ch. Gerber, and E. Weibel. Tunneling through a controllable vacuum gap. *Appl. Phys. Lett.*, 40(2):178–180, 1982.

[2] J. A. Sidles. Noninductive detection of single-proton magnetic resonance. *Appl. Phys. Lett.*, 58(24):2854–2856, June 1991.

[3] J. Frank. Single particle imaging of macromolecules by cryo-electron microscopy. *Ann. Rev. Biophys. Biomol. Struct.*, 31(1):303–319, June 2002.

[4] C. L. Degen, M. Poggio, H. J. Mamin, C. T. Rettner, and D. Rugar. Nanoscale magnetic resonance imaging. *Proc. Nat. Acad. Sci.*, 106(5):1313–1317, February 2009.

[5] S. Subramaniam. Bridging the imaging gap: visualizing subcellular architecture with electron tomography. *Curr. Op. Microbio.*, 8(3):316 – 322, 2005.

[6] J. L.S. Milne and S. Subramaniam. Cryo-electron tomography of bacteria: progress, challenges and future prospects. *Nat. Rev. Micro.*, 7(9):666–675, 2009.

[7] G. P. Berman, G. D. Doolen, P. C. Hammel, and V. I. Tsifrinovich. Magnetic resonance force microscopy quantum computer with tellurium donors in silicon. *Phys. Rev. Lett.*, 86(13):2894, March 2001.

[8] Z. Zhang, P. C. Hammel, and P. E. Wigen. Observation of ferromagnetic resonance in a microscopic sample using magnetic resonance force microscopy. *Appl. Phys. Lett.*, 68(14):2005–2007, April 1996.

[9] H. J. Mamin, R. Budakian, B. W. Chui, and D. Rugar. Detection and manipulation of statistical polarization in small spin ensembles. *Phys. Rev. Lett.*, 91(20):207604, November 2003.

[10] J. A. Sidles, J. L. Garbini, K. J. Bruland, D. Rugar, O. Züger, S. Hoen, and C. S. Yannoni. Magnetic resonance force microscopy. *Rev. Mod. Phys.*, 67(1):249, 1995.

[11] S. Kuehn, S. A. Hickman, and J. A. Marohn. Advances in mechanical detection of magnetic resonance. *J. Chem. Phys.*, 128(5):052208, 2008.

[12] C. P. Slichter. *Principles of magnetic resonance*. Springer series in solid-state sciences, 1. Springer-Verlag, Berlin; New York, 1990.

[13] D. Rugar, C. S. Yannoni, and J. A. Sidles. Mechanical detection of magnetic resonance. *Nature*, 360(6404):563–566, December 1992.

[14] K. Wago, D. Botkin, C. S. Yannoni, and D. Rugar. Paramagnetic and ferromagnetic resonance imaging with a tip-on-cantilever magnetic resonance force microscope. *Appl. Phys. Lett.*, 72(21):2757–2759, May 1998.

[15] S. R. Garner, S. Kuehn, J. M. Dawlaty, N. E. Jenkins, and J. A. Marohn. Force-gradient detected nuclear magnetic resonance. *Appl. Phys. Lett.*, 84(25):5091–5093, June 2004.

[16] K. McDonald and J. R. McIntosh. Cryopreparation methods for electron microscopy of selected model systems. In *Cellular Electron Microscopy*, volume Volume 79, pages 23–56. Academic Press, 2007.

[17] H. J. Mamin, M. Poggio, C. L. Degen, and D. Rugar. Nuclear magnetic resonance imaging with 90-nm resolution. *Nature Nanotech.*, 2(5):301–306, May 2007.

[18] D. Rugar, R. Budakian, H. J. Mamin, and B. W. Chui. Single spin detection by magnetic resonance force microscopy. *Nature*, 430(6997):329–332, July 2004.

[19] B. C. Stipe, H. J. Mamin, C. S. Yannoni, T. D. Stowe, T. W. Kenny, and D. Rugar. Electron spin relaxation near a micron-size ferromagnet. *Phys. Rev. Lett.*, 87(27):277602, December 2001.

[20] S. Kuehn, R. F. Loring, and J. A. Marohn. Dielectric fluctuations and the origins of noncontact friction. *Phys. Rev. Lett.*, 96(15):156103–4, April 2006.

[21] S. M. Yazdanian, J. A. Marohn, and R. F. Loring. Dielectric fluctuations in force microscopy: Noncontact friction and frequency jitter. *J. Chem. Phys.*, 128(22):224706–13, June 2008.

[22] S. M. Yazdanian, N. Hoepker, S. Kuehn, R. F. Loring, and J. A. Marohn. Quantifying electric field gradient fluctuations over polymers using ultrasensitive cantilevers. *Nano Lett.*, 9(6):2273–2279, June 2009.

[23] E. Vidal Russell and N. E. Israeloff. Direct observation of molecular cooperativity near the glass transition. *Nature*, 408(6813):695–698, December 2000.

[24] S. Kuehn, J. A. Marohn, and R. F. Loring. Noncontact dielectric friction. *J. Phys. Chem. B*, 110(30):14525–14528, 2006.

[25] O. Cherniavskaya, L. Chen, V. Weng, L. Yuditsky, and L. E. Brus. Quantitative noncontact electrostatic force imaging of nanocrystal polarizability. *J. Phys. Chem. B*, 107(7):1525–1531, February 2003.

[26] A. Goj and R. F. Loring. Effect of noise on the classical and quantum mechanical nonlinear response of resonantly coupled anharmonic oscillators. *J. Chem. Phys.*, 124(19):194101–9, May 2006.

[27] P. Grutter, Y. Liu, P. LeBlanc, and U. Durig. Magnetic dissipation force microscopy. *Appl. Phys. Lett.*, 71(2):279–281, July 1997.

[28] Y. Liu and P. Grutter. Magnetic dissipation force microscopy studies of magnetic materials (invited). In *The 7th joint MMM-intermag conference on magnetism and magnetic materials*, volume 83, pages 7333–7338, San Francisco, California (USA), June 1998. AIP.

[29] W. Denk and D. W. Pohl. Local electrical dissipation imaged by scanning force microscopy. *Appl. Phys. Lett.*, 59(17):2171–2173, October 1991.

[30] T. D. Stowe, T. W. Kenny, D. J. Thomson, and D. Rugar. Silicon dopant imaging by dissipation force microscopy. *Appl. Phys. Lett.*, 75(18):2785–2787, November 1999.

[31] R.M. Stockle, Y.D. Suh, V. Deckert, and R. Zenobi. Nanoscale chemical analysis by tip-enhanced Raman spectroscopy. *Chem. Phys. Lett.*, 318(1 – 3):131 –136, 2000.

[32] D. J. Inman. *Engineering vibration*. Pearson Prentice Hall, Upper Saddle River, N.J., 2008.

[33] Y. M. Tseytlin. Atomic force microscope cantilever spring constant evaluation for higher mode oscillations: A kinetostatic method. *Rev. Sci. Instrum.*, 79(2):025102, February 2008.

[34] K. E. Petersen. Silicon as a mechanical material. *Proc. IEEE*, 70(5):420–457, 1982.

[35] T. D. Stowe, K. Yasumura, T. W. Kenny, D. Botkin, K. Wago, and D. Rugar. Attonewton force detection using ultrathin silicon cantilevers. *Appl. Phys. Lett.*, 71(2):288–290, July 1997.

[36] N. E. Jenkins, L. P. DeFlores, J. Allen, T. N. Ng, S. R. Garner, S. Kuehn, J. M. Dawlaty, and J. A. Marohn. Batch fabrication and characterization of ultrasensitive cantilevers with submicron magnetic tips. *J. Vac. Sci. Tech. B*, 22(3):909–915, Mayh 2004.

[37] B. C. Stipe, H. J. Mamin, T. D. Stowe, T. W. Kenny, and D. Rugar. Magnetic dissipation and fluctuations in individual nanomagnets measured by ultrasensitive cantilever magnetometry. *Phys. Rev. B*, 86(13):2874, March 2001.

[38] M. J. Vasile, D. Grigg, J. E. Griffith, E. Fitzgerald, and P. E. Russell. Scanning probe tip geometry optimized for metrology by focussed ion-beam milling. *J. Vac. Sci. Tech. B*, 9(6):3569 – 3572, November 1991.

[39] L. Folks, M. E. Best, P. M. Rice, B. D. Terris, D. Weller, and J. N. Chapman. Perforated tips for high-resolution in-plane magnetic force microscopy. *Appl. Phys. Lett.*, 76(7):909 – 911, February 2000.

[40] G. N. Phillips, M. Siekman, L. Abelmann, and J .C. Lodder. High resolution magnetic force microscopy using focused ion beam modified tips. *Appl. Phys. Lett.*, 81(5):865 – 867, July 2002.

[41] M. R. Koblischka, U. Hartmann, and T. Sulzbach. Improving the lateral resolution of the MFM technique to the 10 nm range. *J. Magnet. Magn. Materials*, 272(Part 3 Sp. Iss. SI):2138 – 2140, May 2004.

[42] A. R. Champagne, A. J. Couture, F. Kuemmeth, and D. C. Ralph. Nanometer-scale scanning sensors fabricated using stencil lithography. *Appl. Phys. Lett.*, 82(7):1111 – 1113, February 2003.

[43] H. J. Mamin, R. Budakian, B. W. Chui, and D. Rugar. Magnetic resonance force microscopy of nuclear spins: Detection and manipulation of statistical polarization. *Phys. Rev. B*, 72(2):024413, July 2005.

[44] N. I. Kato. Reducing focused ion beam damage to transmission electron

microscopy samples. *J Electron Microsc (Tokyo)*, 53(5):451–458, October 2004.

[45] A. G. Baker and W. C. Morris. Deposition of metallic films by electron impact decomposition of organometallic vapors. *Rev. Sci. Instrum.*, 32(4):458, April 1961.

[46] I. Utke, P. Hoffmann, R. Berger, and L. Scandella. High-resolution magnetic co supertips grown by a focused electron beam. *Appl. Phys. Lett.*, 80(25):4792 –4794, June 2002.

[47] Y. M. Lau, P. C. Chee, J. T. L. Thong, and V. Ng. Properties and applications of cobalt-based material produced by electron-beam-induced deposition. *J. Vac. Sci. Tech. A*, 20(4):1295 – 1302, July 2002.

[48] W. F. van Dorp and C. W. Hagen. A critical literature review of focused electron beam induced deposition. *J. Appl. Phys.*, 104(8):081301, October 2008.

[49] R. W. Christy. Formation of thin polymer films by electron bombardment. *J. Appl. Phys.*, 31(9):1680 –1683, September 1960.

[50] A. N. Broers, W. W. Molzen, J. J. Cuomo, and N. D. Wittels. Electron-beam fabrication of 80 metal structures. *Appl. Phys. Lett.*, 29(9):596 – 598, November 1976.

[51] P. B. Fischer, M. S. Wei, and S. Y. Chou. Ultrahigh resolution magnetic force microscope tip fabricated using electron beam lithography. *J. Vac. Sci. Tech. B*, 11(6):2570 – 2573, November 1993.

[52] M. Rührig, S. Porthun, and J. C. Lodder. Magnetic force microscopy using electron-beam fabricated tips. *Rev. Sci. Instrum.*, 65(10):3224–3228, October 1994.

[53] M. Rührig, S. Porthun, J. C. Lodder, S. McVitie, L. J. Heyderman, A. B. Johnston, and J. N. Chapman. Electron beam fabrication and characterization of high-resolution magnetic force microscopy tips. *J. Appl. Phys.*, 79(6):2913 – 2919, March 1996.

[54] G. D. Skidmore and E. DanDahlberg. Improved spatial resolution in magnetic force microscopy. *Appl. Phys. Lett.*, 71(22):3293 – 3295, December 1997.

[55] I. C. Chen, L. H. Chen, A. Gapin, S. Jin, L. Yuan, and S. H. Liou. Iron-platinum-coated carbon nanocone probes on tipless cantilevers for high resolution magnetic force imaging. *Nanotechnology*, 19(7):075501, February 2008.

[56] Z. F. Deng, E. Yenilmez, J. Leu, J. E. Hoffman, E. W. J. Straver, H. J. Dai, and K. A. Moler. Metal-coated carbon nanotube tips for magnetic force microscopy. *Appl. Phys. Lett.*, 85(25):6263 – 6265, December 2004.

[57] Z. F. Deng, E. Yenilmez, A. Reilein, J. Leu, H. J. Dai, and K. A. Moler. Nanotube manipulation with focused ion beam. *Appl. Phys. Lett.*, 88(2):023119, January 2006.

[58] T. Arie, H. Nishijima, S. Akita, and Y. Nakayama. Carbon-nanotube probe equipped magnetic force microscope. *J. Vac. Sci. Tech. B*, 18(1):104 – 106, January 2000.

[59] N. Yoshida, T. Arie, S. Akita, and Y. Nakayama. Improvement of MFM tips using Fe-alloy-capped carbon nanotubes. *Physica B*, 323(1 – 4):149 –150, October 2002.

[60] S. Ingole, P. Manandhar, J. A. Wright, E. Nazaretski, J. D. Thompson, and S. T. Picraux. Assembly and magnetic properties of nickel nanoparticles on silicon nanowires. *Appl. Phys. Lett.*, 94(22):223118–3, June 2009.

[61] G. Yang, J. Tang, S. Kato, Q. Zhang, L. C. Qin, M. Woodson, J. Liu, J. W. Kim, P. T. Littlehei, C. Park, and O. Zhou. Magnetic nanowire based high resolution magnetic force microscope probes. *Appl. Phys. Lett.*, 87(12):123507, September 2005.

[62] E. Nazaretski, E. A. Akhadov, I. Martin, D. V. Pelekhov, P. C. Hammel, and R. Movshovich. Spatial characterization of the magnetic field profile of a probe tip used in magnetic resonance force microscopy. *Appl. Phys. Lett.*, 92(21):214104–3, May 2008.

[63] O. Züger, S. T. Hoen, C. S. Yannoni, and D. Rugar. Three-dimensional imaging with a nuclear magnetic resonance force microscope. *J. Appl. Phys.*, 79(4):1881–1884, February 1996.

[64] S. Chao, W. M. Dougherty, J. L. Garbini, and J. A. Sidles. Nanometer-scale magnetic resonance imaging. *Rev. Sci. Instrum.*, 75(5):1175–1181, May 2004.

[65] M. Li, R. B. Bhiladvala, T. J. Morrow, J. A. Sioss, K. Lew, J. M. Redwing, C. D. Keating, and T. S. Mayer. Bottom-up assembly of large-area nanowire resonator arrays. *Nature Nanotech.*, 3(2):88 – 92, February 2008.

[66] T. J. Morrow, M. Li, J. Kim, T. S. Mayer, and C. D. Keating. Programmed assembly of DNA-coated nanowire devices. *Science*, 323(5912):352, January 2009.

[67] T. V. Roszhart. The effect of thermoelastic internal friction on the Q of micromachined silicon resonators. In *Solid-State Sensor and Actuator Workshop, 1990. 4th Technical Digest., IEEE*, pages 13–16, 1990.

[68] J. Yang, T. Ono, and M. Esashi. Energy dissipation in submicrometer thick single-crystal silicon cantilevers. *J. MEMS.*, 11(6):775–783, 2002.

[69] R. Lifshitz and M. L. Roukes. Thermoelastic damping in micro- and nanomechanical systems. *Phys. Rev. B*, 61(8):5600, February 2000.

[70] F. R. Blom, S. Bouwstra, M. Elwenspoek, and J. H. J. Fluitman. Dependence of the quality factor of micromachined silicon beam resonators on pressure and geometry. *J. Vac. Sci. Tech. B*, 10(1):19–26, 1992.

[71] P. Mohanty, D. A. Harrington, K. L. Ekinci, Y. T. Yang, M. J. Murphy, and M. L. Roukes. Intrinsic dissipation in high-frequency micromechanical resonators. *Phys. Rev. B*, 66(8):085416, 2002.

[72] G. Zolfagharkhani, A. Gaidarzhy, S. Shim, R. L. Badzey, and P. Mohanty. Quantum friction in nanomechanical oscillators at millikelvin temperatures. *Phys. Rev. B*, 72(22):224101, December 2005.

[73] D. F. Wang, T. Ono, and M. Esashi. Crystallographic influence on nanomechanics of ⟨100⟩-oriented silicon resonators. *Appl. Phys. Lett.*, 83(15):3189–3191, October 2003.

[74] D. W. Carr, S. Evoy, L. Sekaric, H. G. Craighead, and J. M. Parpia. Measurement of mechanical resonance and losses in nanometer scale silicon wires. *Appl. Phys. Lett.*, 75(7):920–922, 1999.

[75] A. Olkhovets, S. Evoy, D. W. Carr, J. M. Parpia, and H. G. Craighead. Actuation and internal friction of torsional nanomechanical silicon resonators. In *Papers from the 44th international conference on electron, ion, and photon*

beam technology and nanofabrication, volume 18, pages 3549–3551, Rancho Mirage, California, (USA), November 2000. AVS.

[76] R. E. Mihailovich and N. C. MacDonald. Dissipation measurements of vacuum-operated single-crystal silicon microresonators. *Sens. Act. A*, 50(3):199–207, September 1995.

[77] K. Y. Yasumura, T. D. Stowe, E. M. Chow, T. Pfafman, T. W. Kenny, B. C. Stipe, and D. Rugar. Quality factors in micron- and submicron-thick cantilevers. *J. MEMS.*, 9(1):117–125, 2000.

[78] Y. Wang, J. A. Henry, D. Sengupta, and M. A. Hines. Methyl monolayers suppress mechanical energy dissipation in micromechanical silicon resonators. *Appl. Phys. Lett.*, 85(23):5736–5738, December 2004.

[79] S. Rast, U. Gysin, P. Ruff, C. Gerber, E. Meyer, and D. W. Lee. Force microscopy experiments with ultrasensitive cantilevers. *Nanotechnology*, 17(7):S189–S194, 2006.

[80] B. E. White and R. O. Pohl. Internal friction of subnanometer a-SiO_2 films. *Phys. Rev. B*, 75(24):4437, December 1995.

[81] D. Lee, J. Kang, U. Gysin, S. Rast, E. Meyer, M. Despont, and C. Gerber. Fabrication and evaluation of single-crystal silicon cantilevers with ultra-low spring constants. *J. Micromech. Microeng.*, 15(11):2179–2183, 2005.

[82] J. Yang, T. Ono, and M. Esashi. Surface effects and high quality factors in ultrathin single-crystal silicon cantilevers. *Appl. Phys. Lett.*, 77(23):3860–3862, December 2000.

[83] T. Ono and M. Esashi. Effect of ion attachment on mechanical dissipation of a resonator. *Appl. Phys. Lett.*, 87(4):044105–3, July 2005.

[84] J. A. Henry, Y. Wang, D. Sengupta, and M. A. Hines. Understanding the effects of surface chemistry on Q: Mechanical energy dissipation in alkyl-terminated (C1–C18) micromechanical silicon resonators. *J. Phys. Chem. B*, 111(1):88–94, 2007.

[85] A. M. Richter, D. Sengupta, and M. A. Hines. Effect of surface chemistry on mechanical energy dissipation: Silicon oxidation does not inherently decrease the quality factor. *J. Phys. Chem. C*, 112(5):1473–1478, February 2008.

[86] S. S. Verbridge, H. G. Craighead, and J. M. Parpia. A megahertz nanomechanical resonator with room temperature quality factor over a million. *Appl. Phys. Lett.*, 92(1):013112–3, 2008.

[87] J. A. Marohn, R. Fainchtein, and D. D. Smith. An optimal magnetic tip configuration for magnetic-resonance force microscopy of microscale buried features. *Appl. Phys. Lett.*, 73(25):3778–3780, December 1998.

[88] F. E. Luborsky. Development of elongated particle magnets. *J. Appl. Phys.*, 32(3):S171–S183, March 1961.

[89] M. Giorgio, B. Meier, R. Magin, and E. Meyer. Magnetic damping losses of tipped cantilevers. *Nanotechnology*, 17(3):871–880, 2006.

[90] C. Chen. *Magnetism and metallurgy of soft magnetic materials*. North-Holland Pub. Co., New York, 1977.

[91] N. X. Sun and S. X. Wang. Soft high saturation magnetization Fe-Co-N thin films for inductive write heads. In *Magnetics Conference, 2000. INTERMAG 2000 Digest of Technical Papers. 2000 IEEE International*, page 191, 2000.

[92] *Standard Specifications for Permanent Magnetic Materials*, volume 0100-00. Magnetic Materials Producers Association.

[93] D. Jiles. *Introduction to magnetism and magnetic materials*. Chapman and Hall, London, 1st ed. edition, 1991.

[94] D. R. Lide. *CRC handbook of chemistry and physics*. CRC Press, Boca Raton, 2005.

[95] J. Du, W. H. Ko, and D. J. Young. Single crystal silicon MEMS fabrication based on smart-cut technique. *Sens. Act. A*, 112(1):116–121, April 2004.

[96] Z. Cui. *Micro-nanofabrication : technologies and applications*. Higher Education Press ;;Springer, Beijing ;Berlin, 2005.

[97] R. E. Oosterbroek, J. W. Berenschot, H. V. Jansen, A. J. Nijdam, G. Pandraud, A. van den Berg, and M. C. Elwenspoek. Etching methodologies in ⟨111⟩-oriented silicon wafers. *J. MEMS*, 9(3):390–398, 2000.

[98] H. Guckel. Surface micromachined pressure transducers. *Sens. Act. A*, 28(2):133–146, July 1991.

[99] B. Du Bois, G. Vereecke, P. Witvrouw, P. De Moor, A. Van Hoof, A. De Caussemaeker, and A. Verbist. HF etching of si-oxides and si-nitrides for surface micromachining. In *Sensor Technology 2001, Proceedings of the Sensor Technology Conference, Enschede, Netherlands, May 14-15, 2001*, pages 131–136. IMEC, 2001.

[100] H. von Kanel, K. A. Mader, E. Muller, N. Onda, and H. Sirringhaus. Structural and electronic properties of metastable epitaxial $FeSi_{1+x}$ films on Si$\langle 111 \rangle$. *Phys. Rev. B.*, 45(23):13807, June 1992.

[101] G. L. Molnar, G. Peta, E. Zsoldos, N. Q. Khanh, and Z. E. Horvath. Amorphous alloy formation and thickness dependent growth of gd-silicides in solid phase thin film reaction. *Thin Solid Films*, 317(1-2):417–420, April 1998.

[102] K. Hoummada, D. Mangelinck, E. Cadel, C. Perrin-Pellegrino, D. Blavette, and B. Deconihout. Formation of Ni silicide at room temperature studied by laser atom probe tomography: Nucleation and lateral growth. *Microelec. Eng.*, 84(11):2517–2522, November 2007.

[103] L. L. Luo, G. A. Smith, Shin Hashimoto, and W. M. Gibson. Room-temperature deposition and initial stages of cobalt silicide interface formation on a si $\langle 111 \rangle$ surface. *Nuclear Inst. Methods Phys. Res. B*, 45(1-4):488–491, 1990.

[104] F. M. D'Heurle and P. Gas. Kinetics of formation of silicides: a review. *J. Mater. Res.*, 1(1):205–221, 1986.

[105] L. A. Clevenger, C. V. Thompson, R. C. Cammarata, and K. N. Tu. Reaction kinetics of nickel/silicon multilayer films. *Appl. Phys. Lett.*, 52(10):795–797, March 1988.

[106] H. Miura, E. Ma, and C. V. Thompson. Initial sequence and kinetics of silicide formation in cobalt/amorphous-silicon multilayer thin films. *J. Appl. Phys.*, 70(8):4287–4294, October 1991.

[107] R. A. Donaton, K. Lokere, R. Verbeeck, and K. Maex. Etching of $CoSi_2$ in HF-based solutions. *Appl. Sur. Sci.*, 89(3):221–227, July 1995.

[108] M. D. Henry, S. Walavalkar, A. Homyk, and A. Scherer. Alumina etch masks for fabrication of high-aspect-ratio silicon micropillars and nanopillars. *Nanotechnology*, 20(25):255305, 2009.

[109] T. D. Stowe. *Extending the lower limits of force detection using micromachined silicon cantilevers*. PhD thesis, 2000.

[110] C. C. Welch, A. L. Goodyear, T. Wahlbrink, M. C. Lemme, and T. Mollenhauer. Silicon etch process options for micro- and nanotechnology using inductively coupled plasmas. *Microelec. Eng.*, 83(4-9):1170–1173, April 2005.

[111] S. Kuehn. *Force-gradient detected nuclear magnetic resonance and the origins of noncontact friction*. PhD thesis, 2007.

[112] S. A. Hickman, E. W. Moore, S. Lee, S. J. Wright, L. E. Harrell, and J. A. Marohn. Batch-fabrication of cantilevered magnets on attonewton-sensitivity mechanical oscillators for scanned-probe nanoscale magnetic resonance imaging. *In preparation*.

[113] D. Rugar, H. J. Mamin, and P. Guethner. Improved fiber-optic interferometer for atomic force microscopy. *Appl. Phys. Lett.*, 55(25):2588–2590, December 1989.

[114] K. J. Bruland, J. L. Garbini, W. M. Dougherty, S. H. Chao, S. E. Jensen, and J. A. Sidles. Thermal tuning of a fiber-optic interferometer for maximum sensitivity. *Rev. Sci. Inst.*, 70(9):3542–3544, 1999.

[115] T. R. Albrecht, P. Grutter, D. Horne, and D. Rugar. Frequency modulation detection using high-Q cantilevers for enhanced force microscope sensitivity. *J. Appl. Phys.*, 69(2):668–673, 1991.

[116] C. Rossel, P. Bauer, D. Zech, J. Hofer, M. Willemin, and H. Keller. Active microlevers as miniature torque magnetometers. *J. Appl. Phys.*, 79(11):8166–8173, June 1996.

[117] T. N. Ng, N. E. Jenkins, and J. A. Marohn. Thermomagnetic fluctuations and hysteresis loops of magnetic cantilevers for magnetic resonance force microscopy. *IEEE Trans. Mag.*, 42(3):378–381, 2006.

[118] E. W. Moore, S. Lee, S. A Hickman, S. J. Wright, L. E. Harrell, P. P. Borbat,

J. H. Freed, and J. A. Marohn. Scanned-probe detection of electron spin resonance from a nitroxide spin probe. *Proc. Natl. Acad. Sci.*, July In press.

[119] D. Shindo and Y. Murakami. Electron holography of magnetic materials. *J. Phys. D*, 41(18):183002, 2008.

[120] V. Bouchiat. Detection of magnetic moments using a nano-SQUID: limits of resolution and sensitivity in near-field SQUID magnetometry. *Supercond. Sci. Tech.*, 22(6):064002, 2009.

[121] G. Balasubramanian, I. Y. Chan, R. Kolesov, M. Al-Hmoud, J. Tisler, C. Shin, C. Kim, A. Wojcik, P. R. Hemmer, A. Krueger, T. Hanke, A. Leitenstorfer, R. Bratschitsch, F. Jelezko, and J. Wrachtrup. Nanoscale imaging magnetometry with diamond spins under ambient conditions. *Nature*, 455(7213):648–651, October 2008.

[122] N. C. Koshnick, M. E. Huber, J. A. Bert, C. W. Hicks, J. Large, H. Edwards, and K. A. Moler. A terraced scanning superconducting quantum interference device susceptometer with submicron pickup loops. *Appl. Phys. Lett.*, 93(24):243101–3, December 2008.

[123] T. Matsuda, A. Tonomura, R. Zuzuki, J. Endo, N. Osakabe, H. Umezaki, H. Tanabe, Y. Sugita, and H. Fujiwara. Observation of microscopic distribution of magnetic fields by electron holography. *J. Appl. Phys.*, 53(8):5444–5446, 1982.

[124] K. R. Williams, K. Gupta, and M. Wasilik. Etch rates for micromachining processing-part II. *J. MEMS*, 12(6):761–778, 2003.

[125] X. Zhang, J. Zhao, A. V. Whitney, J. W. Elam, and R. P. Van Duyne. Ultrastable substrates for surface-enhanced Raman spectroscopy: Al_2O_3 overlayers fabricated by atomic layer deposition yield improved anthrax biomarker detection. *J. Amer. Chem. Soc.*, 128(31):10304–10309, 2006.